Formation of low-mass helium white dwarfs orbiting binary millisecond pulsars

Dissertation
zur
Erlangung des Doktorgrades (Dr. rer. nat.)
der
Mathematisch-Naturwissenschaftlichen Fakultät
der
Rheinischen Friedrich-Wilhelms-Universität Bonn

vorgelegt von
Alina G. Istrate
aus
Tecuci (Rumänien)

Bonn 2016

Angefertigt mit Genehmigung der Mathematisch-Naturwissenschaftlichen Fakultät der Rheinischen Friedrich-Wilhelms-Universität Bonn

1. Gutachter: PD. Dr. Thomas Tauris
2. Gutachter: Prof. Dr. Norbert Langer

Tag der Promotion:
Erscheinungsjahr:

The beginning of knowledge is the discovery of something we do not understand

---

Frank Herbert

Abstract

Millisecond pulsars (MSPs) belong to a class of radio pulsars characterized by high rotational spin rates and low magnetic fields. These neutron stars are believed to be the end-product of binary evolution, in which an old neutron star accretes matter and angular momentum from a close stellar companion for an extended period of time, while being observable as an X-ray binary. During this evolutionary phase, they acquire millisecond spin periods and, after the accretion episode ceases, they are reactivated as radio emitting pulsars. The majority of MSP companions are low-mass helium-core white dwarfs (He WDs). However, MSP systems harbouring carbon-oxygen white dwarfs (CO WD), neutron stars, or ultra light companions have also been found, suggesting a diversity in the nature of their progenitors. A handful of MSPs are observed in very compact orbits, $P_{\rm orb} \simeq 2 - 9$ hr, orbiting around low-mass He WDs with masses below 0.25 $M_\odot$ and surface gravities $5 < \log g < 7$, the so-called extremely low-mass helium white dwarfs (ELM WDs).

Today we know of the existence of more than 80 ELM WDs. The increasing number of discovered ELM WDs reveals that they are formed in different environments, from the Galactic disk to open and globular clusters. ELM WDs are most likely the result of binary evolution as they cannot be formed from single stars within a Hubble time. Indeed, over 80% of the observed ELM WDs are found in binary systems, most commonly around a more massive CO WD. The new wealth of data raises questions regarding the puzzling presence of metals in the atmospheres of young bloated ELM proto-WDs and the newly discovered pulsations in three ELM proto-WDs. In this context, improved stellar evolutionary models in which binary evolution is fully accounted for are needed in order to explain the formation and the observed properties of these objects.

In this thesis, we investigate the formation of MSPs found in compact orbits with ELM WD companions through numerical calculations using state-of-the-art stellar evolutionary codes. In particular, we examine if the observed systems can be reproduced by theoretical modelling using standard prescriptions of angular momentum loss with contributions from gravitational wave radiation, magnetic braking and mass loss. We find that a severe fine-tuning in the initial orbital period is necessary to reproduce the observed number of MSPs with ELM WD companions suggesting that something needs to be modified or is missing in the standard input physics of their modelling.

Moreover, we explore the formation and cooling of ELM WDs through a large grid of computed models suited for environments with different metallicities, with emphasis on the proto-WD phase. Specifically, we analyse in detail the evolutionary times of these objects which are of great importance in providing an accurate independent age estimate for MSP systems. For the first time, we study the combined effects of element diffusion, i.e. gravitational settling, thermal and chemical diffusion, and rotational mixing on the evolution of these WDs. Our results show that rotational mixing plays a key role in determining the chemical composition of the surface layers of ELM proto-WDs, but it does not affect their internal structure. This finding has important implications for the asteroseismology studies of ELM proto-WDs which are currently pursued. Furthermore, we suggest that the spin frequencies of the resulting WDs are well above the orbital frequencies, a result which needs to be confirmed by further dedicated observations.

Contents

CHAPTER 1

Introduction

> Astronomy, as nothing else can do, teaches men humility.
>
> Arthur C. Clarke, The Challenge of the Spaceship, 1959

Astronomy is as old as mankind although the concepts tremendously evolved and changed with time. The last 100 years represents a huge step forward in scientific and technological development. For astronomy, the availability of more telescopes, bigger telescopes, space missions and ever increasing computing power provides new windows and methods to study the surrounding Universe.

Stars are fundamental objects in the Universe as they are the building blocks of larger structures such as clusters and galaxies. As an example, our own galaxy, the Milky Way, a typical spiral galaxy, contains between 10^{11} to 10^{12} stars. In the early Universe, the first generation of stars formed exclusively from the primordial gas which contained hydrogen, helium, and very small amounts of lithium and beryllium. It is the first stars that produced heavier elements which changed the dynamics and evolution of the Universe as we know it today. The history of a galaxy can be traced by statistically studying the properties of its stars. Thereby, stellar astrophysics, which studies the birth, the evolution and the death of the stars plays a central role in modern astrophysics.

Stars form inside very cold (~10–20 K) clouds of gas which are composed mostly of molecular hydrogen and helium. In addition, they are seeded with heavier elements from stars that lived and died before them. These clouds extend across hundreds of light years and contain the raw material for thousands or even more stars. A nearby supernova, collisions with another gas cloud, or the pressure wave of a galaxy's spiral arms passing through the region can disrupt the balance between the cloud's gravity and the outward gas pressure of the molecules, causing the cloud to collapse. As the cloud collapses, it breaks into smaller and smaller increasingly compact clumps, until there are knots with roughly the mass of a star. These newly formed objects are the so-called *protostars*. The protostar is surrounded by a circumstellar disk from which it may still accrete material while the remaining matter eventually will form a planetary system. When the central temperature of the protostar reaches roughly 10^7 K, hydrogen can fuse into helium. Once the nuclear fusion starts, a new star is born! Some objects don't accumulate enough mass to be able to start nuclear fusion and become brown dwarfs, substellar objects, which slowly cool down over billions of years. A qualitative picture showing the formation process, the evolution and the type of remnant for different stellar masses is shown in Fig. 1.1.

According to their observational properties, stars can be classified in various ways creating a true stellar zoo. However, the most important factor in determining the evolution of a star is its initial mass. From a theoretical point of view, stars can simply be classified according to their initial mass as *low-mass stars*, with $0.08 \lesssim M/M_{\odot} \lesssim 2.0$, *intermediate-mass stars*, with $2.0 \lesssim M/M_{\odot} \lesssim 8.0$ and *high-mass stars* or *massive stars* with $M \gtrsim 8.0\ M_{\odot}$.

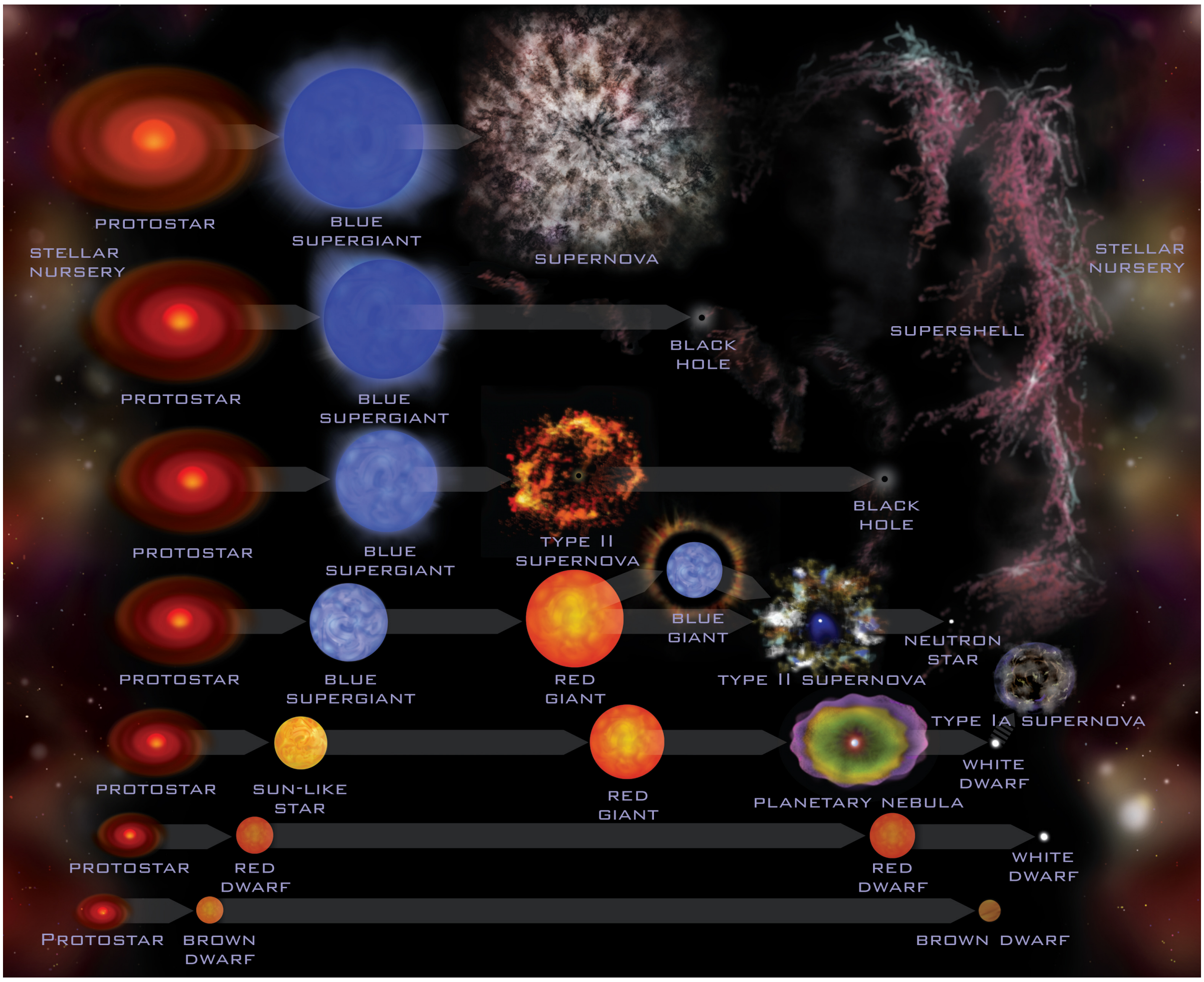

Figure 1.1: Image depicting birth, evolution and death of stars. The mass of the star increases on the y-axis and the time evolution is represented on the x-axis, from left to right. Credit: Jet Propulsion Laboratory.

The distribution of the initial masses in a population of stars is described by an empirical function, called the *initial mass function*. The initial mass function of the local solar neighbourhood (Salpeter 1955; Kroupa 2002) indicates that the vast majority of stars ($\sim 90\%$) are born with masses less than 0.8 $M_\odot$, while massive stars are very rare, less than 1% of all stars.
Stellar evolution can not be studied by continuously observing an individual star as most changes occur over millions or billions of years, but by observing numerous stars which are in various stages of their evolutionary history. Astronomers visualize the evolution of a star in a so-called *Hertzsprung-Russell diagram* (HRD). The most common used quantities plotted in this diagram are luminosity[1] and surface (effective) temperature.

1.1 Stellar evolution in a nutshell

Stars, much like humans, are born, evolve and eventually die. The evolution of a single star, its lifetime and the nature of its compact remnant are primarily determined by its initial mass. However, other

---

[1] total energy emitted by a star per unit time.

parameters, such as chemical composition, rotation and mass-loss by a stellar wind also play a crucial role. Things get much more complicated if the star, at some point in its life, interacts gravitationally with another star and experiences mass transfer from one to another. A complete introduction on stellar astrophysics is beyond the scope of this thesis, but the interested reader is referred to, for example, the textbook by Kippenhahn et al. (2012).

A star can be approximated by a self-gravitating gas (plasma) in hydrostatic equilibrium that radiates energy into its surrounding space. The *virial theorem* states that the radiative loss of energy for such a gas causes it to contract. During the contraction phase, the gas releases gravitational energy which translates into an increase in its temperature. Thus, while the star tries to cool itself by radiating away energy through the surface, instead gets hotter. The more it radiates, the hotter it gets and the more it has to radiate away. This is an unstable situation in the long run and explains why the star ends its life as a compact object. However, nuclear fusion provides the energy that is lost at the surface for most of the lifetime of a star leading to the stability we observe, for example, in our own Sun. The energy produced in the center of the star needs to be transported to the surface[2], thus a temperature gradient is established which is coupled to the pressure gradient that provides the hydrostatic equilibrium.

Nuclear fusion occurs in regions of the star where the temperature is high enough that quantum mechanical effects lead to the fusion of some nuclei into heavier ones, with the release of their binding energy (the difference in the rest mass). Depending on the initial mass[3], there are different nuclear fusion cycles that can occur in the core of a star through which the initial hydrogen is gradually converted to helium, helium to carbon and then further to heavier elements such as neon, oxygen and silicon in the case of the more massive stars. As the energy source changes, the star goes through different evolutionary stages characterized by changes in its observable properties such as surface temperature, luminosity, and radius.

In general, massive stars produce metals[4] up to iron during the core nuclear burning phases. However, through processes such as the *s-process*[5], heavier elements than iron can be produced. During the final stages of their evolution, stars shed a fraction of their material into space through a stellar wind[6], thus recycling interstellar material. The remnants of stellar evolution are white dwarfs for low- and intermediate-mass stars, and neutron stars and black holes for massive stars.

Low- and intermediate-mass stars

All stars initially convert hydrogen into helium. During this evolutionary phase, stars are found on the *main sequence* which is the region in the HRD where stars spend most of their lives and, therefore, is also the most populated region of the diagram. At the end of this phase[7], the star will have an inert helium core surrounded by a hydrogen envelope.

A *low-mass star*, such as our own Sun, will spend about 10^{10} years on the main sequence. Once the helium core is formed, the central temperature is not high enough for helium fusion to occur. As no nuclear energy source is available to balance the energy loss from the surface, the core slowly starts to contract. As the contracting core heats up, hydrogen will start burning in a shell surrounding the core, releasing more energy per unit time (i.e luminosity) than during the main sequence phase due to a higher core temperature.

---

[2] either through convection or radiative transport.

[3] The crucial difference between low, intermediate and high-mass stars stars is the core temperature.

[4] In astrophysics, metals denote all the chemical elements heavier than hydrogen and helium.

[5] The s-process is a nucleosynthesis process that occurs at relatively low neutron density such that any unstable products have time to decay before another neutron is captured.

[6] In general, the more massive the star, the stronger the wind-mass loss.

[7] The main sequence ends when the supply of hydrogen runs out in the inner $\sim 10\%$ of the mass the star.

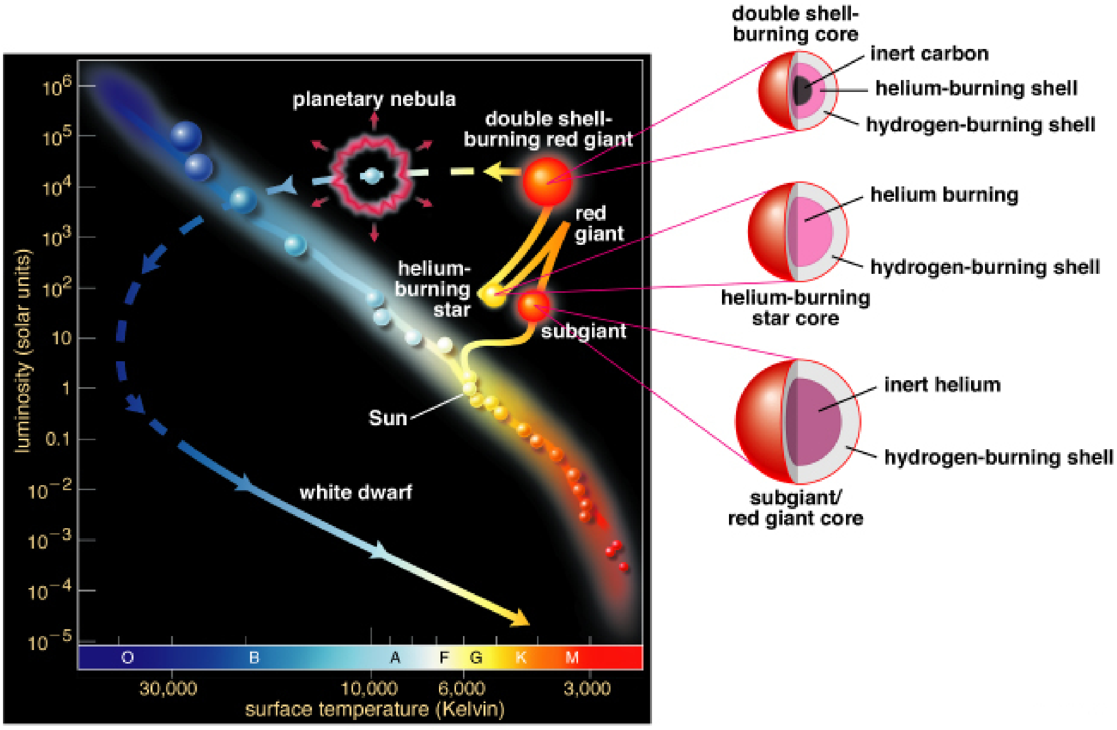

Figure 1.2: The evolution of a low-mass star in the Hertzsprung-Russell diagram (HR). Credit: Addison Wesley.

The pressure produced by the burning shell is transferred to the envelope causing it to expand and cool down. During this phase, the radius of the star expands 10 to 100 times its original size, while the surface temperature decreases – characteristics that give rise to the name *red-giant* phase. The evolution of a low-mass star in the HRD, as well as its internal structure, is schematically shown in Fig. 1.2. The helium core contains a mixture of helium nuclei and electrons. According to the Pauli exclusion principle, two electrons cannot occupy the same energy level with identical quantum numbers simultaneously. As the core of the star contracts, it becomes denser and denser and therefore the lowest electron energy levels are filled and the electrons are forced into higher and higher energy levels. This gives rise to a pressure called the *electron degeneracy pressure* which prevents further gravitational collapse. When degeneracy pressure is stronger than thermal pressure, the gas is said to be *degenerate*. A degenerate gas behaves quite differently than an ideal gas. While for an ideal gas, the pressure depends on the density and the temperature, for the degenerate gas the pressure depends only on the density. In all low-mass stars, the helium core becomes degenerate during the red-giant phase.

Nuclear reactions that occur in a degenerate core tend to be explosive, generating a type of runaway process. An increase in the temperature in the degenerate gas does not increase the pressure, so the gas cannot expand and cool down. The temperature increase makes it easier for the nuclear reactions to occur, as they are very temperature dependent. The nuclear reactions occur more and more rapidly until the temperature of the core becomes so high that the degeneracy is lifted. The ignition of helium in low-mass stars is thus an explosive phenomenon called *helium core flash* in which a large amount of helium fuses to carbon in a matter of seconds. After the flash, the luminosity decreases and the outer layers of the star shrink. Low-mass stars ignite helium in their cores essentially at the same core mass of 0.45 $M_\odot$. As the core structure of all such stars is similar, during helium burning they are found on the *horizontal branch*, characterized by near constant luminosity. One of the main difference between low-and intermediate-mass stars ($2.0 \lesssim M/M_\odot \lesssim 8.0$) is that the latter, due to higher central temperatures, have non-degenerate cores when helium burning starts, and the core helium burning proceeds steadily.

After helium core burning, the evolution of low- and intermediate-mass stars is qualitatively alike. Over time, the core is depleted of helium leaving behind the ashes from the nuclear burning (carbon and oxygen). At this point, the star is made of a carbon-oxygen core, a helium shell surrounding the core and the outer part of the star forms a hydrogen shell. Following helium depletion, the star begins to contract and heat up. The nuclear burning proceeds into a helium shell surrounding the core, causing the star to expand again and go through a second red giant-like stage on the *the asymptotic giant branch*. This phase is relatively short compared to the previous ones, lasting about only one million years for a Solar-type star. During the red-giant and the asymptotic-giant phase, stars lose significant part of their envelopes due to a strong stellar wind. During this last phase, the core does not reach the temperature necessary for carbon burning to ignite. However, the helium shell burns in a series of helium shell flashes which causes the ejection of the outer helium and hydrogen layers. This outer hot ejected gas forms a so-called *planetary nebula*. The carbon-oxygen core left behind is supported by electron degeneracy pressure and this new object is called a *white dwarf*, because it is hot and small in size.

Massive stars

A massive star continues nuclear burning beyond helium burning, such that, after several stages of nuclear fusion, the inner core will be made out of iron. The core nuclear burning cycle ends once the iron core is formed, as further fusion requires energy rather than releasing it.

Over time, the internal structure of a high-mass star resembles the structure of an onion, with concentric layers of different elements layered over each other, with highest mass element (iron) at the center.

If the mass of the iron core exceeds the Chandrasekhar limit of $\sim 1.4\ M_\odot$, which is the maximum mass for an electron-degenerate configuration, the star will collapse to form either a neutron star or a stellar-mass black hole, depending on the mass of the remaining core. The gravitational energy released during the implosion is way larger than the binding energy of the envelope of the star. This will result in a supernova explosion in which the collapsing star ejects its envelope with a typical speed of about 10^4 km s^{-1}. These type of supernovae, called *core-collapse supernovae* are some of the most energetic events in the Universe. For the few weeks that they are at peak brightness, their luminosities can compete with the luminosity of the entire galaxy in which they are born.

The last stages of a massive star, during and beyond carbon burning, are very short lasting compared to the lifetime of the star as the burning process becomes less and less efficient, i.e. progressively less energy is released. The evolution of the core is accelerated as the energy during these burning stages is mostly released as neutrinos, which can escape the star without interaction with the stellar matter. Massive stars are considered cosmic engines because they are responsible for a large fraction of the ionized gas and metals found in normal galaxies.

Table 1.1 lists the possible end-products as a function of the initial mass for single stars. These values and outcomes (e.g. the possibility of forming helium white dwarfs) will change if binary interactions are at work. The mass values are only indicative and depend on the metallicity and uncertainties in mass loss rates and assumed physics. Moreover, for binaries, the values depend on the initial orbital period and mass ratio.

1.2 Binary evolution

Stars, much like every living organisms, do not prefer life in isolation. Roughly two thirds of all stars are members of a binary or multiple systems with orbital periods ranging from ~ 10 min to $\sim 10^6$ years.

Table 1.1: End products of single stellar evolution as function of initial mass (Tauris & van den Heuvel (2006)).

Initial mass	He-core mass	Stellar remnant
< 2.3 $M_\odot$	< 0.45 $M_\odot$	CO white dwarf
2.3-6 $M_\odot$	0.5-1.9 $M_\odot$	CO white dwarf
6-8 $M_\odot$	1.9- 2.1 $M_\odot$	ONeMg white dwarf
8-12 $M_\odot$	2.1-2.8 $M_\odot$	neutron star
12-25 $M_\odot$	2.8-8 $M_\odot$	neutron star
> 25 $M_\odot$	> 8 $M_\odot$	black hole

The majority of them are in wide systems in which both of the components are basically evolving as single stars. However, there is a fraction of binary systems close enough that the stellar companions will interact at some point in their lifetime. During this interaction, mass and angular momentum are transferred from the donor star to the accreting star which changes the structure of both stars and subsequently their evolution. Binary interactions give rise to numerous spectacular phenomena which are absent in single star evolution. Compact binaries, in which at least one of the components is a compact remnant of a star, host most of the observed high-energy phenomena: X-ray bursts, X-ray pulsars, novae, supernovae Type Ia, radio and X-ray jets, accretion disks and even gamma-ray bursts.

If two stars orbit each other, we define the *Roche potential* as the effective potential describing their mutual attraction. It includes the gravitational potential of each individual star and the contribution from the centrifugal force. In a binary system[8] one can define fixed equipotential surfaces, of particular importance being the equipotential surface (pear-like shape) passing through the first Lagrangian point, known as the Roche-lobe (see Fig. 1.3). The Roche potential limits the expansion of a star in a binary to a maximum radius, the *Roche-lobe radius*. If a star expands to fill its Roche lobe, i.e. its radius is close to the Roche-lobe radius, material will be transferred to its companion star.
The Roche-lobe radius is approximated by the following expression (Eggleton 1983):

$$R_L = \frac{0.49q^{2/3}}{0.6q^{2/3} + ln(1 + q^{1/3})}a, \tag{1.1}$$

where a is the orbital separation and q=$M_{\rm donor}/M_{accretor}$ is the mass ratio between the two stars.
According to the Roche-lobe geometry, binary stars can be found in three states:

- *detached binaries*: both stars are confined within their Roche lobes. The only influence they have on each other is through gravitation, tidal interactions and stellar winds.
- *semi-detached binaries*: one of the stars fills its Roche lobe (the donor). Mass is being transferred from the envelope of the donor towards the accretor.
- *contact binaries*: both stars fill or overfill their Roche lobe. Both stars are gravitationally distorted and surrounded by a common photosphere through which the stars are in physical contact.

Once a star fills its Roche lobe, i.e. the stellar radius is slightly larger than the Roche-lobe radius, $R \gtrsim R_L$, matter starts being transferred towards the companion in a phase called *Roche-lobe overflow* (RLO). A star can fill its Roche lobe due to either radial expansion as a result of nuclear evolution, or orbital shrinkage due to orbital angular momentum losses. When RLO is initiated, the stability of the mass transfer process depends on several factors.

---

[8] in which the tidal forces have circularized the orbit and the stellar rotation is synchronized with the orbit.

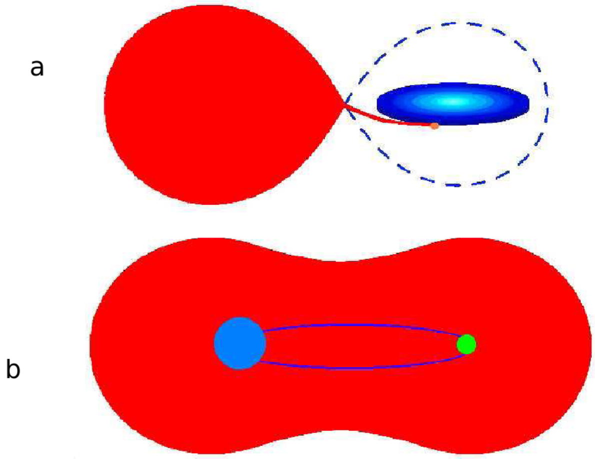

Figure 1.3: Simple representation of stable mass transfer (a) and unstable mass transfer through common envelope evolution (b). Credit: Philipp Podsiadlowski.

These factors include how the radius of the donor responds to the mass loss and how the orbit itself, and therefore also R_L, responds to mass transfer. In addition, the dynamical stability also depends on the response of the companion star to the mass being transferred to it. Depending on the evolutionary state of the donor, RLO mass transfer can be classified into three cases:

- *Case A* mass transfer is initiated while the donor is still on the main sequence, i.e. undergoing core-hydrogen burning.
- *Case B* mass transfer occurs when the donor left the main sequence but did not start yet helium core burning.
- *Case C* mass transfer occurs when the donor overflows its Roche lobe during helium shell burning or beyond.

When considering binary evolution, three timescales associated with single stars evolution become important:

- *the dynamical timescale* is the timescale in which a star reacts to a perturbation on its hydrostatic equilibrium. It is given by the ratio of the stellar radius to the sound speed of the stellar matter:

$$\tau_{dyn} = \frac{R}{c_s} \approx 0.04\left(\frac{M_\odot}{M}\right)^{1/2}\left(\frac{R}{R_\odot}\right)^{3/2} \text{ day} \tag{1.2}$$

- *the thermal timescale* is the timescale in which a star reacts when energy loss and energy production are no longer in equilibrium. It can be expressed by the ratio of the thermal energy reservoir of the star, $E_{\rm th}$ and its luminosity L :

$$\tau_{KH} = \frac{E_{th}}{L} \approx \frac{GM^2}{2RL} \approx 1.5\times 10^7\left(\frac{M}{M_\odot}\right)^2 \frac{R}{R_\odot}\frac{L_\odot}{L} \text{ yr} \tag{1.3}$$

- *the nuclear timescale* is the timescale in which a star uses its nuclear fuel reservoir:

$$\tau_{nuc} = 0.007 \frac{M_{core} c^2}{L} \approx 10^{10} \frac{M}{M_\odot} \frac{L_\odot}{L} \text{ yr} \tag{1.4}$$

  where c is the speed of light and $M_{\rm core}$ is the mass of the stellar core.

The response of the stellar radius to mass loss depends critically on the structure of the envelope of the star and, in particular, whether the envelope is convective or radiative. Stars with radiative envelopes shrink in response to mass loss, while stars with convective envelopes tend to expand rapidly.

Depending on the reaction of the stellar radius to mass loss, RLO mass transfer can be classified as *stable mass transfer*, *thermal time-scale mass transfer* and *dynamically unstable mass transfer*. The later often leads to a *common envelope* (CE). Figure 1.3 shows the geometry for stable mass transfer as well as for a common envelope.

Dynamically unstable mass transfer occurs when the donor is a giant or supergiant with a convective envelope, because a star with a convective envelope tends to expand rather than shrink when it losses mass very rapidly (adiabatically). In this case, the radius of the star expands faster than its Roche-lobe radius causing a runaway mass transfer on a dynamical timescale. In the same time, the Roche-lobe radius shrinks when mass is transferred from a more massive to a less massive star, making the donor overfill its Roche lobe by an ever larger amount. Once a common envelope system is formed, friction between the immersed binary will make the two components spiral towards each other until enough orbital energy has been released to eject the envelope (Paczynski 1976), in a poorly understood process. This ends the spiral-in phase and leaves a much closer binary with an orbital period typically between $\sim$ 0.1 and $\sim$ 10 d, consisting of the core of the giant and a normal secondary star. In contrast to the RLO channel, CE evolution tends to produce very short period systems. Since the spiral-in phase is very short lived, the companion star will not be able to accrete much matter and it will be mostly unchanged at the end of this phase. The conditions for the occurrence of dynamical mass transfer are not well determined. It is usually assumed that the mass transfer from a star with a convective envelope is dynamically unstable if the mass ratio of the donor to the mass accretor is larger than a critical value of $\sim$ 1.3. The formation and evolution of compact binary stars is reviewed in Tauris & van den Heuvel (2006) and Postnov & Yungelson (2014) and a complete review of the common envelope formalism can be found in Ivanova et al. (2013).

1.3 White dwarfs

A white dwarf (WD) is the stellar remnant of low- and intermediate-mass stars, i.e. stars with mass smaller than 10±2 $M_\odot$. More than about 97% of all stars, including our own Sun, will end their life as a WD. Because many WDs are among the oldest objects in the Galaxy, they can be used to determine the age of the stellar population where they reside, such as the Galactic disk (e.g. Oswalt et al. 1996), individual open clusters (e.g. García-Berro et al. 2010), and the Galactic halo (e.g. Kalirai 2012). Moreover, studying the population of WDs in a given environment, reveals important information about the star formation process (Tremblay et al. 2014).

Because of their small radii, WDs are intrinsically faint, and therefore, from an observation point of view, they are hard to detect requiring moderately large telescope apertures. The *Sloan Digital Sky Survey* (SDSS) played a major role in the last decade by spectroscopically identifying roughly 30 000 WDs (Kepler et al. 2016) and this number will only increase to reach $\sim 10^5$ with the new Gaia mission (Gaensicke et al. 2015).

White dwarfs are supported against gravitational collapse by the electron degeneracy pressure. This provides a maximum limit for the mass of a WD, known as the Chandrasekhar mass limit that is roughly about 1.4 $M_\odot$. Any isolated WD with a mass below this critical mass will stay a WD forever, while a WD that exceeds this mass, for example, by accretion in a binary system, will collapse and possibly explode in a thermonuclear supernova.

White dwarfs have a relatively simple structure of an isothermal core surrounded by a non-degenerate envelope. The chemical composition of both the core and the envelope depends on the WD mass and are basically determined by the evolution of the WD progenitor. Most of them have a core composed of a mixture of carbon and oxygen with a thin helium mantle (containing $\sim 1\%$ of their mass) surrounded by a thinner hydrogen envelope (most 0.01% of the WD mass). The WDs with a mass smaller than about 0.4 $M_\odot$ have helium cores and are produced in close binary systems, while those more massive than about 1.05 $M_\odot$ are probably made of oxygen, neon and magnesium.

Spectral types

White dwarfs can be classified according to their optical spectra, i.e the dominant spectral lines in their atmospheres as (i) DA: strong hydrogen lines, (ii) DB: strong He I lines, (iii) DO: strong He II lines, (iv) DC: no strong lines (continuous) spectrum, (v) DZ: strong metal lines (excluding carbon), (vi) DQ: strong carbon lines.

About 80% of the WDs enter the WD cooling domain with hydrogen-rich atmospheres. Gravitational settling (element sedimentation) is very efficient in the regime of high surface gravities exhibited by WDs ($\log g \sim 8$) leading to the formation of almost pure hydrogen atmospheres, the DA WDs. The mass distribution of DA WDs peaks at 0.59 $M_\odot$ and also exhibits high- and low-mass components (Kepler et al. 2007; Kleinman et al. 2013; Kepler et al. 2015).

Some of the newly formed WDs may experience a very late helium flash, during which the WD undergoes violent mixing episodes. As a result, the atmospheres of these WDs contain a mixture of helium, carbon and oxygen. These are very hot objects, called the PG1159 stars, showing a very characteristic spectral signature. The interplay between stellar winds, gravitational settling, cooling evolution and possible pollution from an accretion disk leaves behind DO, DB, DQ, DZ, and DC stars.

Cooling evolution

The evolution of a WD can be treated as a simple cooling process in which the internal energy of the ions in the degenerate core act as a reservoir of energy and the outer non-degenerate layers control the energy outflow. Energy transport in the interior of the WD is dominated first by neutrinos and then by electron conduction. In the outer non-degenerate layers, radiation transports the energy to the surface but, at lower temperatures, convection associated with the partial ionization of the most abundant element at the surface becomes important.

The basic theory of WD cooling was developed more than 60 years ago by Mestel (1952), who found a power-law relation between age and WD luminosity:

$$t_{\mathrm{cool}} \propto L^{-5/7}. \tag{1.5}$$

The Mestel age-luminosity relation is in good agreement with detailed numerical evolutionary models, in particular in the regime $-1 \geq \log(L/L_\odot) \geq -3$. However, important physical processes such as for example neutrino cooling, crystallization and surface convection can change the cooling time compared to the simple relationship above.

An example of the formation and evolution of a WD in the HR diagram is shown in figure 1.4.

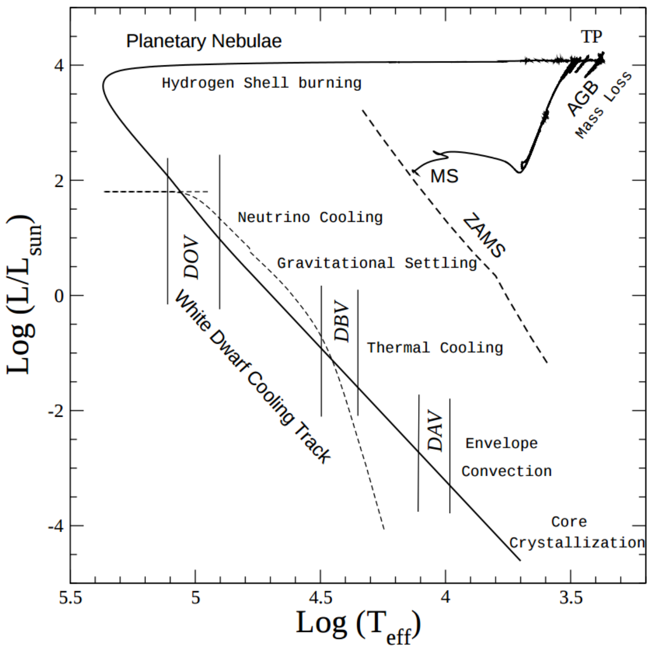

Figure 1.4: HR-diagram for the full evolution of a 3.5 $M_{\odot}$ star from the zero-age main sequence to the white dwarf domain. Mass-loss episodes at the thermally pulsing AGB reduce the stellar mass to 0.66 $M_{\odot}$. The various physical processes which occur as the WD cools, as well as the domain of the pulsating instability strips for the DOV, DBV and DAV, are indicated. The thin dashed line displays the neutrino luminosity. Figure from Althaus et al. (2010).

In the earliest stage, the cooling is a very complicated function of the initial status of the pre-white dwarf, such as the pulse-interpulse phase at which the WD is formed. The cooling also depends on the number of thermal pulses the star suffered before planetary nebula ejection, and the chemical stratification. The thermal evolution is affected by processes such as mass loss, radiative levitation of elements, gravitational settling and diffusion.

The ions inside the WD core behave initially as a gas, and, as the cooling evolution proceeds, as a fluid, and ultimately undergoes a first-order phase transition to the solid phase. A significant amount of energy is lost in the early phases of the WD cooling through neutrino processes. Consequently, the cooling process of a WD can be roughly divided in four stages (Isern & García–Berro 2004; Kawaler et al. 1996):

- *Neutrino cooling* occurs when log $(L/L_{\odot}) > -1.5$. Shortly after the planetary nebula phase, the core of the WD is still hot enough such that a large number of neutrinos are formed through processes involving the electroweak interaction. The vast majority of the neutrinos escape without interaction to outer space, thus contributing to an important stellar energy sink. The evolution of a very hot, young WD is thus dominated by neutrino cooling.

- *Fluid cooling* occurs at $-1.5 \geq \log(L/L_{\odot}) \geq -3$. This is the best understood phase in the WD cooling evolution. At this point, the ratio of Coulomb energy to thermal ion energy exceeds one and the WD core becomes a Coulomb liquid. At this stage, the fluid is only loosely coupled and the transfer of energy through the envelope is controlled by a large buffer of non-degenerate matter.

- *Crystallization* settles in when log $(L/L_{\odot}) < -3$ and leads to one of the largest sources of uncertainty in determining the ages of cool WDs (Segretain et al. 1994). When a typical WD with a mass of 0.6 $M_{\odot}$ cools down to $T_{\rm eff} \simeq 6000-8000$ K, the core will undergo a phase transition from liquid to solid, when the Coulomb energy exceeds the thermal energy of the ions by a factor of about 171. The phase transition releases latent heat which contributes as a new source of thermal energy that introduces a delay in the cooling of the WD. Its contribution to the total luminosity is between ~5 and 10%. Sedimentation of heavy ions upon crystallization, with subsequent release of gravitational binding energy, represents another major source of energy for cool WDs. Minor species are the main source of uncertainty since, for example, neon can introduce a delay in the range of 0.5 – 9 Gyr (Isern et al. 1991), while iron can introduce an additional delay of 1 Gyr.

- *Debye cooling* takes over as quantum effects become important after crystallization. During this stage, the thermal content of the WD is progressively depleted as central temperature drops. After most of the star solidifies, the cooling curve begins to decline again, more steeply than before. The crystal lattice causes coherent vibrations and this actually promotes further energy loss. This is known as Debye cooling. The internal thermal content has been depleted and subsequent contraction of the outer envelope contributes up to 30 percent of the luminosity output.

In the case of low-mass helium-core WDs, the mass of the hydrogen envelope plays an extremely important role in their cooling evolution, such that, the WDs that enter on the cooling track with a thick hydrogen envelope will cool much slower than those with a thin hydrogen envelope due to the residual burning of hydrogen. Therefore, the determination of the hydrogen envelope mass at the beginning of the cooling track for such objects is very important for an accurate determination of their age.

Detailed reviews of recent developments in the WD field can be found in Koester (2002); Hansen & Liebert (2003); Fontaine et al. (2001); Althaus et al. (2010); Kilic (2011), while an introduction to the basic theory of WD cooling can be found in D'Antona & Mazzitelli (1990).

1.4 Neutron stars

Unlike WDs, neutron stars (NSs) are born in a more violent fashion, as a result of a supernova explosion that occurs in the last few moments in the evolution of massive stars (M$\gtrsim$ 8.0 $M_{\odot}$). When all the nuclear fuel in the core of the massive star has been exhausted, the remaining iron core must be supported by degeneracy pressure alone. If the core mass exceeds the Chandrasekhar limit of about 1.4 M$_{\odot}$, the electron degenerate pressure cannot counteract the gravity anymore. The core thus becomes unstable and collapses.

Because of the extreme conditions available now in the core, i.e T ~ $10^9 - 10^{10}$ K, a process of photo-disintegration starts, in which the energetic photons destroy the iron nuclei into helium nuclei. The helium nuclei will further disintegrate into single protons and neutrons, thus reversing the result of the nuclear burning which have been taking place in the core of the star during its lifetime. The photo-disintegration is an endothermic process, which contributes to a faster contraction of the core. The newly formed protons mutate into neutrons by an inverse β-decay process $e^- + p \rightarrow n + \nu_e$, which is also an endothermic process. This phase is called *neutronization*, because its effect is to destroy protons and electrons and create neutrons. The core collapses until the neutron degeneracy pressure is high enough to stop the collapse. During this quick implosion of the star, the core converts into a hot neutron sphere. The envelope of the massive star moves in free fall to the center and is reflected there because of the repulsive strong interaction force of supra-nuclear dense matter. As a result, an outward shock is launched from the surface region of the proto-neutron star. A stream of neutrinos helps to boost the unbound matter off in a powerful explosion. Immediately after the supernova event, the temperature of the newborn neutron star is about 10^{12} K.

Neutron stars are some of the most extreme objects in the Universe. They are about 20 km in diameter and have a mass of about 1-2 times that of the Sun. Moreover, they posses magnetic fields millions of times stronger than the strongest magnetic field produced on Earth.

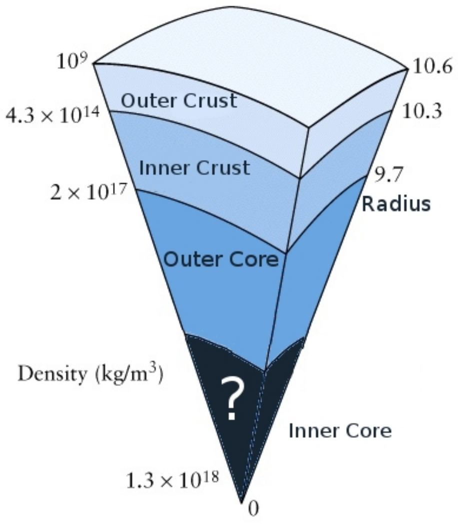

Figure 1.5: The internal structure of a neutron star. Credit: Alessandro Patruno.

Because NSs retain the angular momentum of the original larger core of their progenitor star, they usually rotate very fast – up to several hundred times per second for a newly born NS.
The structure of a NS is not yet fully understood. A simplified picture is shown in figure 1.5 where one can distinguish several regions:

- the atmosphere is thin (~ a few cm thick) and consists of very hot plasma, on top of an iron envelope. The density here is $\rho \lesssim 10^6$ g cm^{-3}.
- the outer crust in only about 200 m thick and consists of a solid lattice (or a dense liquid at early stages) of heavy nuclei. The dominant pressure in this region is from electron degeneracy. The density is not high enough here to favor neutronization.
- the inner crust is from 0.5 to 1 km thick. The pressure is higher and the lattice of heavy nuclei is now permeated by free neutrons that begin to drip out of the nuclei when $\rho \sim 4 \times 10^{11}$ g cm^{-3}. The pressure is still mostly from degenerate electrons.
- the outer core is composed primarily of superfluid neutrons and the neutrons supply most of the pressure through neutron degeneracy. Free superconducting protons are present too. This region of mainly neutrons is what gives the neutron star its name.
- the structure of the inner core is less certain than that of the outer layers of the NS because the equation-of-state for matter under super-dense conditions is not well understood.

A NS is an excellent object to test the physics of dense matter. Especially in the cores of the NSs, many exotic particles are expected to be formed, but the information from the central parts of the neutron star is hidden in the macroscopic properties such as neutron star masses and radii.
Masses of NSs at birth are tuned by the complex details of the astrophysical processes that drive core collapse and supernova explosions (Timmes et al. 1996). The maximum possible mass of a NS has attracted particular attention because it draws the boundary for the low-mass limit of stellar mass black holes (Rhoades & Ruffini 1974; Fryer & Kalogera 2001).

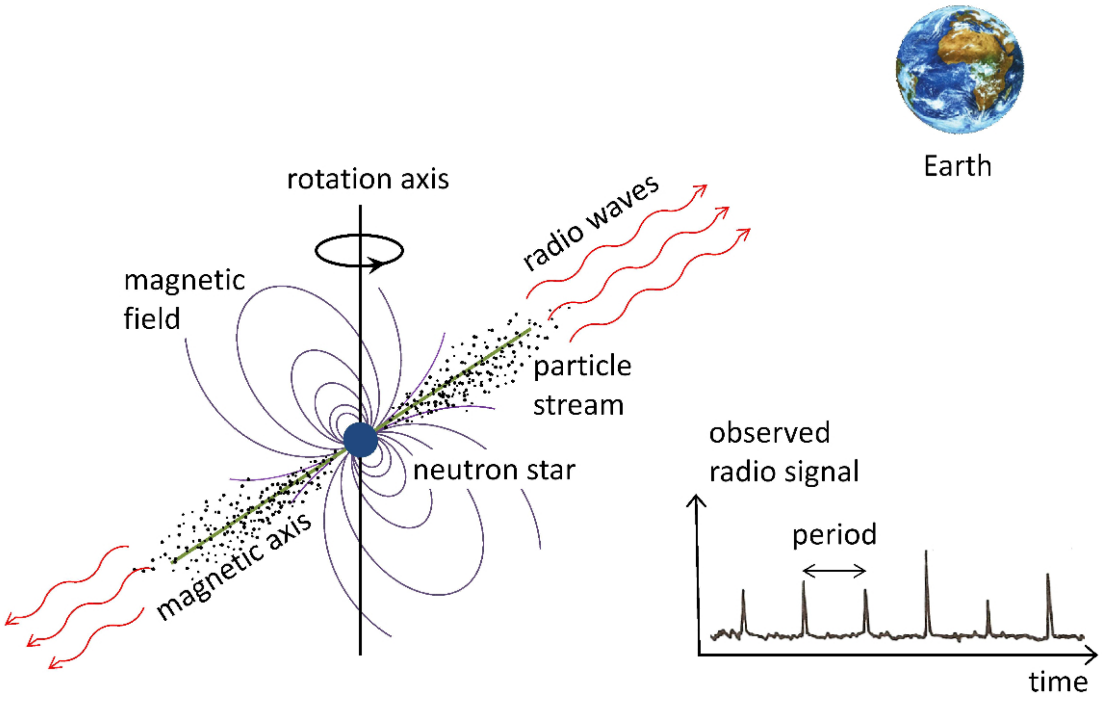

Figure 1.6: The pulsar lighthouse model. The rotating neutron star emits a beam of radio waves from above the polar regions. A periodic signal is intercepted on Earth revealing the spin period of the pulsar. Figure from Tauris (2015).

1.5 Pulsars

Although NSs were theoretically predicted in 1933 (Baade & Zwicky 1934b,a), it was not until 1968 that the serendipitous discovery of radio pulsars (Hewish et al. 1968) pointed to rapidly rotating neutron stars as their most likely explanation. Since then, the number of known pulsars in the disk of our Galaxy increased to be more than 2600, with many applications in astrophysics. Some of these applications include the first indirect observational evidence for gravitational waves in the first binary pulsar discovered (Hulse & Taylor 1975), for which the Nobel price was awarded in 1993, the first observed extra-solar planetary system (Wolszczan & Frail 1992) or the first detection of gas in a globular cluster (Freire et al. 2001). Using pulsar timing arrays, one interesting application of pulsars is their use as a cosmic global positioning system that is capable of detecting the effects of passing gravitational waves (e.g. Hobbs et al. 2010).

Pulsars, rapidly rotating, highly magnetized neutron stars, are concentrated in the Galactic plane in star-forming regions though they have a large spread in their distribution perpendicular to the disk caused by their high velocities resulting from the supernova explosions.

Figure 1.6 shows a simplified model of the beamed emission of a pulsar known as the *light house model*. The physics underlying the pulsar emission mechanism is very complicated and not yet fully understood. As the neutron star spins, charged particles are accelerated along magnetic field lines. Via a cascade of pair creation processes, the accelerated particles eventually emit coherent electromagnetic radiation through curvature radiation, in most cases detected at radio frequencies. Usually one pulse per rotation is observed as the rotating emission crosses the observer's line of sight. The timing and pulse stability of some pulsars rivals terrestrial atomic clocks.

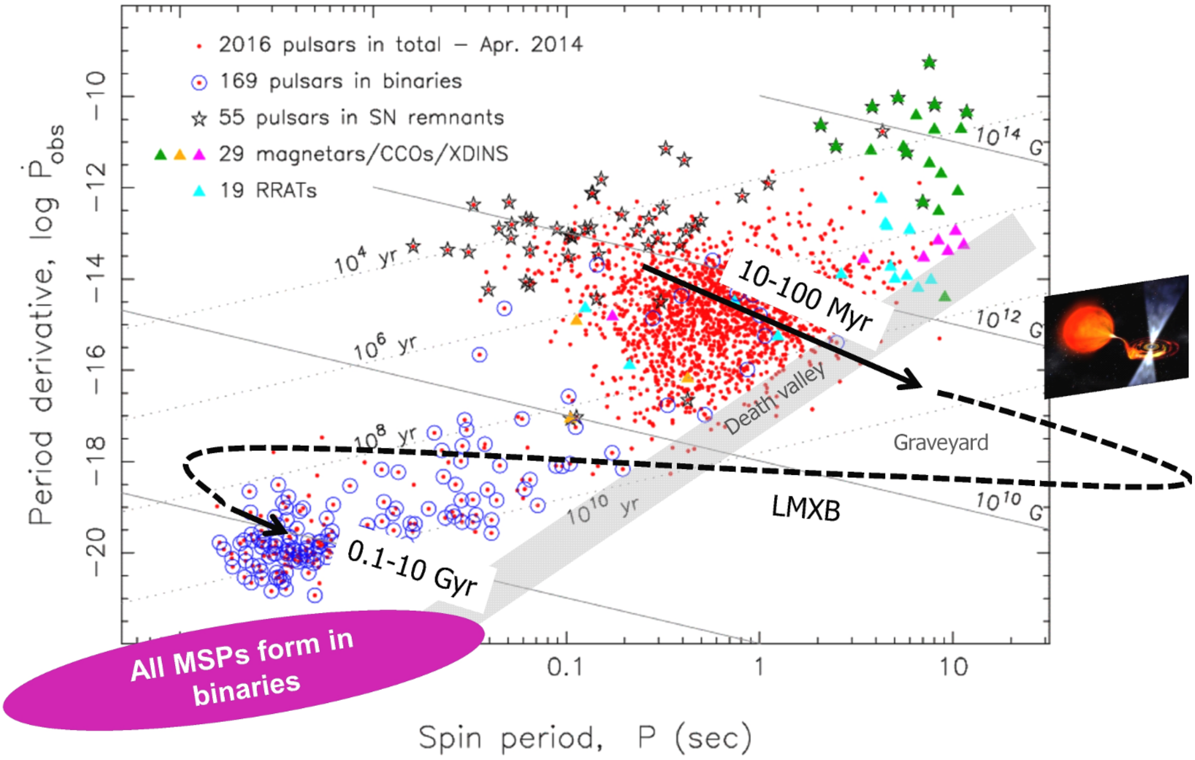

Figure 1.7: All currently known pulsars with measured P and $\dot{P}$. Data from the ATFN Pulsar Catalogue - April 2014. Lines of constant characteristic age and constant B-field are marked (figure from Tauris et al. (2015))

Most neutron stars have been discovered as radio pulsars but the vast majority of the energy emitted is as magnetic dipole radiation, rather than radio waves. In addition, very high-energy photons such as X-rays and γ-rays are emitted. Typically only about 10^{-6} of their radiated energy is in the radio-frequency spectrum.
The rotating neutron star model predicts a gradual slowdown and consequently an increase in the pulse period as the outgoing radiation carries away rotational kinetic energy.

1.5.1 Pulsar demography

Figure 1.7 shows all the radio pulsars known with measured values for spin period, P and its time derivative $\dot{P}$. This type of diagram is essential in understanding the formation and evolution of different observed types of pulsars. The different values of P of $\dot{P}$ imply fundamentally different magnetic fields strengths and ages. Assuming a pulsar can be described as a rotating magnetic dipole, one can show that the surface magnetic field strength is given by $B \propto (P\dot{P})^{1/2}$ and a *characteristic age* can be defined as $\tau_c = P/(2\dot{P})$. Three main populations of pulsars can be distinguished:

- *classic radio pulsars* (red dots) are concentrated in the region of the diagram with $P \simeq 0.2 - 2$ s and $\dot{P} \simeq 10^{-16} - 10^{-13}$ s s^{-1}. They have magnetic fields of the order B$\simeq 10^{10} - 10^{13}$ G and a lifetime as a radio source of a few 10^7 yr.

- *millisecond pulsars* (MSPs) represent a growing fraction of the discovered pulsars, around 10% of the pulsar population. With spin periods of 1.4 ms$\lesssim P \lesssim$ 30 ms and $\dot{P} \lesssim 10^{-19}$ s s^{-1} and relatively small magnetic field strengths, they represent the oldest population of neutron stars. The binary pulsars plotted in blue circles overlap with the millisecond pulsars, clearly indicating a connection between the two populations. As we will see, they have a different formation scenario from the normal pulsars.

- *magnetars* are found in the upper corner of the diagram and are characterized, as the name suggests, by huge magnetic fields even for pulsars standards. They are very young objects and currently 28 of them are known. They can occasionally have outbursts of X-rays and soft gamma−rays believed to originate from the decay of an intense internal magnetic field which causes stresses and fractures of the stellar crust (Thompson & Duncan 1995).

Millisecond pulsars are thought to be born in the region of the $P\dot{P}$-diagram populated by the normal pulsars. After 10−100 Myr, the radio emission becomes so faint that is not detectable anymore and the pulsar now moves into a region of the diagram called "the graveyard", where no, or very few, pulsars are observed. But luckily some of these pulsars are part of a binary system. At some point, they will start feeding on their companions and, due to the accretion of matter and angular momentum they will be "born again" (recycled) as a MSP.

1.5.2 The population of binary millisecond pulsars

It is believed that all MSPs must form in binary systems, although isolated MSPs have been found. One idea is that the companions of the (later isolated) MSPs are ablated away by energetic particles and γ-rays produced by the pulsar wind. This idea was inspired by the discovery of the original black widow pulsar B1957+20 (Fruchter et al. 1988), an eclipsing 1.6 ms pulsar in a 9.1 hr orbit around a very low mass companion, $\sim 0.02\ \mathrm{M}_{\odot}$.

Shortly after the discovery of the first MSP, B1937+21, Alpar et al. (1982) proposed that radio MSPs are the end product of the accretion process we see today in X-ray binaries. Accreting X-ray binaries were discovered in the 1970's (Giacconi et al. 1971) and are among the most luminous objects in the X-ray sky. In X-ray binaries, matter is accreted from a donor star onto a compact object (white dwarf, neutron star or black hole). X-ray emission originates as a result of the conversion of the gravitational binding energy of the accreted mater into kinetic energy. In this type of binary systems, the neutron star is spun-up to a high spin frequency via accretion of mass and angular momentum once the secondary star evolves (Alpar et al. 1982; Radhakrishnan & Srinivasan 1982; Bhattacharya & van den Heuvel 1991). During this recycling phase the system is observable as an X-ray binary (e.g. Nagase 1989; Bildsten et al. 1997) and towards the end of this phase as an X-ray millisecond pulsar (Wijnands & van der Klis 1998; Archibald et al. 2009). Although this scenario is now commonly accepted, there are many aspects that are not yet fully understood such as the mass-transfer process and the accretion physics.

All MSPs possess a low surface magnetic flux density B of the order of 10^8 G, about 3−5 orders of magnitude less than the B-fields of the ordinary, non-recycled pulsars. Therefore, the recycled pulsars do not suffer as much from loss of rotational energy due to emission of magnetic dipole radiation. Hence, MSPs have small period derivatives $\dot{P} < 10^{-18}$ s/s and are capable to maintain the production of radio waves for billion of years.

Depending on the nature of the companion star, recycled pulsars are believed to form from low-mass X-ray binaries (LMXBs), where the donor is a low-mass star, intermediate-mass X-ray binaries (IMXBs), where the donor is a intermediate-mass star with a mass typically between 3−6 $\mathrm{M}_{\odot}$ or high-mass X-ray binaries (HMXBs), where the donor is a high-mass star $\gtrsim 8\ \mathrm{M}_{\odot}$ (Tauris & van den Heuvel 2006; Tauris 2011; Tauris et al. 2012). The total population of known X-ray binaries in our Galaxy exceeds over 300 sources (Liu et al. 2007; Chaty 2013).

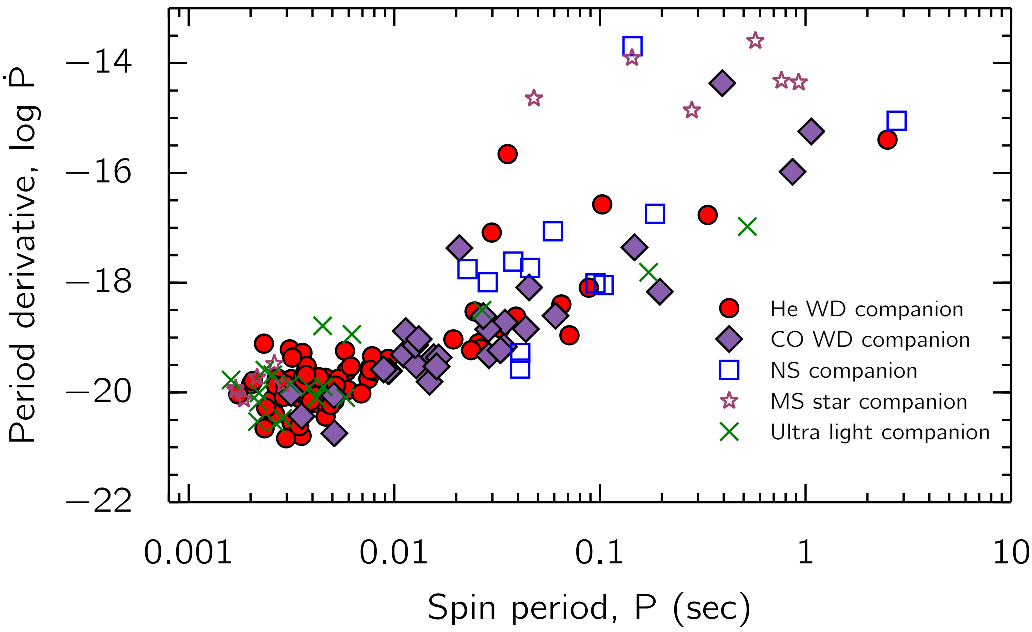

Figure 1.8: Distribution of ~180 binary radio pulsars with measured values in the $P - \dot{P}$ diagram (Tauris et al. 2012). The symbols indicate the nature of the companion star. Data taken from the ATNF *Pulsar Catalogue* (Manchester et al. 2005) in December 2015.

For each of these classes of X-ray binaries, the evolutionary status of the donor star, or equivalently the orbital period at the onset of the Roche-lobe overflow, is the determining factor for the outcome of the mass-transfer phase and thus the nature of the MSP formed (Tauris 2011). The discovery of several X-ray pulsars with millisecond periods in LMXBs and of IGR J18245-2452, an LMXB with a rotation period of 3.9 ms that alternates between a rotation-powered radio source and an accretion-powered X-ray source (Papitto et al. 2013), have provided strong evidence in support of the recycling scenario.

To understand the formation scenario of MSPs, one needs to analyze the properties of the observed companions of such systems and reconstruct the initial conditions of their progenitors. Binary pulsars in globular clusters are in general not suitable as tracers of their stellar evolution history because of the frequent encounters and exchanges of companion stars in the dense environments (Ransom et al. 2005). Figure 1.8 shows the location of the radio binary pulsars in the $P - \dot{P}$ diagram with various symbols denoting the type of companion star. The lower left corner of the diagram is populated with the so-called fully recycled MSPs, with spin periods $P < 10$ ms. The majority of them have He WDs companions, but some systems harbour ultra-light semi-degenerate companions in the so called *black widow* systems as well as more massive CO white dwarfs. The mildly recycled MSPs, 10 ms $< P <$ 100 ms are dominated by CO (and ONeMg) WDs and NS companions.

In general, binary systems with WD companions have essentially circular orbits: $10^{-7} \lesssim e \lesssim 0.01$. Binary pulsars with NS or main-sequence companions tend to have more eccentric orbits, $0.10 \lesssim e \lesssim 0.9$ (Phinney 1992; Tauris et al. 2011).

An important diagram in understanding the various progenitors of MSPs is shown in figure 1.9, where one plots the binary orbital period as a function of the companion mass. A review discussing the characteristics and the formation classes of all MSPs can be found in Tauris (2011).

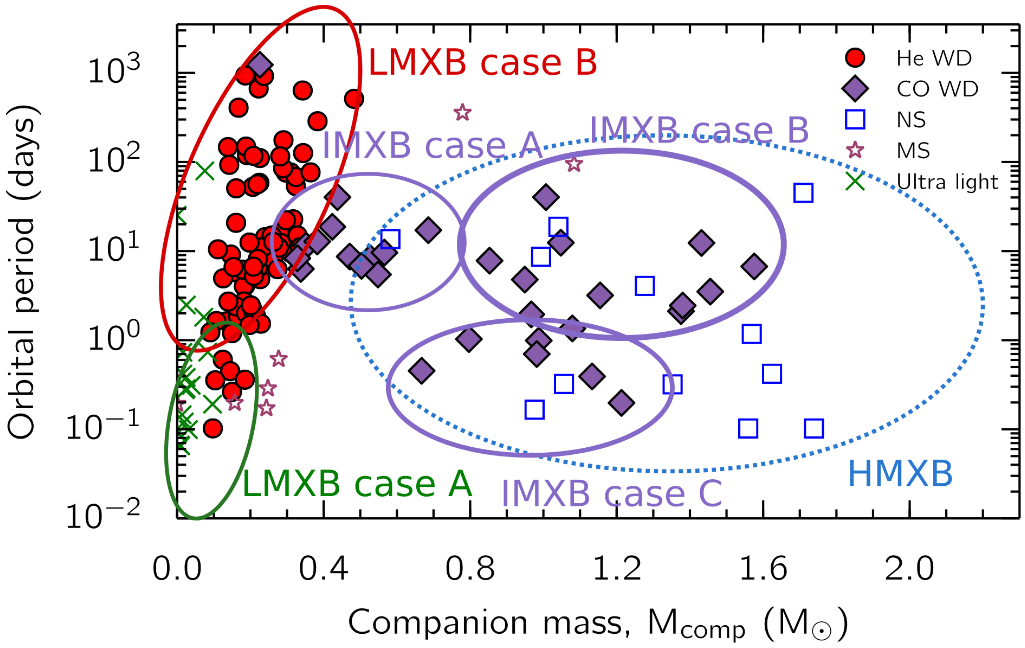

Figure 1.9: Distribution of ~180 binary radio pulsars with measured values in the companion mass-orbital period plane. The symbols indicate the nature of the companion star. Also shown are the types of progenitor binaries. Data taken from the ATNF *Pulsar Catalogue* (Manchester et al. 2005) in December 2015. See also Tauris (2011).

1.6 This thesis

In this thesis, we investigate two main problems: (i) the formation and evolution of MSPs in compact orbits with low-mass helium WD companions descending from LMXBs, see Chapter 2 and (ii) the thermal properties of the donor star in an LMXB system from the end of the mass transfer phase to the WD cooling track, as function of mass, metallicity and different input physics, see Chapter 3 and 4.

1.6.1 Millisecond pulsars in very compact orbits

Figure 1.10 shows schematically an evolutionary sequence leading the formation of an MSP in a very compact orbit. In a binary with a massive star and a low-mass companion, mass transfer will become dynamically unstable leading to a common-envelope phase. After the common envelope, a naked helium star will be left behind that will eventually explode in a supernova event giving birth to a NS. If the supernova explosion did not disrupt the binary, a NS will be orbiting the low-mass star. The evolutionary phases until the formation of the NS are very fast compared to the further evolution (cf. Section 1.4). The further evolution of the newly formed NS and the low-mass main sequence star depends very much on the orbital separation, which in turn dictates on which timescale the subsequent mass transfer will proceed, a nuclear timescale or a timescale defined by the loss of orbital angular momentum. If the orbital separation is small, the loss of orbital angular momentum will bring the stars closer together until the low-mass star fills its Roche-lobe and material is being transferred to the neutron star.

At the onset of the mass transfer phase, the donor star may be at the end of the main sequence or it just started hydrogen burning in a shell. In wider systems, the star will expand until it fills its Roche-lobe on the red-giant branch. If the orbital separation is very large (several years), the low-mass star basically evolves as a single star.

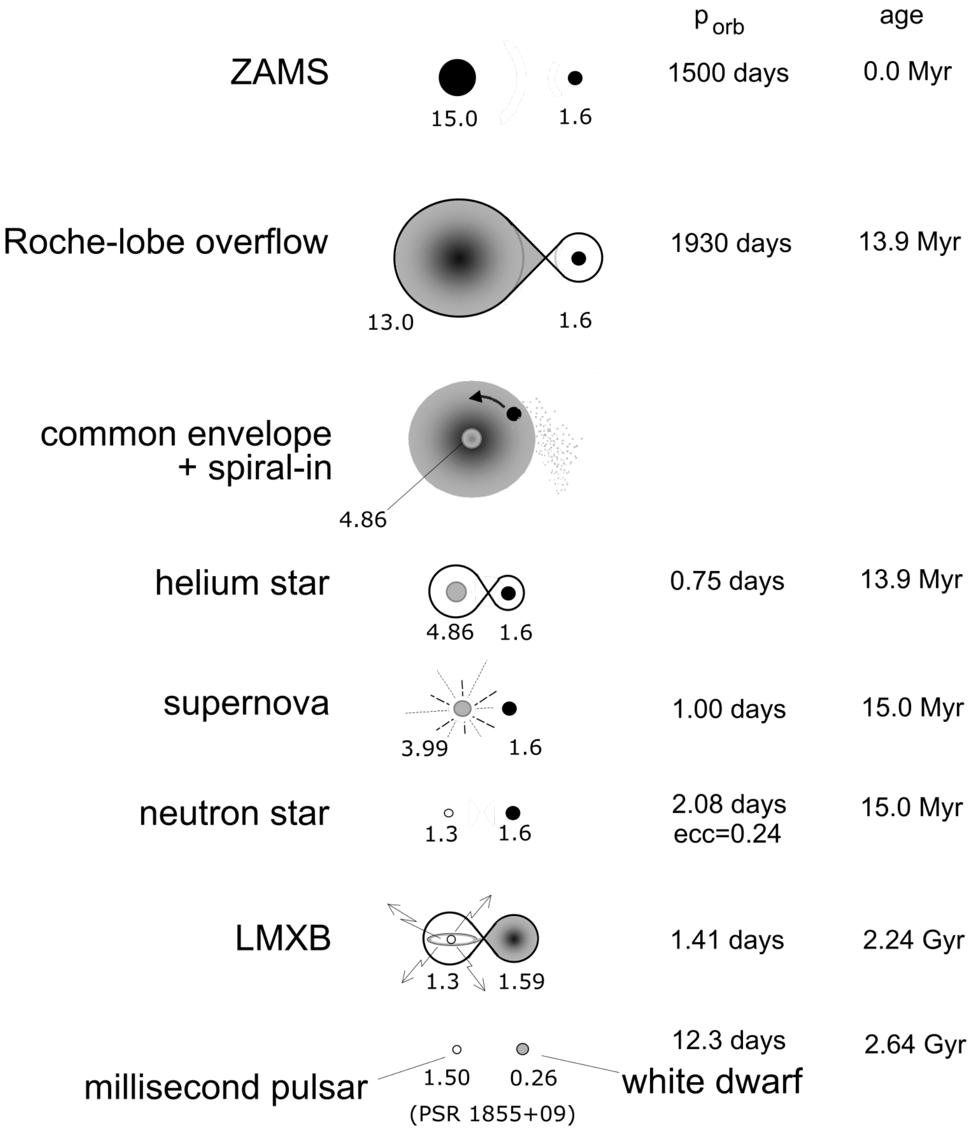

Figure 1.10: The evolution of a binary system which will lead to a LMXB and finally to the formation of a MSP with a WD companion. The evolution is governed by the specific orbital angular momentum treatment, the common envelope and spiral-in phase, the asymmetric supernova explosion and the stellar evolution of the helium star. The parameter shown on the right are rough predictions for the formation of PSR 1855+09. Cartoon adapted from Tauris & van den Heuvel (2006).

For binaries with low-mass stars, there are several mechanisms responsible for the removal of the orbital angular momentum: *gravitational wave radiation*, *mass transfer* and *magnetic braking* by a stellar wind, cf. Chapter 2. The low-mass donor is assumed to posses a magnetic stellar wind, similar to a solar wind which is forced to corotate to large distances. In this way, the wind removes angular momentum from the star by exerting a torque with a long lever arm. In a close binary system, the donor is assumed to be tidally locked and synchronously rotate with the orbital motion, and thus removal of spin orbital momentum from the star removes angular momentum from the orbit. This effect of a magnetic stellar wind was observed in low-mass stars by Skumanich (1972) which showed that low-mass main sequence stars are rotating slower with time, $\Omega \propto t^{-\frac{1}{2}}$. The treatment of the loss of orbital angular momentum by magnetic braking of such stars in a binary is one of the biggest uncertainties in the evolution of low-mass X-ray binaries, cf. Chapter 2 .

It has been shown by Pylyser & Savonije (1988) that a critical initial orbital period exists at the onset of the Roche-lobe overflow, the so called *bifurcation period*, $P_{\rm bif}$. This bifurcation period separates the formation of *converging* LMXBs, those with final orbital period smaller than initial orbital from *diverging* LMXBs, which have a final orbital period much larger than the initial one. The theoretical estimated value of $P_{\rm bif}$ is $\sim$ 1 day, but it strongly depends on the treatment of tidal interactions and the assumed strength of magnetic braking which drains the system of orbital angular momentum (e.g. van der Sluys et al. 2005a; Ma & Li 2009). This distinction regarding the orbital period evolution is important as it determines the nature of the MSP companion. In converging systems, the remnant of the low-mass star will be a sub-stellar dwarf object which eventually might be completely destroyed leaving behind an isolated MSP. The diverging systems will produce He WDs with masses dependent on the final orbital separation.

Chapter 2 is focused on the the formation scenario of MSPs in very tight orbits with extremely low-mass He white dwarfs, $M \lesssim 0.2\ M_\odot$ (those populating the lower left corner of the diagram in figure 1.9) assuming different strengths of the magnetic braking law.

1.6.2 Formation and evolution of extremely low-mass helium white dwarfs

Extremely low-mass helium white dwarf (ELM WD) is a term recently used in the literature to denote a WD with surface gravity $5 < \log g < 7$ and effective temperature $8,000\ \mathrm{K} \lesssim\ T_{\rm eff} \lesssim\ 22,000\ \mathrm{K}$. This definition is based on the fact that WDs with these characteristics are nearly absent in major spectroscopic WD catalogues (Brown et al. 2016). From a theoretical point of view, such objects are low-mass helium-core WDs with masses below roughly 0.3 $M_\odot$. They are most likely the result of binary interactions (Marsh et al. 1995a), as the remnant of a single star evolution will be much older than the current age of the Universe, unless they are formed in very high metallicity environment (Kilic et al. 2007).

After the mass-transfer process ends, the remnant of the donor star will go through a proto-WD phase in which hydrogen burning continues in a shell surrounding the helium core. Depending on the included physics and metallicity, there is a certain range of WDs masses for which the residual hydrogen burning in the envelope is unstable, giving rise to the so-called hydrogen shell flashes. The occurrence of these hydrogen shell flashes greatly reduces the hydrogen envelope mass such that, once on the cooling track, these objects will have an accelerated cooling compared to the proto-WDs which experienced stable hydrogen burning. However, many details of this proto-WD phase are unclear and these are investigated in Chapters 3 and 4. An extended review of ELM WDs is given by Heber (2016).

In the last several years, the number of discovered ELM WDs increased drastically due to the ELM survey (Brown et al. 2010; Kilic et al. 2011; Brown et al. 2012; Kilic et al. 2012; Brown et al. 2013; Gianninas et al. 2015; Brown et al. 2016). The ELM survey is a dedicated survey of finding ELM WDs through broadband color selection from the SDSS database. Once such candidates are found, they are confirmed through follow-up spectroscopy observations, as the hydrogen lines provide a sensitive measure of surface gravity in this effective temperature range (Brown et al. 2016).

The population of companions found orbiting an ELM WD is a rather diverse one. The majority of companions are CO WDs, but ELM WDs have also been found in systems with MSPs (e.g. van Kerkwijk et al. 1996; Kaplan et al. 2013; Antoniadis et al. 2013), sdB stars as well as main-sequence stars, the so called EL CVn systems (e.g. Maxted et al. 2014b). Moreover, they are found in different environments, from the Galactic plane to globular and open clusters, implying that the metallicity of their progenitors spans a wide range.

Brown et al. (2016) showed that the sample of ELM WDs discovered by the ELM survey [9] has a log-normal distribution of orbital periods with a median period of 5.4 hr and that the binary companions have a normal distribution of masses with a median of 0.76 $M_{\odot}$ and a dispersion of 0.25 $M_{\odot}$. This indicates that 95% of the ELM WD systems have a total mass below the Chandrasekhar mass and most likely their evolution does not lead to a Type Ia supernova. As half of these systems will merge within 6 Gyr due to gravitational wave radiation, the probable outcome includes single massive white dwarfs and AM CVn binaries.

Due to their compact orbits, some of the ELM WDs are strong gravitational wave emitters. The most interesting system is the P=765 s detached eclipsing WD binary J0651, which is a gravitational wave source 10,000 times stronger than the Hulse-Taylor pulsar (Brown et al. 2011; Hermes et al. 2012a).

Six of the observed ELM WDs show multiperiodic light variations with periodicities between 1300 s to 7000 s, associated with g-mode pulsations (Hermes et al. 2012c, 2013c,a). Detailed theoretical studies (Steinfadt et al. 2010a; Córsico et al. 2012; Van Grootel et al. 2013a; Córsico & Althaus 2014a) showed that these ELM WD pulsators extend the ZZ Ceti instability strip to lower effective temperatures and higher luminosities. The discovery of these pulsators is important because they provide new constraints (especially for the hydrogen envelope mass on the cooling track) for theoretical models of ELM WDs.

One puzzling question regarding the evolution of ELM WDs is the observed presence of metals in their spectra (Gianninas et al. 2014a). In these type of objects, surface gravity is strong enough such that the gravitational settling will produce pure hydrogen envelopes. The observed metals therefore suggest that another process acts on the surface layers of these objects, counteracting the settling of elements heavier than hydrogen. Another piece of evidence of such a process acting against the gravitational settling in ELM proto-WDs is the recent discovery of three ELM proto-WDs pulsators (Gianninas et al. 2016), which is the first empirical evidence that pulsations in ELM proto-WDs can only occur if these objects have a mixed H/He atmosphere. The current available theoretical models predict that ELM proto-WDs have pure hydrogen atmospheres, in contradiction with the recent observational data. In Chapter 4 we present new evolutionary models in which we take into account, for the first time, the effect of rotational mixing on the evolution of proto-WDs, in an effort of reconciling the observational data with theoretical models.

---

[9] currently containing 76 ELM-WDs

CHAPTER 2

The formation of low-mass helium white dwarfs orbiting pulsars

Evolution of low-mass X-ray binaries below the bifurcation period

Alina G. Istrate, Thomas M. Tauris and Norbert Langer

Astronomy & Astrophysics, 2014, 571, 45

Abstract Millisecond pulsars (MSPs) are generally believed to be old neutron stars (NSs) that have been spun up to high rotation rates via accretion of matter from a companion star in a low-mass X-ray binary (LMXB). This scenario has been strongly supported by various pieces of observational evidence. However, many details of this recycling scenario remain to be understood. Here we investigate binary evolution in close LMXBs to study the formation of radio MSPs with low-mass helium white dwarf companions (He WDs) in tight binaries with orbital periods $P_{\mathrm{orb}} \simeq 2-9$ hr. In particular, we examine i) if the observed systems can be reproduced by theoretical modelling using standard prescriptions of orbital angular momentum losses (i.e. with respect to the nature and the strength of magnetic braking), ii) if our computations of the Roche-lobe detachments can match the observed orbital periods, and iii) if the correlation between WD mass and orbital period (M_{WD}, P_{orb}) is valid for systems with $P_{\mathrm{orb}} < 2$ days. Numerical calculations with 5 detailed stellar evolution code were used to trace the mass-transfer phase in ~400 close LMXB systems with different initial values of donor star mass, NS mass, orbital period, and the so-called γ-index of magnetic braking. Subsequently, we followed the orbital and the interior evolution of the detached low-mass (proto) He WDs, including stages with residual shell hydrogen burning. We find that severe fine-tuning is necessary to reproduce the observed MSPs in tight binaries with He WD companions of mass $< 0.20\ M_{\odot}$, which suggests that something needs to be modified or is missing in the standard input physics of LMXB modelling. Results from previous independent studies support this conclusion. We demonstrate that the theoretically calculated (M_{WD}, P_{orb})–relation is in general also valid for systems with $P_{\mathrm{orb}} < 2$ days, although with a large scatter in He WD masses between $0.15 - 0.20\ M_{\odot}$. The results of the thermal evolution of the (proto) He WDs are reported in a follow-up paper (Paper II).

2.1 Introduction

Millisecond pulsars (MSPs) belong to a class of radio pulsars characterized with high rotational spin rates and low magnetic fields. Most of them are observed in binary systems and it is thought that they spin rapidly because of mass accretion from a companion star in a process known as recycling (Bhattacharya & van den Heuvel 1991; Tauris & van den Heuvel 2006). The first MSP was discovered in 1982 (Alpar et al. 1982) and today 171 fully recycled MSPs[1] are known in our Galaxy, of which 60 are found inside globular clusters and 111 are in the Galactic field. The orbital periods of binary MSP systems in the Galactic field range from $P_{\rm orb}$ = 93 min to 175 days, while the companion masses can be as low as 0.02 $M_\oplus$ (tiny planets) or as high as $\approx$ 1.3 $M_\odot$ (massive white dwarfs).

MSPs in binaries can be subdivided into several classes according to the nature of their companion which can be either a degenerate or a non-degenerate object. Degenerate companions include helium white dwarfs (He WDs) and carbon-oxygen white dwarfs (CO WDs), while the non-degenerate (or semi-degenerate) ones are often low-mass dwarf stars (or brown-dwarf like remnants) which have suffered from significant mass loss and ablation from the pulsar wind (cf. the so-called black widow and redback systems in Roberts 2013 and Chen et al. 2013. The progenitors of most MSP systems are low-mass X-ray binaries (LMXBs), except for the MSPs with the more massive CO/ONeMg WDs which are produced from intermediate-mass X-ray binaries (IMXBs) – see Tauris (2011) for a review. Pulsars with another neutron star (NS) companion are produced in high-mass X-ray binaries. Most NSs in all flavours of binary pulsar systems are produced via supernovae (SNe) of Type Ib/c, given that their progenitors must have lost their hydrogen-rich envelopes via mass transfer in a relatively close orbit prior to the explosion.

It has been shown by Pylyser & Savonije (1988, 1989) that a critical initial orbital period (the so-called bifurcation period, $P_{\rm bif}$) exists at the onset of Roche-lobe overflow (RLO), separating the formation of converging LMXBs from diverging LMXBs, which shorten and widen their orbits, respectively. The theoretical estimated value of $P_{\rm bif}^{\rm RLO}$ is $\sim$ 1 day, but depends strongly on the treatment of tidal interactions and the assumed strength of magnetic braking which drains the system of orbital angular momentum (e.g. van der Sluys et al. 2005a; Ma & Li 2009). The observed MSPs with $P_{\rm orb} > 1$ day originate from relatively wide orbit LMXBs where the donor star did not fill its Roche lobe until it had evolved and expanded to become a (sub)giant, i.e. Case B RLO (e.g. Rappaport et al. 1995; Tauris & Savonije 1999; Podsiadlowski et al. 2002).

In this work, we concentrate on investigating the evolutionary path of MSPs with He WD companions in very narrow orbits. There are four such systems known which have orbital periods, $P_{\rm orb} < 9$ hr and WD masses of $0.13 < M_{\rm WD}/M_\odot \lesssim 0.21$. Having low-mass companions and $P_{\rm orb} < 1$ day, these systems thus descend from LMXBs in tight orbits where the donor star already initiated RLO while it was still on the main sequence (Case A RLO). As a result of their compact nature, these systems emit gravitational wave radiation and eventually evolve to become primary candidates for strong gravitational wave sources to be detected by eLISA in the mHz frequency range (Nelemans 2009). In Section 3.4 we list the detailed observational properties of the investigated systems. Our binary stellar evolution code is introduced in Section 2.3, and the results of the numerical calculations for the LMXBs systems are presented in Section 2.4. In Section 2.5 we discuss our findings with an emphasis on magnetic braking and the ($M_{\rm WD}$, $P_{\rm orb}$)–relation. Our conclusions are given in Section 5. In Paper II (Istrate et al. 2014b) we explore the early evolution of the detached (proto) He WDs.

2.2 Observational properties of MSPs with He WDs in tight orbits

The observed properties of the binary MSPs on which we focus our attention here are described below (see also Table 2.1).

PSR J0348+0432 is an interesting recycled pulsar with a relatively slow spin period, $P = 39.1$ ms in a binary system with an orbital period of $P_{\rm orb} = 2.46$ hr. Recently, Antoniadis et al. (2013) found that

---

[1] According to the ATNF Pulsar Catalogue (Manchester et al. 2005), version 1.50 (June 2014). Here we define MSPs as pulsars with a spin period, $P < 20$ ms. The typical measured value of the associated period-derivative is $\dot{P} < 10^{-18}$.

Table 2.1: Observed MSPs with He WD companions in tight circular orbits. The top four systems have $P_{\rm orb} < 9$ hr (i.e. solutions) and are found in the Galactic field. The bottom six systems are intermediate systems with $P_{\rm orb} = 9 - 15$ hr, of which five systems are located in globular clusters.

Pulsar name	$P_{\rm orb}$ (hr)	$M_{\rm WD}$ ($M_\odot$)	$M_{\rm NS}$ ($M_\odot$)	eccentricity	$P_{\rm spin}$ (ms)	$\dot{P}$ (s s^{-1})	WD age (Gyr)	Optical data reference
PSR J0348+0432	2.46	0.17	2.01	2.6×10^{-6}	39.1	2.41×10^{-19}	2.1 ± 0.5	Antoniadis et al. (2013)
PSR J0751+1807	6.31	0.14	1.34	7.1×10^{-7}	3.48	7.79×10^{-21}	–	Lundgren et al. (1995)
PSR J1738+0333	8.52	0.18	1.47	4.0×10^{-6}	5.85	2.41×10^{-19}	–	Antoniadis et al. (2012)
PSR J1816+4510	8.66	0.21^a	2.0^a	8×10^{-6}	3.19	4.31×10^{-20}	–	Kaplan et al. (2013)
PSR J0024−7204U	10.3	0.15^b	1.5^b	$< 10^{-4}$	4.34	–	0.6	Edmonds et al. (2001)
PSR J1748−2446M	10.6	0.17^b	1.5^b	$< 10^{-4}$	3.57	–	–	
PSR J1748−2446V	12.1	0.15^b	1.5^b	$< 10^{-4}$	2.07	–	–	
PSR J0024−7204Y	12.5	0.17^b	1.5^b	$< 10^{-4}$	2.20	–	–	
PSR J1641+3627D	14.2	0.22^b	1.5^b	$< 10^{-4}$	3.12	–	–	
PSR J1012+5307	14.5	0.16	1.64	$< 8.4 \times 10^{-7}$	5.26	1.71×10^{-20}	–	Callanan et al. (1998)

[a] This value is very uncertain. Kaplan et al. (2013) find $M_{\rm WD} \sin^3 i = 0.193 \pm 0.012\ M_\odot$ and $M_{\rm NS} \sin^3 i = 1.84 \pm 0.11\ M_\odot$, where i is the unknown orbital inclination angle. Assuming $M_{\rm NS} \leq 2.0\ M_\odot$ yields $M_{\rm WD} \leq 0.21\ M_\odot$. From pulsar timing (Stovall et al. 2014) a strict lower limit on the minimum companion mass is $M_{\rm WD} = 0.16\ M_\odot$ (assuming $i = 90°$ and $M_{\rm NS} = 1.4\ M_\odot$).

[b] For these systems we estimated $M_{\rm WD}$ by assuming $M_{\rm NS} = 1.5\ M_\odot$ and an orbital inclination angle of 60°.

this pulsar is the most massive, precisely measured NS known with a mass of $M_{\rm NS} = 2.01 \pm 0.04\ M_\odot$, in orbit with a He WD companion of mass $M_{\rm WD} = 0.172 \pm 0.003\ M_\odot$. The estimated cooling age of the WD is about $\tau_{\rm cool} \sim 2$ Gyr. (In an upcoming paper, Paper III, we present our analysis for the formation of this system.)

PSR J0751+1807 is an MSP with $P = 3.48$ ms in a binary system with a He WD companion and $P_{\rm orb} = 6.31$ hr. Nice et al. (2008) estimated the masses of the pulsar and its companion to be $M_{\rm NS} = 1.26 \pm 0.14\ M_\odot$ and $M_{\rm WD} \simeq 0.15\ M_\odot$, respectively. Optical and near-IR spectroscopy of the WD reveals that it has a very low (ultra-cool) effective temperature $T_{\rm eff} \simeq 3500 - 4300$ K (Bassa et al. 2006b). The cooling age of the WD is not well determined since it depends critically on residual nuclear burning in its (presumably) thick hydrogen-rich envelope. In addition, although there are no signs of pulsar irradiation, heating from the pulsar cannot be excluded.

PSR J1738+0333 is another one of the handful of MSPs which have a He WD companion bright enough to make spectroscopic observations (Antoniadis et al. 2012). This system also has a very short orbital period (8.51 hr) making it a perfect laboratory for testing theories of gravity (Freire et al. 2012). The mass of the companion is $M_{\rm WD} = 0.181 \pm 0.006\ M_\odot$ and the NS mass is constrained to be $M_{\rm NS} = 1.47 \pm 0.07\ M_\odot$.

PSR J1816+4510 is an intriguing case. It is an eclipsing MSP recently discovered by Stovall et al. (2014) who performed a radio search of a Fermi γ-ray point source. The companion star to PSR J1816+4510 ($P_{\rm orb} = 8.7$ hr) was detected by Kaplan et al. (2012, 2013) who measured an effective temperature of $T_{\rm eff} = 16\,000 \pm 500$ K and estimated a companion mass of $M_{\rm WD} \sin^3 i = 0.193 \pm 0.012\ M_\odot$, where i is the orbital inclination angle of the binary. Despite of its low surface gravity ($\log g = 4.9 \pm 0.3$) they concluded that its spectrum is rather similar to that of a low-mass He WD. For the mass of the NS they estimated $M_{\rm NS} \sin^3 i = 1.84 \pm 0.11\ M_\odot$. Assuming that $M_{\rm NS} \leq 2.0\ M_\odot$ (i.e. less than the highest precisely measured NS mass known to date) this yields $M_{\rm WD} \leq 0.21\ M_\odot$. As we discuss in Section 2.4.5, however, based solely on its $P_{\rm orb}$, combined with modelling of the orbital period evolution of LMXBs, we would even expect $M_{\rm WD} \lesssim 0.18\ M_\odot$. (See also Paper II for further discussions on the nature of this companion star.)

In addition to these four systems, there are a number of MSPs with low-mass He WD companions and slightly larger $P_{\rm orb} = 9 - 15$ hr. Five of these MSPs are found in globular clusters. Usually, binary MSPs observed in dense environments like globular clusters are excluded from comparison to theoretical modelling of binaries because of the possibility that the observed MSP companion was exchanged via an encounter event. However, there are some MSPs found in globular clusters which have very small eccentricities ($e < 10^{-4}$, Paulo Freire, priv. comm.). This we take as good evidence that the present He WD companion is indeed the one which was the former donor star in the LMXB phase, and thus responsible for recycling the MSP. Therefore, we include these five MSPs in Table 2.1 as well.

Finally, we note that a number of low-mass He WDs ($\leq 0.20\ M_\odot$) with $P_{\rm orb} < 15$ hr are also found in double WD systems (e.g. Kaplan et al. 2014a, and references therein). These WDs often have a massive CO WD companion and evolved via stable RLO in cataclysmic variable (CV) systems. Although the structure and the properties of these low-mass He WDs are similar to the ones with radio pulsar companions, we restrict ourselves to the latter sources in this work (see, however, Paper II for further discussions of these systems).

To summarize, the systems described above all have similar properties: their $P_{\rm orb}$ is very short (in the range of $2 - 15$ hr), and the He WD companions have typical masses of $0.14 - 0.18\ M_\odot$. Given these characteristics, in this work we explore their formation paths (with a special focus on the systems with $P_{\rm orb} < 9$ hr) and discuss the underlying physical assumptions of the applied standard modelling for loss of orbital angular momentum via magnetic braking.

2.3 Numerical methods and physical assumptions

We consider as a starting point binary systems which consist of a NS orbiting a low-mass main-sequence star. Such systems are expected to have formed from zero-age main sequence (ZAMS) binaries with a massive ($\sim 10-25\ M_{\odot}$) primary star and a low-mass ($\sim 1-2\ M_{\odot}$) companion in a relatively close orbit, and which subsequently survived a common-envelope phase, followed by a supernova explosion (Bhattacharya & van den Heuvel 1991; Tauris & van den Heuvel 2006). Numerical calculations with a detailed stellar evolution code were then used in this study to trace the mass-transfer phase in roughly 400 close LMXB systems with different initial values of donor star mass, NS mass, orbital period and the so-called γ-index of magnetic braking. Subsequently, we followed the evolution of the low-mass (proto) He WD, including stages with residual hydrogen shell burning.

We used the BEC-code which is a binary stellar evolution code originally developed by Braun (1997) on the basis of a single-star code (Langer 1998, and references therein). It is a one-dimensional implicit Lagrangian code which solves the hydrodynamic form of the stellar structure and evolution equations (Kippenhahn & Weigert 1990). The evolution of the donor star, the mass-transfer rate, and the orbital separation are computed simultaneously through an implicit coupling scheme (see also Wellstein & Langer 1999) using the Roche-approximation in the formulation of Eggleton (1983). To compute the mass-transfer rate, the code uses the prescription of Ritter (1988). It employs the radiative opacities of Iglesias & Rogers (1996), which are interpolated in tables as a function of density, temperature, and chemical element mass fractions, including carbon and oxygen. For the electron conduction opacity, the code follows Hubbard & Lampe (1969) in the non-relativistic case, and Canuto (1970) in the relativistic case. The stellar models are computed using extended nuclear networks including the PP I, II, and III chains and the four CNO-cycles. Chemical mixing due to convection, semi-convection and overshooting is treated as a diffusion process. Thermohaline mixing is also included in the code (cf. Cantiello & Langer 2010), whereas gravitational settling and radiative levitation is not. Finally, the accreting NS is treated as a point mass.

A slightly updated version of this code for LMXBs and IMXBs has recently been applied to study the formation of MSPs (Tauris et al. 2011, 2012, 2013; Lazarus et al. 2014). In our models we assumed a mixing-length parameter of $\alpha = l/H_{\mathrm{p}} = 2.0$ and a core convective overshooting parameter of $\delta_{\mathrm{ov}} = 0.10$. Tauris et al. (2013) recently tested several models of wide-orbit LMXB evolution using $\alpha = l/H_{\mathrm{p}} = 1.5$ which resulted in only slightly smaller final WD masses ($\sim 1\%$), orbiting recycled pulsars in somewhat closer orbits (up to $\sim 3\%$ decrease in P_{orb}). The magnetic braking was implemented as outlined below.

2.3.1 Orbital angular momentum treatment

We considered the change in orbital angular momentum,

$$\frac{\dot{J}_{\mathrm{orb}}}{J_{\mathrm{orb}}} = \frac{\dot{J}_{\mathrm{ml}}}{J_{\mathrm{orb}}} + \frac{\dot{J}_{\mathrm{gwr}}}{J_{\mathrm{orb}}} + \frac{\dot{J}_{\mathrm{mb}}}{J_{\mathrm{orb}}}, \tag{2.1}$$

with contributions from mass loss, gravitational wave radiation, and magnetic braking, respectively.

Loss of orbital angular momentum due to mass loss

We solved the orbital angular momentum balance equation (e.g. eqn. 20 in Tauris & van den Heuvel 2006) using the isotropic re-emission model (Bhattacharya & van den Heuvel 1991; van den Heuvel 1994; Tauris 1996; Soberman et al. 1997). In this model matter flows over from the donor star (M_2) to the accreting NS (M_{NS}) in a conservative manner and thereafter a certain fraction, β of this matter is ejected from the vicinity of the NS with the specific orbital angular momentum of the NS. Hence, one can express the loss of orbital angular momentum due to mass loss as

$$dJ_{\rm ml} = \frac{J_{\rm NS}}{M_{\rm NS}}\beta\, dM_2 = \frac{\mu}{M_{\rm NS}^2}\, J_{\rm orb}\,\beta\, dM_2 \tag{2.2}$$

or

$$\frac{\dot{J}_{\rm ml}}{J_{\rm orb}} = \frac{\mu}{M_{\rm NS}^2}\beta\,\dot{M}_2 = \frac{\beta q^2}{1+q}\,\frac{\dot{M}_2}{M_2}\,, \tag{2.3}$$

where $\mu = M_{\rm NS}M_2/(M_{\rm NS}+M_2)$ is the reduced mass, and $q = M_2/M_{\rm NS}$ denotes the ratio between donor star mass and the mass of the NS accretor. Keep in mind that a fraction $1-\beta$ of the matter lost from the donor star is accreted onto the NS. The rate of wind mass loss from the low-mass donor star is negligible compared to the mass-loss rate via RLO.

Loss of orbital angular momentum due to gravitational wave radiation

The second term on the right-hand side of Eq. (2.1) gives the loss of orbital angular momentum due to gravitational wave radiation (Landau & Lifshitz 1971),

$$\frac{\dot{J}_{\rm gwr}}{J_{\rm orb}} = -\frac{32\,G^3}{5\,c^5}\,\frac{M_2 M_{\rm NS} M}{a^4}\,, \tag{2.4}$$

where G is the gravitational constant, c is the speed of light in vacuum, a is the orbital separation, and $M = M_{\rm NS} + M_2$ is the total mass of the system. The validity of this mechanism has been beautifully demonstrated in PSR 1913+16, which is considered as an ideal gravity laboratory (e.g. Weisberg et al. 2010). For sufficiently narrow orbits the above equation becomes the dominant term in Eq. (2.1), causing a to decrease. Gravitational wave radiation is the major force driving the mass transfer in very narrow binaries, such as CVs (below the period gap) and ultra-compact X-ray binaries (Faulkner 1971; van Haaften et al. 2012). Therefore, the orbits of very narrow LMXBs will tend to continuously shrink (i.e. converging systems) until a period minimum is reached, before hydrogen burning is exhausted and the donor star becomes fully degenerate (Paczynski & Sienkiewicz 1981; Rappaport et al. 1982; Nelson et al. 1986; Podsiadlowski et al. 2002; Lin et al. 2011). At this point the donor star has a mass of typically $M_2 \approx 0.05 - 0.07\ M_\odot$ and $P_{\rm orb} \approx 40 - 80$ min. The subsequent evolution causes the orbit to widen because of the extreme mass ratio between the small donor star mass and the accreting NS. According to modelling of LMXBs (e.g. Benvenuto et al. 2012; Chen et al. 2013), the subsequent ablation of the donor star from the pulsar wind leads to the production of the so-called black widow pulsars which have companion star masses of a few 0.01 $M_\odot$ and $P_{\rm orb} \approx 2 - 10$ hr (Fruchter et al. 1988; Stappers et al. 1996; Roberts 2013). These systems may eventually form pulsar planets (Wolszczan & Frail 1992) or become isolated MSPs (Backer et al. 1982).

Loss of orbital angular momentum due to magnetic braking

In synchronized binaries with low-mass stars ($\lesssim 1.5\ M_\odot$), the loss of spin angular momentum due to a magnetic wind occurs at the expense of the orbital angular momentum (e.g., Mestel 1968; Verbunt & Zwaan 1981). However, a fundamental law of angular momentum loss is unknown for rapidly rotating stars. To compute the angular momentum loss due to magnetic braking, we adopt the prescription of

Rappaport et al. (1983),

$$\frac{\dot{J}_{\rm MB}}{J_{\rm orb}} = -3.8 \times 10^{-30}\, f\, \frac{R_\odot^4\ (R_2/R_\odot)^\gamma\ GM^2}{a^5\ M_{\rm NS}} \qquad {\rm s}^{-1}\,, \tag{2.5}$$

where R_2 is the radius of the donor star, f is scaling factor (of the order of unity) and γ is the magnetic braking index. Here, we have investigated the effect of systematically applying various values of γ between 2 and 5. Larger values of γ seem to produce too strong magnetic braking compared to observations of low-mass stars in open clusters (cf. Section 2.5.1 where we discuss the nature of the magnetic braking law).

The net effect of applying the above prescription for magnetic braking is that the orbital period of close binaries ($P_{\rm orb} \simeq 2 - 5$ days) typically decreases by a factor of three (depending on γ) prior to the RLO, i.e. magnetic braking causes orbital decay and forces the donor star to fill its Roche lobe and initiate mass transfer already on the main sequence or early into the Hertzsprung gap.

To optimize the analysis of our investigation and to enable us to better interpret the results in a coherent manner, we have simply assumed magnetic braking to operate in all our binaries (which have donor star masses $1.1 \leq M_2/M_\odot \leq 1.6$) at all times between the ZAMS and until the end of our calculations.

2.3.2 Mass accretion rate and accretion efficiency

The accretion rate onto the NS is assumed to be Eddington limited and is given by

$$\dot{M}_{\rm NS} = \left(\min\left[|\dot{M}_2|,\ \dot{M}_{\rm Edd}\right]\right)\ e_{\rm acc}\ k_{\rm def}\,, \tag{2.6}$$

where $e_{\rm acc}$ is the fraction of matter transferred to the NS which actually ends up being accreted and remains on the NS, and $k_{\rm def}$ is a factor that expresses the ratio of gravitational mass to rest mass of the accreted matter (depending on the equation-of-state of supranuclear matter, $k_{\rm def} \simeq 0.85 - 0.90$; e.g. Lattimer & Prakash 2007). The accretion efficiency of MSPs formed in LMXBs has been shown to be about 30% in several cases (Tauris & Savonije 1999; Jacoby et al. 2005; Antoniadis et al. 2012; Tauris & van den Heuvel 2014), even in close systems where the mass-transfer rate is expected to be sub-Eddington ($|\dot{M}_2| < \dot{M}_{\rm Edd}$) at all times. Hence, as a default value we assumed a NS accretion efficiency of $\epsilon = e_{\rm acc}\ k_{\rm def} = 0.30$. Accretion disk instabilities (e.g. van Paradijs 1996; Dubus et al. 2001; Coriat et al. 2012), which act to decrease the accretion efficiency in LMXBs, were not considered explicitly in this work, but are assumed to be integrated in the somewhat low accretion efficiency quoted above. Other mechanisms for inefficient accretion include propeller effects (Illarionov & Sunyaev 1975) and direct irradiation of the donor's atmosphere by the pulsar (see Section 2.5.3 for further discussions). We calculated the Eddington mass-accretion rate using

$$\dot{M}_{\rm Edd} = 2.3 \times 10^{-8}\ M_\odot\,{\rm yr}^{-1}\ \left(\frac{M_{\rm NS}}{M_\odot}\right)^{-1/3}\ \frac{2}{1+X}\,, \tag{2.7}$$

where X is the hydrogen mass fraction of the accreted material.

2.4 Results

2.4.1 Parameters of the model grid

In this work, we created a grid of models for LMXBs consisting of different initial donor star masses and NS masses, as well as for different values of the magnetic braking index, γ (see Fig. 2.1). For each of these sets of parameters we tried a range of initial orbital periods, $P_{\rm orb}$ in a systematic survey, yielding a total of roughly 400 models. More specifically, we chose the initial donor mass, M_2 between 1.1 and 1.6 $M_\odot$ (all with a metallicity of $Z = 0.02$). The lower mass limit is chosen to ensure nuclear evolution within a Hubble time. However, we find that $M_2 \geq 1.2\ M_\odot$ is often required for the stars to evolve through the LMXB phase and settle on the WD cooling track within a Hubble time. The upper mass limit is imposed by the requirement of a convective envelope on the ZAMS, which is an assumption needed to operate a magnetic wind. Although the 1.4 – 1.6 $M_\odot$ donors are borderline cases in this respect, we included them in our grid for comparison with previous studies in the literature. For the NSs, we applied initial masses of $M_{\rm NS} = 1.2 - 1.9\ M_\odot$. The initial $P_{\rm orb}$ were mainly chosen in the range of 2 to 4 days and do not follow a uniform distribution. The reason for this is that we were interested in obtaining systems with certain properties which turned out to be located around a specific initial $P_{\rm orb}$ which is characteristic for every studied configuration. To obtain this value we used a bracketing method which resulted in a high density of models around that specific initial $P_{\rm orb}$. The magnetic braking index γ was varied between 2 and 5 (but is constant for any given LMXB calculation). As mentioned in Section 2.3.2, in most cases we used a NS accretion efficiency parameter of $\epsilon = 0.3$. However, for 1.5 $M_\odot$ donors we also studied the influence of applying different values in the range $\epsilon = 0.1 - 0.9$. Although this entire parameter space of variables is large, the resulting systems do show similarities in the evolution as discussed below.

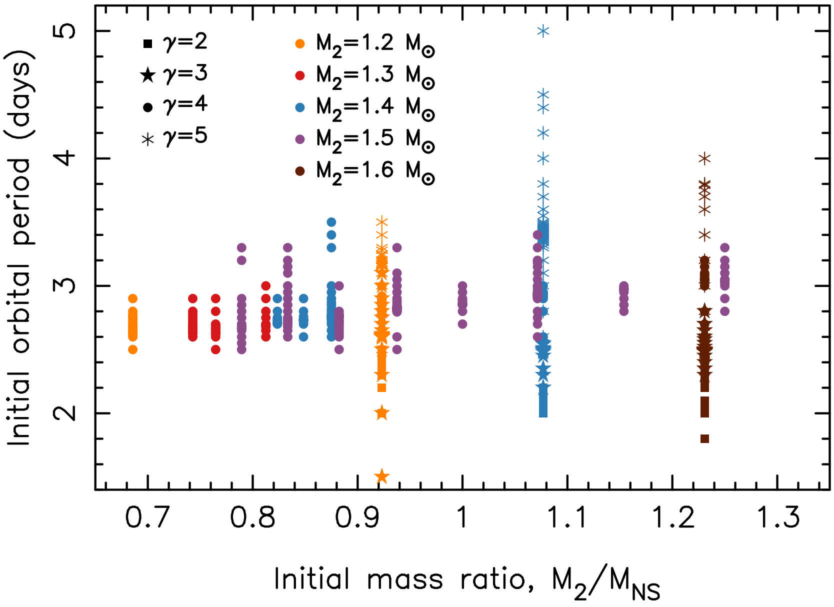

Figure 2.1: Grid of initial parameters for the studied LMXB configurations, yielding a total of more than 400 models. The colours correspond to different donor star masses (M_2), and the various symbols indicate different values of the magnetic braking index, γ. See text for further details.

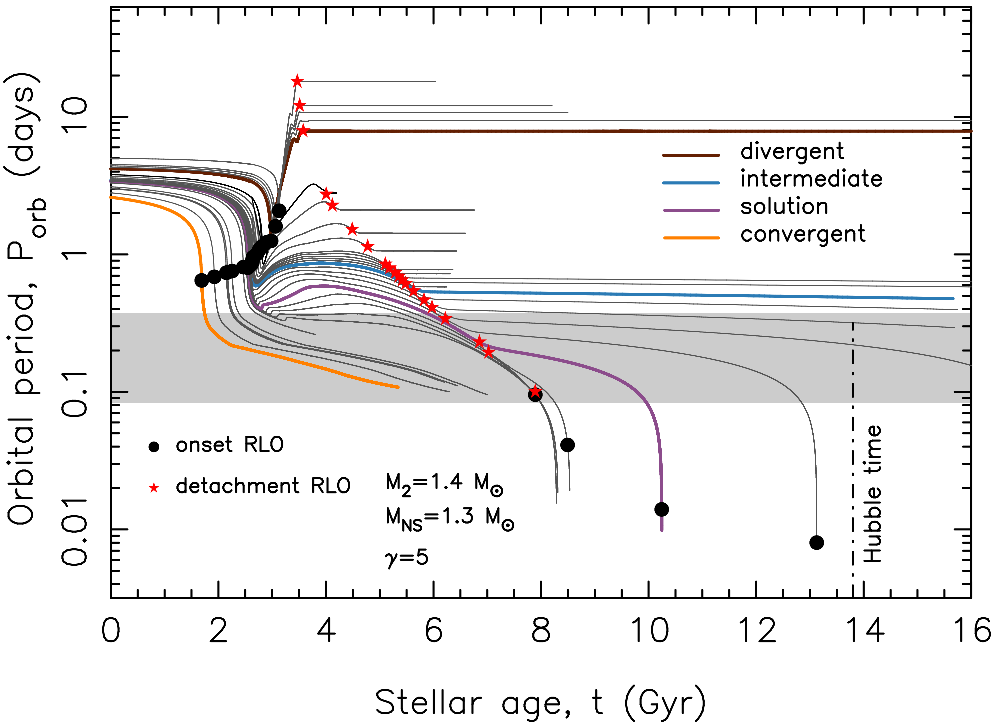

Figure 2.2: Orbital period evolution for LMXB systems with a donor mass of 1.4 $M_{\odot}$, a NS mass of 1.3 $M_{\odot}$ and a magnetic braking index of $\gamma = 5$. The black circles represent the onset of RLO and the red stars show the end of the mass-transfer phase. The observed MSP systems mainly investigated here, with low-mass He WD companions and $P_{\mathrm{orb}} = 2 - 9$ hr (cf. Table 2.1), are located within the grey shaded region. The LMXB systems experience a second RLO and evolve into ultra-compact X-ray binaries in very tight orbits.

2.4.2 Orbital evolution, mass transfer and stellar structure

The final P_{orb} of a given LMXB is a result of the interplay between mass transfer, magnetic braking and gravitational wave radiation. It strongly depends on the initial P_{orb} which determines the strength of orbital angular momentum losses and at which point in the nuclear evolution the donor star initiates RLO.

Pylyser & Savonije (1988) classified the orbital evolution of an LMXB system with respect to the final P_{orb} as: (i) converging, if $P_{\mathrm{orb}}^{\mathrm{final}} < P_{\mathrm{orb}}^{\mathrm{initial}}$, or (ii) diverging, if $P_{\mathrm{orb}}^{\mathrm{final}} > P_{\mathrm{orb}}^{\mathrm{initial}}$. Here, we redefine converging systems as those tight binaries where the donor star never detaches to form a He WD. As mentioned previously, we are interested in finding those systems that have a final P_{orb} between 2 – 9 hr and which have terminated their mass-transfer phase yielding a (proto) He WD remnant with a mass < 0.20 M$_{\odot}$ (cf. Table 2.1). The systems that fulfil these conditions are hereafter called solutions. Finally, we define the intermediate systems as those systems which detach from RLO to form a He WD with 9 hr $< P_{\mathrm{orb}}^{\mathrm{final}} < P_{\mathrm{orb}}^{\mathrm{initial}}$.

Fig. 2.2 shows the variety in orbital period evolution for an initial configuration with $M_2 = 1.4\ M_{\odot}$ ($Z = 0.02$), $M_{\mathrm{NS}} = 1.3\ M_{\odot}$, $\gamma = 5$ and $P_{\mathrm{orb}} = 2.6 - 5.0$ days. Highlighted with different colours are one example for each of the aforementioned classes of the outcome of LMXB evolution: converging, solution, intermediate and diverging. For clarity, we have omitted the markings of the temporary detachment of the diverging systems caused by the encounter of a slight chemical discontinuity at the outer boundary of the hydrogen burning shell (Tauris & Savonije 1999; D'Antona et al. 2006). The converging systems never detach, but keep evolving towards the minimum orbital period, $P_{\mathrm{min}} \approx 10 - 85$ min (Paczynski & Sienkiewicz 1981; Rappaport et al. 1982; Fedorova & Ergma 1989; Ergma & Sarna 1996; Podsiadlowski et al. 2002; van der Sluys et al. 2005a). As a result of numerical issues the evolution of the converging systems was ended before reaching P_{min}. At this point they have masses $< 0.13\ M_{\odot}$ and yet a significant hydrogen content – even in their cores – and very small nuclear burning rates (cf. Figs. 2.4, 2.5, and 2.11). Hence, these systems will not detach and produce a He WD within several Hubble times (if ever).

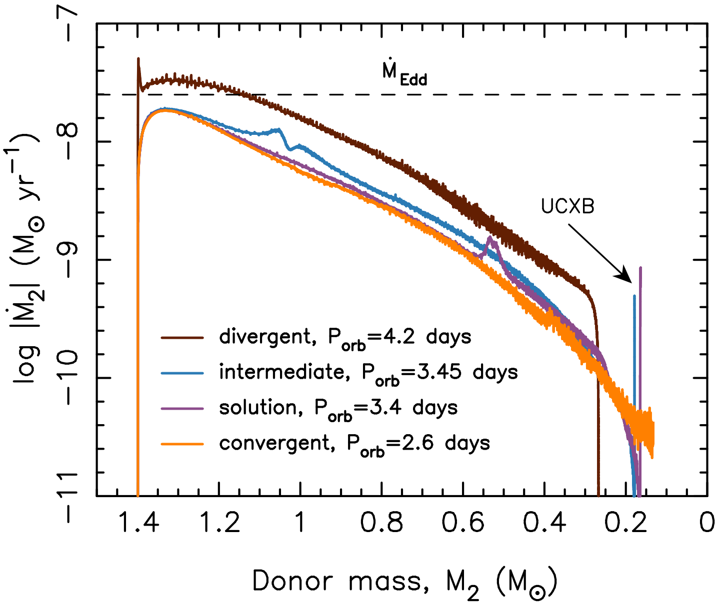

Figure 2.3: Mass-transfer rate versus decreasing donor star mass for the four systems highlighted in Fig. 2.2. The larger the initial P_{orb}, the higher the mass-transfer rate and the shorter the RLO episode will be. The converging system does not detach at all. The system resulting in a solution eventually evolves into an ultra-compact X-ray binary (UCXB) when the He WD fills its Roche lobe.

As demonstrated in the literature (Tutukov et al. 1987; Pylyser & Savonije 1988, 1989; Ergma & Sarna 1996; Podsiadlowski et al. 2002; van der Sluys et al. 2005a; Ma & Li 2009), an orbital bifurcation period (P_{bif}) exists which separates the evolution of converging[2] and diverging systems. With respect to the initial P_{orb} on the ZAMS we find $P_{\mathrm{bif}}^{\mathrm{ZAMS}} \simeq 4.0$ days. As a result of magnetic braking the orbit shrinks during the main-sequence evolution of the donor star prior to mass transfer. Thus the bifurcation period at the onset of RLO is $P_{\mathrm{bif}}^{\mathrm{RLO}} \simeq 1.2$ days (Fig. 2.2). If we apply other values of M_2, M_{NS}, γ or metallicity, the qualitative picture remains intact but the value of $P_{\mathrm{bif}}^{\mathrm{ZAMS}}$ changes between $\simeq 2.2 - 4.5$ days.

Fig. 2.3 shows the RLO mass-transfer rate, $|\dot{M}_2|$ as a function of decreasing donor mass, M_2 for the four examples highlighted in Fig. 2.2. At first sight these rates are quite similar. From a closer look, however, it is seen that the wider systems have higher values of $|\dot{M}_2|$ (and shorter durations of RLO), as expected from an evolutionary point of view (e.g. Tauris & Savonije 1999). And more importantly, the final fates of these four LMXB systems are quite different.

Changing the initial P_{orb} between 2.6 – 4.5 days means that the systems will gradually shift from undergoing Case A (onset of RLO on the main sequence) to early Case B RLO (onset of RLO in the Hertzsprung-gap), as shown in Fig. 2.4. The converging systems start RLO relatively early when there is

---

[2] Here meaning converging, solutions and intermediate systems.

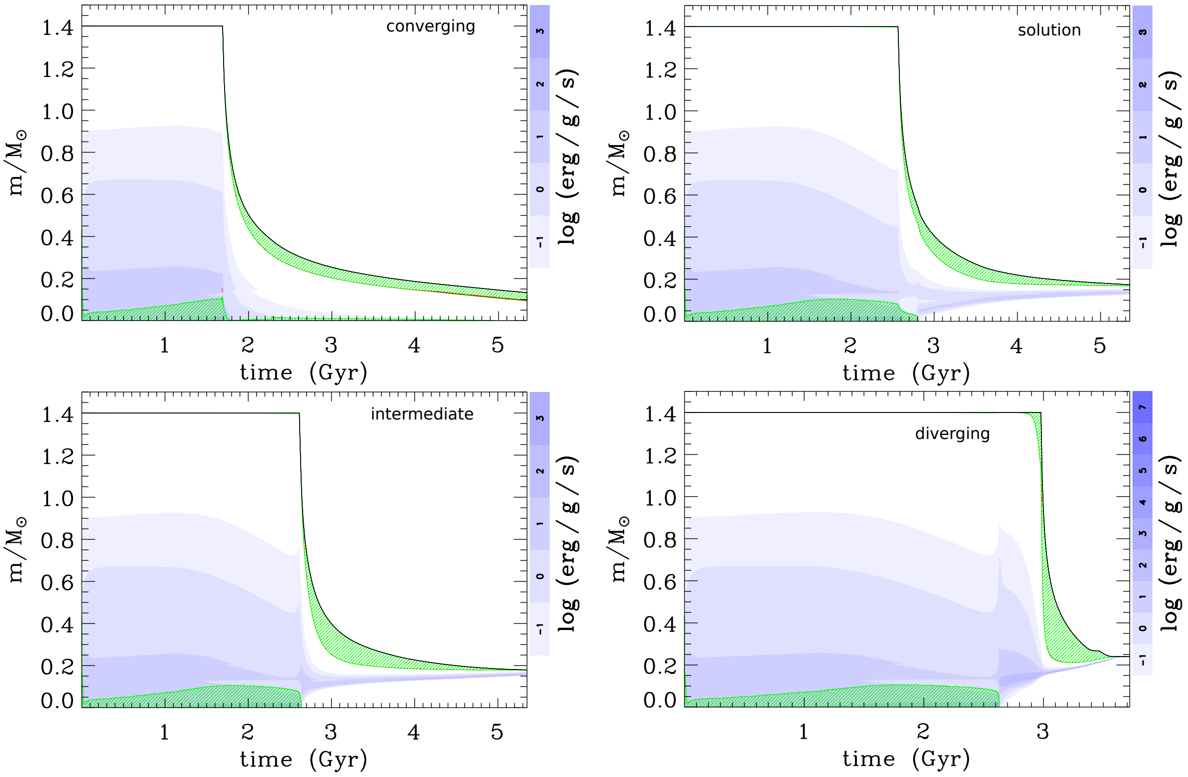

Figure 2.4: The Kippenhahn diagram of a converging (top left), solution (top right), intermediate (bottom left) and diverging (bottom right) LMXB system, respectively. In all cases we used $M_2 = 1.4\ M_\odot$, $M_{\rm NS} = 1.3\ M_{\rm NS}$, $\gamma = 5$ and applied initial $P_{\rm orb} = 2.6$, 3.4, 3.45 and 4.2 days, respectively. These four systems are identical to the examples highlighted in Fig. 2.2. In the converging system the donor star experiences Case A RLO; for the solution and intermediate systems the mass transfer is either late Case A or early Case B RLO, while the diverging systems undergo Case B RLO. The plots show cross-sections of the stars in mass-coordinates from the centre to the surface of the star, along the y-axis, as a function of stellar age on the x-axis. For clarity, we only show the evolution up to a stellar age of 5.35 Gyr in the first three panels. The duration of the LMXB-phase is: "∞" (no detachment), 4.0 Gyr, 2.9 Gyr and 0.6 Gyr, respectively. The green hatched areas denote zones with convection (according to the Schwarzschild criterion), initially in the core and later in the envelope of the donor stars. The intensity of the blue color indicates the net energy-production rate; the hydrogen burning shell is clearly seen in the case of the solution, intermediate and diverging systems at $m/M_\odot \simeq 0.2$.

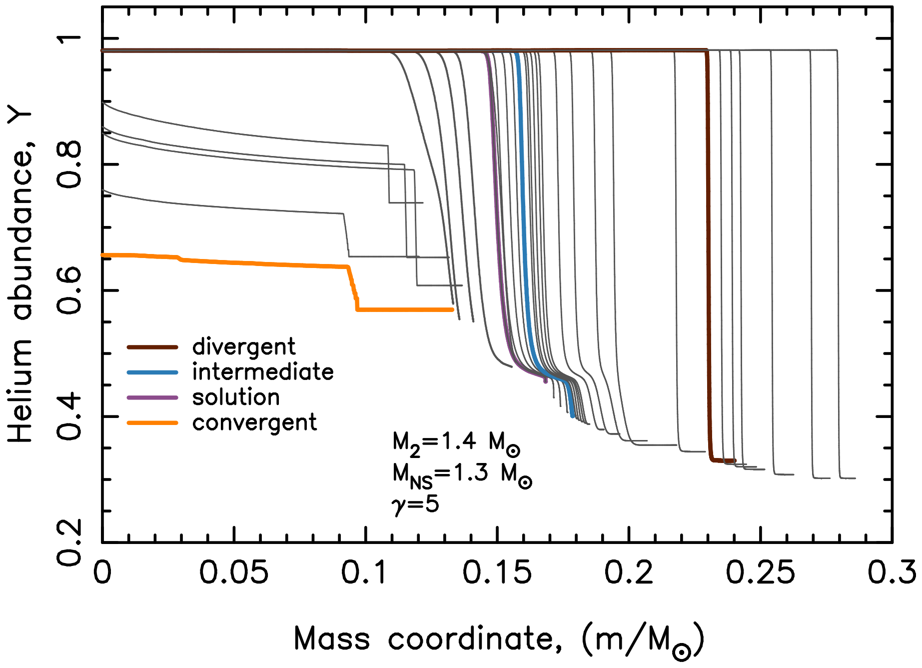

Figure 2.5: Helium abundance profiles of the donor stars in Fig. 2.2 at the time of RLO detachment (diverging, intermediate and solution) or at the end of our calculations (converging).

still a significant amount of hydrogen left in the core of the donor star. In these systems, the mass transfer is driven by a reduction in the orbital separation due to loss of orbital angular momentum (initially caused by magnetic braking, later dominated by gravitational wave radiation). The intermediate systems are in a transition between mass transfer driven by loss of orbital angular momentum and mass transfer driven by nuclear evolution and expansion of the donor star (the diverging systems).

The final helium abundance profiles of the donor stars are shown in Fig. 2.5. The thickness of the hydrogen-rich envelopes of these detached (proto) He WDs is very important for their subsequent thermal evolution (see Paper II).

In Fig. 2.6 we plot the final P_{orb} ("final" refers to our last calculated model) versus the initial P_{orb} for the same systems as in Fig. 2.2. The vertical dotted lines denote P_{detach}, P_{UCXB}, and P_{bif}. We define P_{detach} as the minimum initial P_{orb} leading to a detached He WD companion, and P_{UCXB} as the maximum initial P_{orb} leading to a system which becomes an ultra compact X-ray binary (UCXB) within a Hubble time (i.e. a detached system which, as a result of gravitational wave radiation, is driven into a very tight orbit with a second RLO from the He WD). All the systems on the left side of P_{detach} are on their way to P_{min}.

The orbital period fine-tuning problem

Fig. 2.6 illustrates two important characteristics of our close-orbit LMXB modelling: (i) how sensitive the outcome is to the initial P_{orb}; (ii) the systems we refer to as solutions are produced within a very narrow interval of initial $P_{\mathrm{orb}} = 3.39 - 3.43$ days which corresponds to onset of RLO near $P_{\mathrm{orb}} \approx 19.2 - 19.4$ hr. The solutions produced in this study all start inside (or slightly beyond) the narrow interval of initial P_{orb} between P_{detach} and P_{UCXB}. Those solutions with initial $P_{\mathrm{orb}} > P_{\mathrm{UCXB}}$ are the

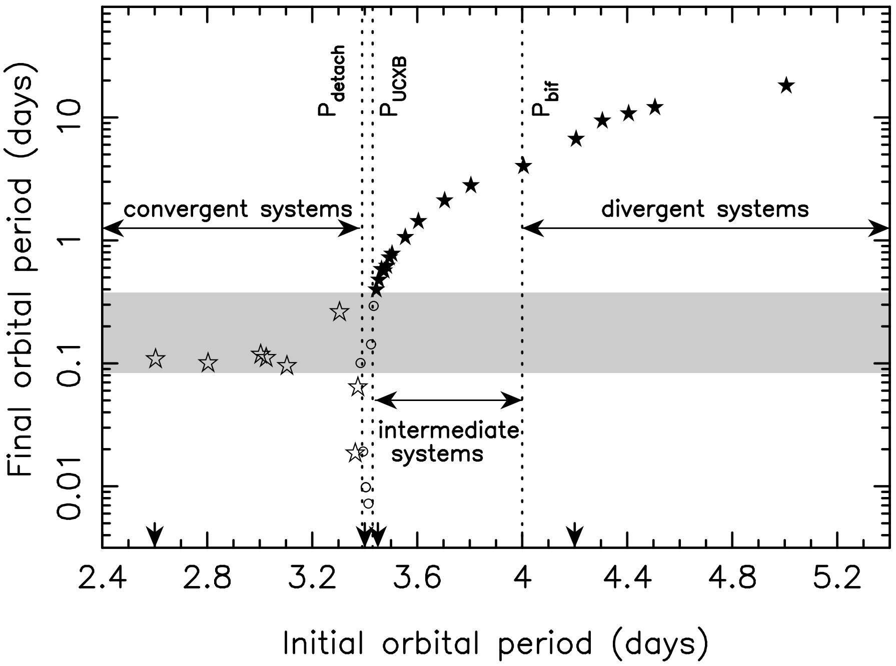

Figure 2.6: Final P_{orb} versus initial P_{orb} for all binaries investigated with $M_2 = 1.4\ M_\odot$, $M_{\mathrm{NS}} = 1.3\ M_\odot$ and a magnetic braking index of $\gamma = 5$ (cf. Fig. 2.2). The arrows at the bottom indicate the initial P_{orb} of the four highlighted systems. Circles represent solutions, i.e. systems which detached while situated inside the grey shaded region that marks the location of the observed MSP systems with $P_{\mathrm{orb}} = 2-9$ hr. The values of initial P_{orb} for these systems are confined to an extremely narrow interval (the orbital period fine-tuning problem, cf. Section 2.4.2). Open stars represent converging systems (which do not detach) and for which we ended our evolutionary calculations before reaching P_{min}. The vertical dotted lines denote P_{detach}, P_{UCXB}, and P_{bif}, see text.

systems which, after detachment, do not evolve into UCXBs within a Hubble time. The width of the initial (ZAMS) range of P_{orb} which allows for a solution is thus only $\sim 1\%$ in P_{orb}.

This is a puzzling result given that a fair fraction of observed MSPs are found with He WDs and $P_{\mathrm{orb}} = 2-9$ hr. We shall refer to this problem as the orbital period fine-tuning problem of LMXBs and discuss it further below, as well as in Section 2.5.2. Outside this narrow range in initial P_{orb}, the LMXB systems always evolve to become converging, intermediate or diverging systems.

In Fig. 2.7 we show the observed orbital period distribution of recycled pulsars with He WD companions (i.e. post-LMXB systems) in the Galactic field. Out of 35 systems with $P_{\mathrm{orb}} < 10$ days, 4 systems have $P_{\mathrm{orb}} < 9$ hr. Assuming these 4 systems (resembling the solutions from our modelling) are indeed produced from LMXBs with an initial P_{orb} between $3.39-3.43$ days (i.e. corresponding to the lower $\sim$4% of the full interval of initial P_{orb}, roughly between $3.4-4.4$ days, which lead to formation of MSPs with He WDs and final $P_{\mathrm{orb}} < 10$ days, see Fig. 2.6), we can estimate the probability for this outcome being a chance coincidence. In that case, the other 31 systems are produced for initial $P_{\mathrm{orb}} = 3.43-4.4$ days ($\sim$96% of the interval of initial P_{orb} producing MSPs with final $P_{\mathrm{orb}} < 10$ days). If the pre-LMXB distribution of P_{orb}, following the SN explosion that created the NS, is approximately flat between $\sim 3.4-4.4$ days, then the probability for producing at least 4 out of 35 MSPs with $P_{\mathrm{orb}} < 9$ hr is about 1:20, i.e. corresponding to not being a chance coincidence at the 95% confidence level.

We calculated this probability analytically using the binomial cumulative distribution function.

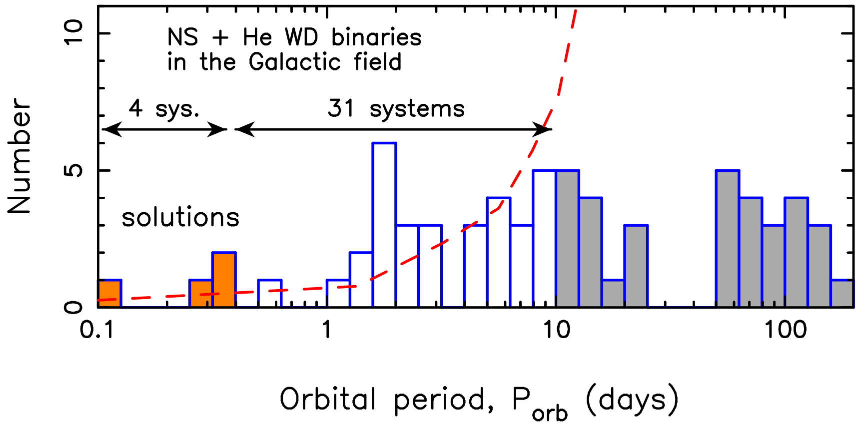

Figure 2.7: Distribution of orbital periods for all observed recycled pulsars (MSPs) with He WD companions in the Galactic field. In total there are 35 systems with $P_{\rm orb} < 10$ days; four of these are the solutions ($P_{\rm orb} < 9$ hr) marked with orange. Data from the ATNF Pulsar Catalogue Manchester et al. (2005) – version 1.50, July 2014. The red dashed line shows the distribution of systems that would be expected from our calculations using standard input physics (i.e. using the results presented in Fig. 2.6), thus illustrating the orbital period fine-tuning problem.

Actually, the problem is even worse given that a certain fraction of the systems formed with $P_{\rm orb} \simeq 2-9$ hr will merge because of gravitational wave radiation and thus not be observable for as long time as the MSPs with larger $P_{\rm orb}$. (The expected radio lifetimes of MSPs are many Gyr and are independent of $P_{\rm orb}$.) Hence, more than 4 systems are most likely to have formed as solutions for every 31 systems produced with $P_{\rm orb}$ between 9 hr and 10 days. As an example, PSR J0348+0432 ($P_{\rm orb} = 2.46$ hr, cf. Table 2.1) has a merger timescale of only ~400 Myr (Antoniadis et al. 2013). Additionally, there are observational selection effects against finding accelerated pulsed signals in very close binaries (Johnston & Kulkarni 1991), although modern day acceleration search software and increased computer power have somewhat alleviated this problem.

The discrepancy between observational data and our calculations is further illustrated by the red dashed line in Fig. 2.7 which shows the rough distribution of systems expected from modelling with standard input physics (assuming again a flat distribution of initial $P_{\rm orb}$ between ~3.4 – 4.4 days.)

The statistics depends, of course, on how the exact subsamples are chosen. However, the above example was calculated for the most conservative case using the result of calculated models with $\gamma = 5$ ($M_2 = 1.4\ M_\odot$). As we demonstrate below, the required fine-tuning is much worse (> 99.99% C.L.) for smaller values of γ. Therefore, there is no doubt that this severe fine-tuning has its basis in the input physics currently adopted in standard LMXB modelling. Something seems to be missing or must be modified – some mechanism that funnels more LMXBs to end up as MSPs with detached He WDs and $P_{\rm orb} < 9$ hr.

2.4.3 Magnetic braking and the influence of the γ-index

As discussed previously, the magnetic braking law is not well known. For this reason we investigated how the general behaviour of LMXBs in close orbits changes with different values of γ. In Fig. 2.8 is shown the difference in orbital period evolution for an initial LMXB with $M_2 = 1.4\ M_\odot$, $M_{\rm NS} = 1.3\ M_\odot$ and $P_{\rm orb} = 2.8$ days, for four different values of γ: 2, 3, 4 and 5. One can see that the higher the γ-index, the stronger is the loss of orbital angular momentum due to magnetic braking. This situation is reversed

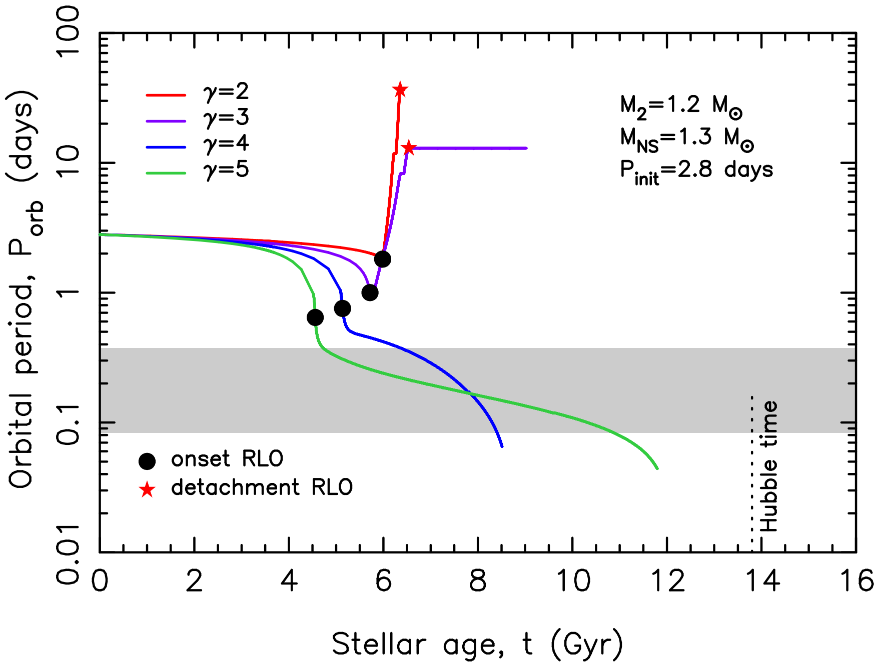

Figure 2.8: Influence of the magnetic braking index, γ on the orbital evolution of an LMXB system with M_2 = 1.2 $M_\odot$, $M_{\rm NS}$ = 1.3 $M_\odot$ and initial $P_{\rm orb}$ = 2.8 days. Plotted is $P_{\rm orb}$ as a function of age of the donor star. None of these models produce a solution (i.e. detachment within the grey shaded region). Instead the outcome is two diverging and two converging systems.

once the donor radius decreases below 1 $R_\odot$ (cf. Eq. 2.5). However, at that point the orbital evolution is mainly dominated by mass loss.

The main consequence of varying the γ-index is that $P_{\rm detach}$, $P_{\rm UCXB}$ and $P_{\rm bif}$ have smaller values for smaller γ, but the general orbital behaviour is similar. However, the final fate of the LMXBs is seen to be quite a sensitive function of γ, and the orbital period fine-tuning problem gets worse for $\gamma < 5$. For example, in Fig. 2.9 we demonstrate that for $\gamma = 2$ the resulting width of the interval of initial $P_{\rm orb}$ leading to an observed solution is less than 2 min (< 0.05% in $P_{\rm orb}$). This translates the significance of the orbital period fine-tuning problem to > 99.99% C.L. In Fig. 2.10 we have demonstrated how the orbital period fine-tuning problem systematically exacerbates with lower values of γ.

In the literature, some authors (e.g. Podsiadlowski et al. 2002; van der Sluys et al. 2005a) reduced the magnetic braking by an ad-hoc factor related to the size of the convective envelope, or turned it off when the donor became fully convective. We note here that with our code we did not produce any donors that became fully convective. In Section 2.5.1 we discuss the magnetic braking law and compare our results with previous work in the literature.

2.4.4 Evolution in the HR-diagram and hydrogen shell flashes

Fig. 2.11 shows the evolution in the Hertzsprung-Russell diagram of the donor stars for all the systems in Fig. 2.2. The systems that start mass transfer during hydrogen core burning (converging Case A RLO systems) closely follow an evolution studied in detail by Pylyser & Savonije (1989). These stars evolve along an almost straight line (following the ZAMS, with smaller radii as they lose mass) down towards very low temperatures and very low luminosities, until the donor star almost becomes fully convective

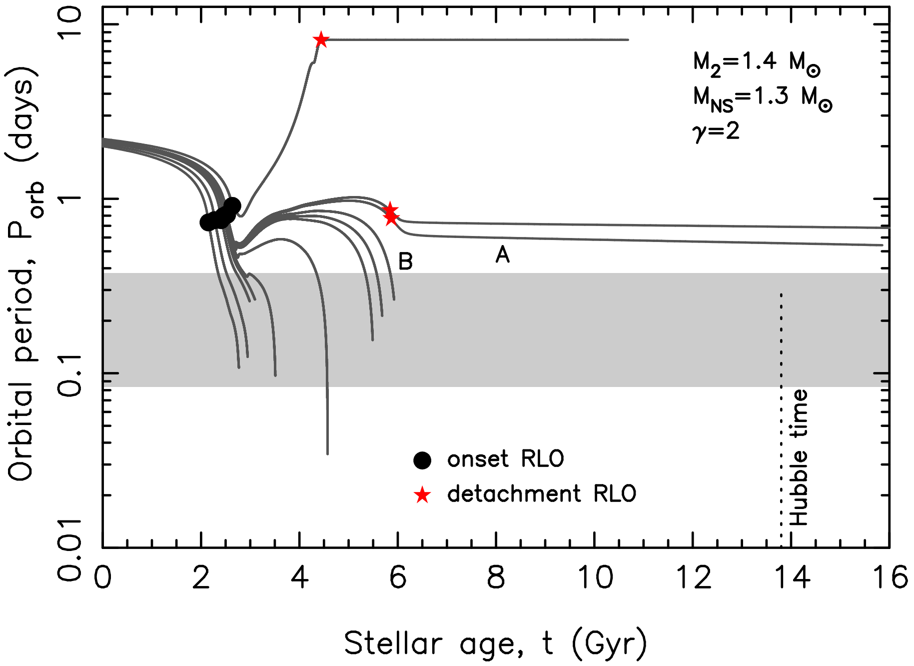

Figure 2.9: Orbital period evolution for all LMXB systems investigated with $M_2 = 1.4\ M_\odot$, $M_{NS} = 1.3\ M_\odot$ and a magnetic braking index of $\gamma = 2$. The first detached system (A) has an initial $P_{orb} = 2.148$ days while the widest of the converging systems investigated (B) has an initial $P_{orb} = 2.147$ days. Whereas system A leads to an intermediate system (with a final $P_{orb} > 9$ hr), system B does not detach but keeps evolving towards P_{min}. Therefore, the observed solutions (i.e. RLO detachment and formation of an MSP and a He WD with $P_{orb} = 2-9$ hr) would require a fine-tuning of the initial P_{orb} to be in a narrow range of less than 2 min. For larger values of γ the situation is less severe (Fig. 2.2) but still a serious problem, see Sections 2.4.2, 2.4.3 and 2.5.2.

and approaches the Hayashi-track. Subsequently, the luminosity is seen to decrease relatively rapidly because of fading nuclear burning and increasing degeneracy. The systems that fill their Roche lobe close to the core contraction phase or later, such as the solutions, the intermediate and the diverging systems, first evolve towards low effective temperatures and low luminosities until, because of ignition of hydrogen shell burning, they turn towards higher temperatures and – for the diverging systems with (sub)giant donors – higher luminosities. The more evolved the donor star is towards the red-giant branch (RGB) when it initiates mass transfer (i.e. the more massive its core mass), the higher the luminosity will be when the star finally evolves towards the WD cooling track.

To get a better overview of the correspondence between the evolutionary status of the donor star at the onset of RLO and the final fate of the LMXB, we show in Fig. 2.12 a zoom-in along the evolutionary track in the HR-diagram of a 1.4 $M_\odot$ star, from the ZAMS to the point where mass transfer is initiated to a 1.3 $M_\odot$ NS companion with various values of initial P_{orb}. The marked points indicate a sequence of cases where the evolutionary status of the donor star at the onset of RLO is somewhere between the middle of the main sequence (A) and all the way up to the point (F) where the donor star has ascended on the RGB. The systems leading to solutions initiate mass transfer in a very narrow epoch between points B and C, when the donor star leaves the main sequence and starts the contraction phase. The converging systems initiate mass transfer between points A and B, while the intermediate and diverging systems start mass transfer after points C and D, respectively.

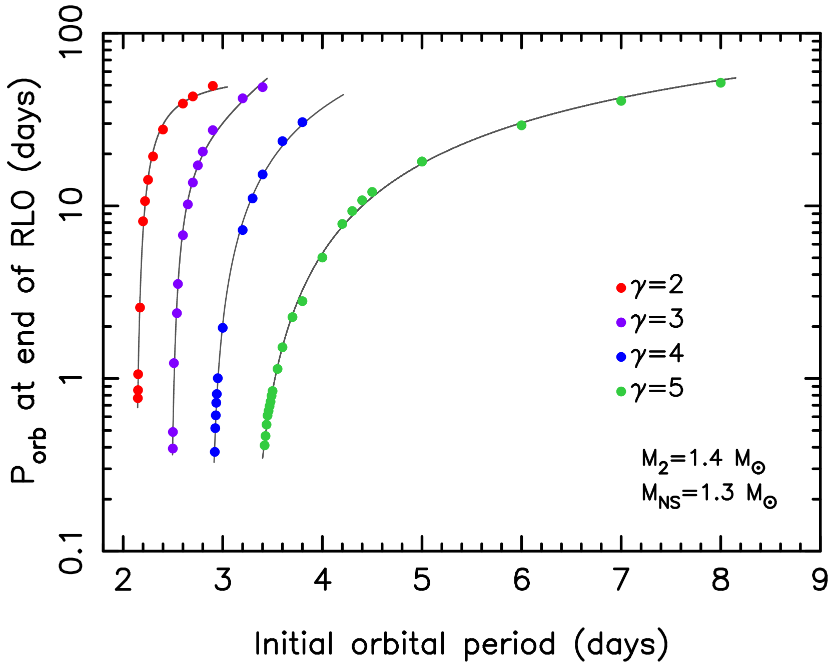

Figure 2.10: The calculated $P_{\rm orb}$ at Roche-lobe detachment as a function of initial $P_{\rm orb}$, plotted for different values of the magnetic braking index, γ. It is seen how the orbital period fine-tuning problem becomes worse for smaller values of γ, see text for discussions.

One can see from Fig. 2.11 that there is a region in which the donor stars experience one or several hydrogen shell flashes. The intensity of the flashes is gradually increasing with the initial $P_{\rm orb}$. In the literature, the mass interval in which a proto-WD experiences hydrogen flashes is roughly between $0.2-0.4\ M_{\odot}$ (Driebe et al. 1998; Sarna et al. 2000; Althaus et al. 2001c; Serenelli et al. 2002a; Nelson et al. 2004; Panei et al. 2007; Althaus et al. 2013), depending on metallicity and input physics (primarily in treatment of diffusion). Donor stars which initiate RLO in the interval between points E and F in Fig. 2.12 will experience hydrogen shell flashes after the mass-transfer phase. Some of these flashes may cause additional RLO of small amounts of material ($\sim 5\times 10^{-4}\ M_{\odot}$). A more complete discussion on the observed flashes in our models, and thermal evolution of (proto) WDs in particular, can be found in Paper II.

2.4.5 The ($M_{\rm WD}$, $P_{\rm orb}$)–relation for tight orbits

For low-mass stars ($< 2.3\,M_{\odot}$) on the RGB, there is a well-known relationship between the mass of the degenerate helium core and the radius of the giant star – almost entirely independent of the mass present in the hydrogen-rich envelope (Refsdal & Weigert 1971; Webbink et al. 1983). This relationship is very important for the formation of binary MSPs because it results in a unique relation between their orbital period ($P_{\rm orb}$) and WD mass ($M_{\rm WD}$) following the LMXB mass-transfer phase (Savonije 1987; Joss et al. 1987; Rappaport et al. 1995; Tauris & Savonije 1999; Nelson et al. 2004; De Vito & Benvenuto 2010; Shao & Li 2012). The masses of the He WD companions are expected to be between $0.13 < M_{\rm WD}/M_{\odot} < 0.46$. The predicted correlation between $M_{\rm WD}$ and $P_{\rm orb}$ has previously been somewhat difficult to verify observationally since few MSPs had accurately measured masses of their companion star. However, over the past decade the correlation has been confirmed from mass

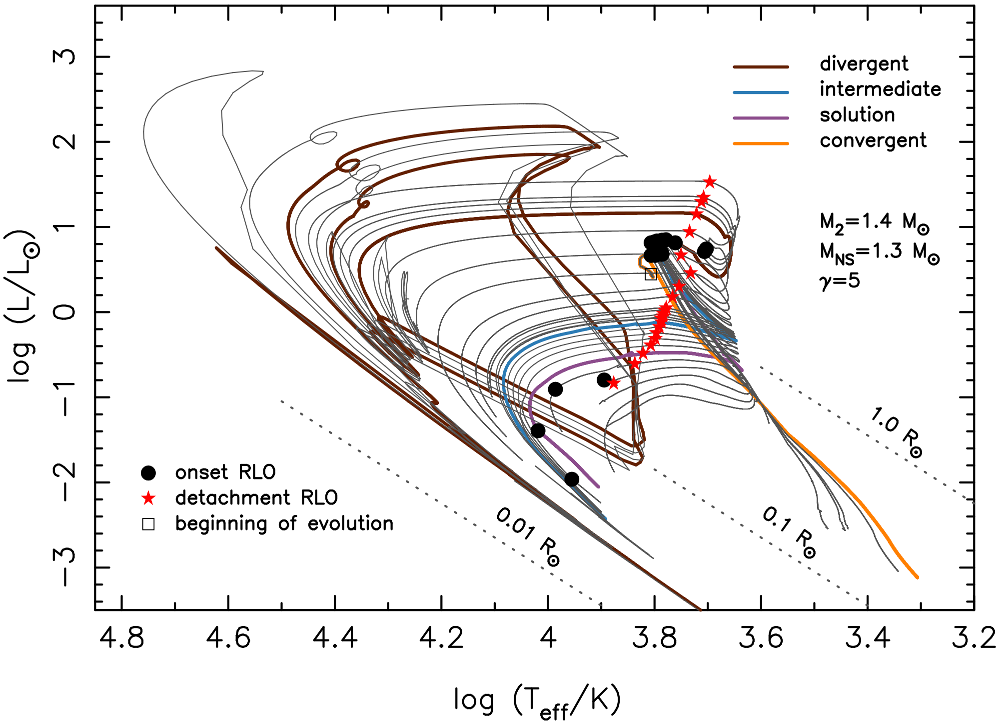

Figure 2.11: Evolutionary tracks in the HR-diagram for the systems shown in Fig. 2.2. The small square on the ZAMS near $(\log T_{\rm eff},\ \log(L/L_\odot)) = (3.8,\ 0.5)$ marks the beginning of the evolution for all systems.

measurements obtained from e.g. pulsar timing (Shapiro delay) or optical observations of He WD companions (e.g. van Kerkwijk et al. 2005), see Tauris & van den Heuvel (2014) for a recent comparison of theory and data.

As a consequence of loss of orbital angular momentum due to magnetic braking, LMXB systems with initial $P_{\rm orb} \lesssim P_{\rm bif}$ are expected to end up as close-binary MSPs with $P_{\rm orb}$ as short as a few hours (Section 2.3.1). Therefore, because of the still unknown strength of magnetic braking, the $(M_{\rm WD},\ P_{\rm orb})$–relation has always been considered less trustworthy for binary pulsars with $P_{\rm orb} \lesssim 2$ day (where He WDs have masses $< 0.20\ M_\odot$).

In Fig. 2.13 we have plotted the final $P_{\rm orb}$ versus $M_{\rm WD}$ for all our detached systems. For comparison we have plotted the theoretical $(M_{\rm WD},\ P_{\rm orb})$–relation following Tauris & Savonije (1999), hereafter TS99. Whereas this relation is expected out to $P_{\rm orb} \simeq 1000$ days for He WDs (at which point the core mass exceeds $\sim 0.46\ M_\odot$ and He is ignited, leading to a continuation of the correlation for higher mass CO WDs produced in LMXBs), Fig. 2.13 only shows the lower left part of the full diagram. The analytical expression of TS99 was derived for $P_{\rm orb} \gtrsim 1$ day. However, as noted, for example, by van Kerkwijk et al. (2005), Bassa et al. (2006a), Antoniadis et al. (2012) and Corongiu et al. (2012), even for $P_{\rm orb} < 1$ day there is apparently a fairly good agreement between the measured masses of He WDs and those expected from the theoretical $(M_{\rm WD},\ P_{\rm orb})$–relation. Examples of observational data include: PSR J1738+0333 (Antoniadis et al. 2012), PSR J1910-5959A (Corongiu et al. 2012), PSR J1012+5307 (Lazaridis et al. 2009), PSR J0348+0432 (Antoniadis et al. 2013), PSR J0751+1807 (Nice et al. 2008)[3];

---

[3] A more recent He WD mass constraint for PSR J0751+1807 is $M_{\rm WD} = 0.138 \pm 0.006\ M_\odot$ (95% confidence level, D. Nice, priv.comm.). This value is used in Fig. 2.13 and Table 2.1.

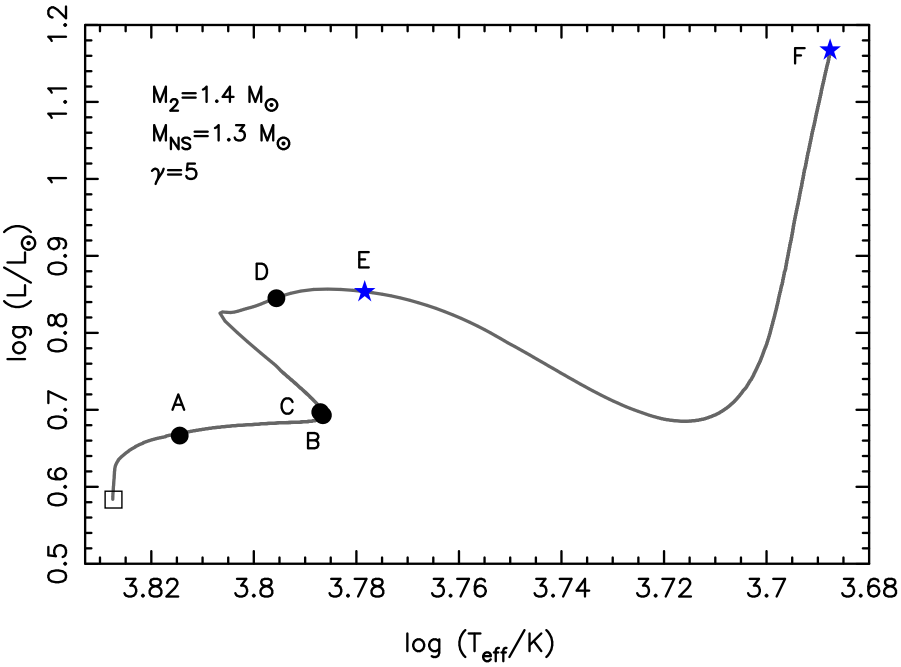

Figure 2.12: HR-diagram for the evolution of a 1.4 $M_\odot$ star ($Z = 0.02$). Along the evolutionary track (starting from the ZAMS marked by a square) is shown the points where such a donor star would initiate RLO to a 1.3 $M_\odot$ NS. The black circles represent the beginning of mass transfer for a system with initial $P_{\rm orb}$ of 2.6 (A), 3.38 (B), 3.42 (C), 3.6 (D), 4.0 (E) and 7.0 days (F), respectively. The interval between the points E and F denote an epoch where the donor star experiences hydrogen shell flashes after the end of the mass-transfer phase.

as well as low-mass He WD companions to non-degenerate stars (e.g. van Kerkwijk et al. 2010; Breton et al. 2012; Maxted et al. 2014a).

At first sight, PSR J0348+0432 may seem to be have an observed $P_{\rm orb}$ (2.46 hr) a bit below the expected theoretical value. However, one must keep in mind the effect of gravitational wave radiation following the detachment of the binary. Antoniadis et al. (2013) estimated a cooling age for this WD of about 2 Gyr, meaning that $P_{\rm orb} \simeq 5$ hr at the moment of Roche lobe detachment (a factor two larger than its present value). See also Fig. 2.2 for the effect of gravitational wave radiation from the detached binaries (solutions). In addition, low metallicity stars have smaller radii which leads to smaller values of final $P_{\rm orb}$ for the He WDs (see also Jia & Li 2014, for a recent investigation of this effect in close-orbit systems).

To summarize, for final $P_{\rm orb}$ less than a few days, our LMXB modelling demonstrates, as expected, a significant spread in the distribution of systems with respect to an extension of the relation of TS99. The deviations seem to be semi-systematic, in the sense that all models have smaller values of $M_{\rm WD}$ compared to the extrapolation of TS99, and there is a clear division of tracks depending on the original mass of the donor star, M_2. However, interestingly enough the order of these tracks does not follow a monotonic change in M_2. Nevertheless, the modelling of the correlation between $M_{\rm WD}$ and $P_{\rm orb}$ remains surprisingly robust for tight orbits, albeit with larger scatter. Given this large scatter (for example, we find that $P_{\rm orb}$ can vary by a factor of four for $M_{\rm WD} \simeq 0.16\ M_\odot$, cf. Fig. 2.13) it is somewhat meaningless to provide an exact analytical fit for $P_{\rm orb} < 2$ days. In this study, we only modelled systems with a metallicity $Z = 0.02$. Accounting for stars with other metallicities (e.g. TS99; Jia & Li 2014), we

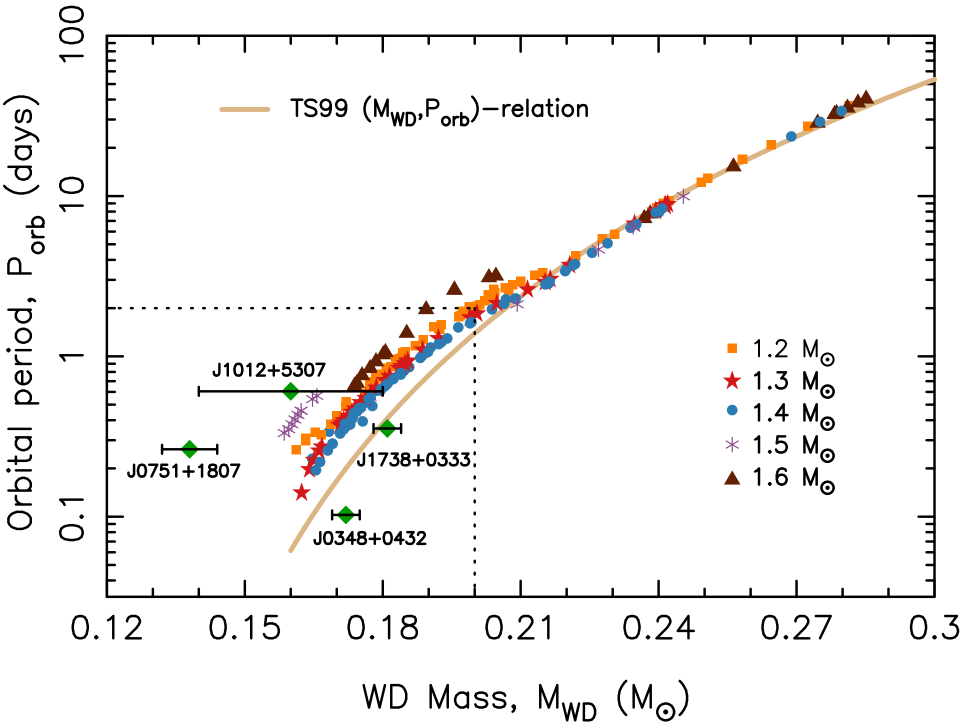

Figure 2.13: The (M_{WD}, P_{orb})–diagram for all the studied LMXB systems which produced a detached He WD. The initial parameters were chosen from: $M_2 = 1.2 - 1.6\ M_\odot$, $M_{\mathrm{NS}} = 1.3 - 1.9\ M_\odot$, $\gamma = 2 - 5$, and $\epsilon = 0.1 - 0.9$. The thick curve (TS99) represents the analytical expression given in Tauris & Savonije (1999) for $Z = 0.02$ (which was derived only for $P_{\mathrm{orb}} \gtrsim 1$ day, but here for illustration extended down to smaller values of P_{orb}). The green diamonds represent observed MSP systems with He WDs and $P_{\mathrm{orb}} < 15$ hr (i.e. similar to the solutions and partly the intermediate systems of our modelling). The region where the analytical expression is uncertain is for $P_{\mathrm{orb}} < 2$ days (and $M_{\mathrm{WD}} \lesssim 0.20\ M_\odot$). Although our calculations show a larger spread of the systems in this region the modelling of this correlation is still surprisingly robust – see text.

therefore expect a broader scatter of He WD masses between 0.14 – 0.20 $M_\odot$ for the systems with $P_{\mathrm{orb}} < 2$ days.

Minimum mass of a He WD

From theoretical work, it is expected that degenerate He WDs have masses of at least 0.13 $M_\odot$ (Schönberg & Chandrasekhar 1942; Tutukov et al. 1987). Indeed, we find that all our calculated He WDs have masses $M_{\mathrm{WD}} \geq 0.15\ M_\odot$. Donor stars in converging LMXBs with smaller semi-degenerate cores have relatively thick hydrogen-rich envelopes. Therefore these stars remain hydrogen rich and bloated which prevents them from terminating their mass-transfer process and forming a detached He WD. Such donors, which often suffer from ablation via the pulsar wind, can have their masses reduced significantly, leading to black-widow type eclipsing MSP systems which have typical companion masses of a few 0.01 $M_\odot$ (Roberts 2013; Chen et al. 2013), or even complete evaporation and formation of an isolated MSP; in some cases possibly surrounded by an asteroid belt (Shannon et al. 2013).

2.5 Discussion

2.5.1 The magnetic braking law

The loss of orbital angular momentum by magnetic braking is an uncertain aspect of LMXB evolution in close systems. For many years it has been thought that the magnetic field has to be anchored in underlying radiative layers of a star (Parker 1955). However, more recent observations and theoretical calculations question this hypothesis (e.g. Dorch & Nordlund 2001; Barnes 2003; Barnes & Kim 2010; Hussain 2011), and suggest that even fully convective stars may still operate a significant magnetic field – a conclusion which also has important consequences for the explanation of the observed period gap in CVs (Spruit & Ritter 1983; Knigge et al. 2011).

In addition, it is possible that the stellar activity necessary for magnetic braking to operate may saturate for rotation periods shorter than a few days (Rucinski 1983; Vilhu & Walter 1987). This would lead to a much flatter dependence of the angular momentum loss rate on the angular velocity ($\dot{J}_{\rm MB} \propto \Omega^{1.2}$) than is given by the Skumanich-law ($\dot{J}_{\rm MB} \propto \Omega^3$, Skumanich 1972) on which basis Eq. (2.5) is derived (see also Verbunt & Zwaan 1981). Based partly on observational work, Stepien (1995) derived a new magnetic braking law which smoothly matches the Skumanich-law for wide systems to the dependence obtained by Rucinski (1983) for short orbital period systems ($\lesssim$, 3 days):

$$\frac{\dot{J}_{\rm MB}}{J_{\rm orb}} \simeq -1.90 \times 10^{-16} \, \frac{k^2 R_2^2}{a^2} \frac{M^2}{M_1 M_2} \, e^{-1.50 \times 10^{-5}/\Omega} \qquad {\rm s}^{-1}. \tag{2.8}$$

Equation (2.5) and the formula above represent a strong and a weak magnetic braking torque, respectively, and their relative strength can be compared in e.g. Tauris (2001). For detailed investigations and reviews on the magnetic wind and the braking torque, see e.g. Eggleton (2001), van der Sluys et al. (2005b) and Knigge et al. (2011), and references therein. In our work presented here, we have restricted ourselves to allow for a variation in the magnetic braking strength by varying the γ-index in Eq. (2.5). This was partially motivated by the results of the work by van der Sluys et. al (see below) who applied Eq. (2.8) without success.

2.5.2 Further evidence of an orbital period fine-tuning problem

As demonstrated so far in this paper, we have a problem with modelling the formation of MSPs with He WDs in tight orbits. From a closer look in the literature it is evident that there is independent support for this conclusion, and our numerical studies are no exception from a more general picture.

van der Sluys et al. (2005a,b) investigated the evolution of LMXBs with the aim of producing UCXBs within a Hubble time. Using detailed modelling of LMXBs they concluded in their first paper that only a narrow range of initial $P_{\rm orb}$ and M_2 is able to result in parameters similar to those of observed UCXBs. To solve this problem, in their second paper, they applied reduced magnetic braking to their models following the work of Sills et al. (2000). The outcome was, however, that for less efficient magnetic braking it becomes impossible to evolve any systems to UCXBs.

In addition, we can compare our results with the detailed studies by Podsiadlowski et al. (2002) and Lin et al. (2011). In the work by Podsiadlowski et al. (2002), no solutions are found in their fig. 13. Only sequence d in their fig. 16 leads to a solution. In fig. 5 of Lin et al. (2011), one can see that only a few systems, out of $\sim 14\,000$ pulsar–WD binaries, are produced with a detached low-mass He WD orbiting a pulsar with $P_{\rm orb} < 15$ hr. The orbital period fine-tuning problem is also seen indirectly in fig. 6 (right panel) of Jia & Li (2014) where a small relative change in the initial $P_{\rm orb}$ results in a large relative change in the final $M_{\rm WD}$, i.e. $\Delta M_{\rm WD}/M_{\rm WD} > 30\, \Delta P_{\rm orb}/P_{\rm orb}$.

A related problem is the question of truncating the RLO. In their analysis of the formation of PSR J0348+0432, Antoniadis et al. (2013) concluded that its existence requires a finely tuned truncation of the mass-transfer process which is not yet understood. (This system is investigated in our Paper III.)

It seems clear that there is evidence of a general problem of reproducing tight-orbit pulsar binaries using current stellar evolution codes. The converging LMXBs most often do not detach but keep evolving with continuous mass transfer to more and more compact systems with $P_{\rm orb} \leq 2$ hr and ultra-light donor masses $M_2 < 0.08\,{\rm M}_\odot$. In the few instances where fine-tuning may lead to detachment at the right values of $P_{\rm orb}$ and M_2, the donor star is typically too hydrogen rich to settle and cool as a compact He WD. Instead the evolution may lead to formation of a redback-like system (Roberts 2013; Chen et al. 2013) which switches back and forth between being visible as an X-ray binary and an eclipsed radio MSP with a bloated companion (e.g. Archibald et al. 2009; Papitto et al. 2013; Bassa et al. 2014).

All of the above-mentioned modelling of LMXBs has difficulties producing detached He WDs with $P_{\rm orb} = 2 - 9$ hr (referred to in this paper as solutions). As demonstrated in Section 2.4.2, this is in clear contradiction with observations which show a relatively large population of such systems. Although we were able to produce solutions for all choices of $M_2 = 1.2 - 1.6\ M_\odot$ and values of $\gamma = 2 - 5$, it seems to require an unrealistic high degree of fine-tuning. Hence, we conclude that apparently something is missing in the standard input physics applied for LMXB modelling.

2.5.3 Irradiation effects, accretion disk instabilities and circumbinary disks

Several effects may potentially affect the LMXB evolution, such as irradiation of the donor star, accretion disk instabilities and a circumbinary disk. As discussed below, we have neglected these effects in our work presented here. Firstly, because in this study we want to isolate the investigation of magnetic braking. Secondly, it has been demonstrated that these effects are uncertain and difficult to quantify for trustworthy modelling. We now briefly discuss each of these effects.

During the LMXB evolution, a small part of mass lost from the companion may be injected into a circumbinary disk, which will exert tidal torques on the binary and extract angular momentum from the system (van den Heuvel 1994; Spruit & Taam 2001). In addition, feedback mechanisms caused by tides may transfer angular momentum from the disk back into the binary (Lin & Papaloizou 1979). Whether or not such a circumbinary disk may act as a reservoir of orbital angular momentum which potentially could stabilize and elucidate the orbital period fine-tuning problem remains to be investigated. It is possible that this loss of orbital angular momentum could lead to some of the intermediate systems in Fig. 2.2 to become solutions, rather than ending above the grey shaded region.

Another (uncertain) aspect of LMXB evolution is the effect of accretion disk instabilities (Pringle 1981; van Paradijs 1996; Lasota 2001; Dubus et al. 2001; Coriat et al. 2012). These are thermal-viscous instabilities resulting from a relatively large and sudden local increase in opacity and viscosity of the disk material at (critically) low mass-transfer rates. The high viscosity leads to a sudden outburst in which the NS accretes at a much higher rate. Outbursts are alternated by low-viscosity stages during which the disk builds up again. Stable behaviour can only persist if the entire disk has a homogeneous degree of ionization. In our work, we have partly compensated for this effect by choosing a small NS accretion efficiency (Section 2.3.2). It is possible, however, that during these outbursts (where $|\dot{M}_2| > \dot{M}_{\rm Edd}$) some material is fed into a circumbinary disk which may affect the orbital angular momentum of the system, as mentioned above.

There is, in addition, the effect of irradiation feedback on the long-term evolution of a close-orbit binary (e.g. Büning & Ritter 2004; Ritter 2008; Dubus et al. 1999). The impact and the modelling of this effect, leading to cyclic accretion, is still unclear and also not included in the present study. Recent work by Benvenuto et al. (2012) on the evolution of UCXBs suggests that the inclusion of irradiation feedback is not very significant for the secular evolution and thus the final properties of these systems. This is in agreement with Nelson & Rappaport (2003) who found that the effect of excess bloating due to X-ray irradiation is small (however, see also Podsiadlowski 1991). Irradiation effects by the pulsar wind (Tavani & Brookshaw 1992), however, possibly in combination with tidal dissipation of energy in the envelope, may cause a companion star to be thermally bloated. This may lead to evaporation and eclipses of the observed radio signals as seen in many narrow-orbit MSP systems. In the case of PSR J2051−0827 one can even measure the effects of gravitational quadrupole moment changes (Lazaridis et al. 2011), which affect the orbital evolution in a semi-cyclic and poorly understood manner that may also be applicable to close-orbit LMXBs (Applegate & Shaham 1994; Lanza & Rodonò 1999).

2.6 Conclusions

The main results are summarized as follows:

i) We have applied a detailed stellar evolution code to model the evolution of ~ 400 close binaries containing a NS and a low-mass main-sequence star. We evolved the systems to the LMXB phase with the purpose of reproducing the observed MSPs hosting He WD companions in tight orbits with $P_{\rm orb} \simeq 2-9$ hr. Using a standard prescription for orbital angular momentum losses via magnetic braking we can reproduce the observed systems for a large initial parameter space of donor star masses, NS masses, NS accretion efficiencies and magnetic braking index values.

ii) However, from an analysis of our modelling we find that a severe fine-tuning is required for the initial orbital period of the LMXBs in order to reproduce these observed systems. Based on a comparison to observational data of binary pulsars, we argue that such a fine-tuning is unlikely. We refer to this issue as the orbital period fine-tuning problem. We find further support for this problem from earlier independent studies in the literature. We conclude that something needs to be modified or is missing in the standard input physics of LMXB modelling.

iii) We have demonstrated that the ($M_{\rm WD}$, $P_{\rm orb}$)–relation is, in general, also valid for binary pulsars with He WDs having $P_{\rm orb} < 2$ days, although with an expected large scatter in He WD masses between $0.15-0.20\ M_\odot$. This conclusion is based on a combination of our theoretical modelling as well as recent observational data.

Acknowledgements AGI is grateful for fruitful discussions with: Fabian Schneider, Pablo Marchant, Luca Grassitelli, Debashis Sanyal, Jean-Claude Passy and Richard Stancliffe. We thank the referee, Zhanwen Han, for helpful comments and for suggesting Fig. 2.10.

CHAPTER 3

The timescale of low-mass proto-helium white dwarf evolution

Alina G. Istrate, Thomas M. Tauris, Norbert Langer and John Antoniadis

Astronomy & Astrophysics, 2014, 571, Letter L3

Abstract A large number of low-mass ($\lesssim 0.20\ M_\odot$) helium white dwarfs (He WDs) have recently been discovered. The majority of these are orbiting another WD or a millisecond pulsar (MSP) in a close binary system; a few examples are found to show pulsations or to have a main-sequence star companion. There appear to be discrepancies between the current theoretical modelling of such low-mass He WDs and a number of key observed cases, indicating that their formation scenario yet remains to be fully understood. Here we investigate the formation of detached proto-He WDs in close-orbit low-mass X-ray binaries (LMXBs). Our prime focus is to examine the thermal evolution and the contraction phase towards the WD cooling track and investigate how this evolution depends on the WD mass. Our calculations are then compared to the most recent observational data. Numerical calculations with a detailed stellar evolution code were used to trace the mass-transfer phase in a large number of close-orbit LMXBs with different initial values of donor star mass, neutron star mass, orbital period, and strength of magnetic braking. Subsequently, we followed the evolution of the detached low-mass proto-He WDs, including stages with residual shell hydrogen burning and vigorous flashes caused by unstable CNO burning. We find that the time between Roche-lobe detachment until the low-mass proto-He WD reaches the WD cooling track is typically $\Delta t_{\rm proto} = 0.5 - 2$ Gyr, depending systematically on the WD mass and therefore on its luminosity. The lowest WD mass for developing shell flashes is $\sim 0.21\ M_\odot$ for progenitor stars of mass $M_2 \leq 1.5\ M_\odot$ (and $\sim 0.18\ M_\odot$ for $M_2 = 1.6\ M_\odot$). The long timescale of low-mass proto-He WD evolution can explain a number of recent observations, including some MSP systems hosting He WD companions with very low surface gravities and high effective temperatures. We find no evidence for $\Delta t_{\rm proto}$ to depend on the occurrence of flashes and thus question the suggested dichotomy in thermal evolution of proto-WDs.

3.1 Introduction

In recent years, the number of detected low-mass ($\lesssim 0.20\ M_\odot$) helium white dwarfs (He WDs) has increased dramatically, mainly as a result of multiple survey campaigns such as WASP, ELM, HVS, *Kepler*, and SDSS (Pollacco et al. 2006; Rowe et al. 2010; Brown et al. 2005, 2010, 2013; Silvotti et al. 2012; Kilic et al. 2012; Hermes et al. 2013b; Maxted et al. 2014a).

The existence of low-mass He WDs in close binaries with a radio millisecond pulsar (MSP), however, has been known for a few decades (e.g. van Kerkwijk et al. 2005, and references therein). Several attempts have been made to calibrate WD cooling models for such systems on the basis of the spin-down properties of the MSP (e.g. Alberts et al. 1996; Hansen & Phinney 1998; Driebe et al. 1998; Althaus et al. 2001c; Panei et al. 2007). The idea is that the characteristic spin-down age of the MSP ($\tau_{\rm PSR} \equiv P/(2\dot{P})$, where P is the spin period and $\dot{P}$ is the period derivative) should be equivalent to the cooling age of the WD ($\tau_{\rm cool}$), assuming that the radio MSP is activated at the same time as the WD is formed, following an epoch of mass transfer in a low-mass X-ray binary (LMXB). Unfortunately, this method is highly problematic since $\tau_{\rm PSR}$ generally is a poor true age estimator. It can easily be incorrect by a factor of 10 or more (Camilo et al. 1994; Lorimer et al. 1995; Tauris 2012; Tauris et al. 2012). Determining the true age of MSPs, however, is important for studying their spin evolution and constraining the physics of their previous recycling phase (Lazarus et al. 2014).

The discovery of the intriguing PSR J1012+5307 (Nicastro et al. 1995) sparked an intense discussion about WD cooling ages and MSP birthrates (Lorimer et al. 1995) given that $\tau_{\rm PSR} > 20\ \tau_{\rm cool}$. Soon thereafter, it was suggested (Alberts et al. 1996; Driebe et al. 1998; van Kerkwijk et al. 2005) that He WDs with a mass $\lesssim 0.20\ M_\odot$ avoid hydrogen shell flashes, whereby their relatively thick ($\sim 10^{-2}\ M_\odot$) hydrogen envelope remains intact, causing residual hydrogen shell burning to continue on a very long timescale. Despite significant theoretical progress (e.g. Althaus et al. 2013, and references therein), our understanding of the thermal evolution of (proto) He WDs remains uncertain. In particular, a number of recent observations of apparently bloated WDs calls for an explanation.

In this Letter, we study the formation of a large number of low-mass He WDs by modelling close-orbit LMXBs. We carefully investigate the properties of the resulting proto-WDs and follow their evolution until and beyond settling on the WD cooling track. Finally, we compare our results with observations.

3.2 Numerical methods and physical assumptions

Numerical calculations with a detailed stellar evolution code were used to trace the mass-transfer phase following the same prescription as outlined in Istrate et al. (2014a). We investigated models with a metallicity of $Z = 0.02$, a mixing-length parameter $\alpha = l/H_p = 2.0$, and a core convective overshooting parameter of $\delta_{\rm OV} = 0.10$. A wide range of LMXB systems were investigated with different initial values of donor star mass (M_2), neutron star mass, orbital period, and the so-called γ-index of magnetic braking. The evolution of the low-mass (proto) He WD was calculated including chemical diffusion (mixing), hydrogen shell flashes (CNO burning), and residual shell hydrogen burning. Convective, semi-convective, and overshoot mixing processes were treated via diffusion. Thermohaline mixing was included as well, whereas gravitational settling and radiative levitation were neglected, as was stellar wind mass loss.

3.3 Results

In Fig. 3.1 we have plotted a selection of our calculated evolutionary tracks, from the moment of Roche-lobe detachment until the end of our calculations, for (proto) He WDs with masses of $0.15 - 0.28\ M_\odot$. In general, our models fit the observations quite well. The few cases with discrepancies are sources with large uncertainties in the WD mass. Vigorous single or multiple cycle hydrogen shell flashes explain the large loops in the diagram, whereas mild thermal instabilities are seen e.g. for the $0.25\ M_\odot$ proto-WDs at $\log g \simeq 4.5$. It has been known for many years that a thermal runaway flash may develop through unstable CNO burning when a proto-WD evolves towards the cooling track (Kippenhahn & Weigert 1967; Webbink 1975; Iben & Tutukov 1986). During these flashes the luminosity becomes very high, whereby the rate of hydrogen burning is significantly increased (e.g. Nelson et al. 2004; Gautschy 2013,

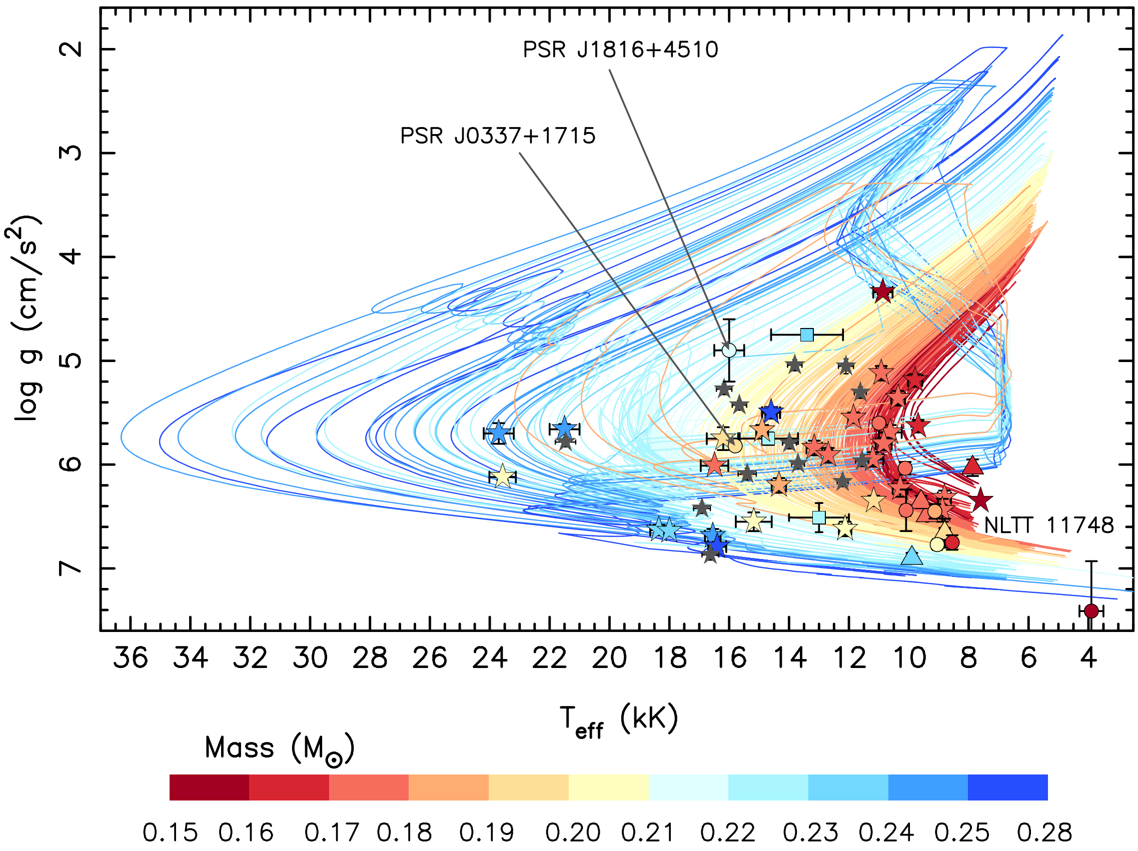

Figure 3.1: Evolutionary tracks in the ($T_{\rm eff}, \log\, g$)–diagram. The evolution from Roche-lobe detachment until settling on the WD cooling track and beyond is shown for a selection of our models. The colour scale represents the final WD mass. A few cases of vigorous hydrogen shell flashes explain the large (counterclockwise) loops in the diagram. Observed WDs are shown with symbols (stars: sdB+WD, double WDs [grey stars: WDs with poor mass constraints]; triangles: pulsating WDs; squares: WD+MS; circles: WD+MSP – see Appendix A for references and data).

and references therein). Our models with strong flashes often experience an additional episode of mass loss via Roche-lobe overflow (RLO, see also Iben & Tutukov 1986; Sarna et al. 2000; Podsiadlowski et al. 2002; Nelson et al. 2004).

For progenitor stars with $M_2 \leq 1.5\ M_\odot$ we find hydrogen shell flashes in WDs with masses of $0.21 \leq M_{\rm WD}/M_\odot \leq 0.28$. Hence, the lowest mass for which flashes occur is $M_{\rm flash} = 0.21\ M_\odot$. However, we find a lower value of $M_{\rm flash} = 0.18\ M_\odot$ for $M_2 = 1.6\ M_\odot$. It has been argued (e.g. van Kerkwijk et al. 2005) that the value of $M_{\rm flash}$ is important since it marks a dichotomy for the subsequent WD cooling such that WDs with a mass $M_{\rm WD} < M_{\rm flash}$ remain hot on a Gyr timescale as a result of continued residual hydrogen shell burning, whereas WDs with $M_{\rm WD} > M_{\rm flash}$ cool relatively fast as a result of the shell flashes that erode the hydrogen envelope. We find that this transition is smooth, however, and that the thermal evolution timescale mainly depends on the proto-He WD luminosity and not on the occurrence or absence of flashes.

In Fig. 3.2 we have plotted the time, $\Delta t_{\rm proto}$ it takes from Roche-lobe detachment until the star reaches its highest value of $T_{\rm eff}$. (For WDs that undergo hydrogen shell flashes we used the time until the occurrence of highest $T_{\rm eff}$ on their last loop in the HR–diagram.) The plot shows a very strong dependence on $M_{\rm WD}$. For very low-mass He WDs (i.e. those with $M_{\rm WD} < M_{\rm flash}$, which therefore avoid hydrogen shell flashes), $\Delta t_{\rm proto}$ may last up to 2 Gyr. This result has important consequences for their thermal evolution and contraction (see below). There is a well-known correlation between the degenerate core mass of an evolved low-mass star and its luminosity, L (Refsdal & Weigert 1971). After terminating the RLO, the star moves to the far left in the HR–diagram – (initially) roughly at constant L – while burning the residual hydrogen in the envelope at a rate proportional to L. We find that the total amount of hydrogen left in the envelope is always $\sim 0.01 \pm 0.005\ M_\odot$, in agreement with Sarna et al. (2000), and is correlated in a variable manner with $M_{\rm WD}$ (especially for $M_2 \geq 1.5\ M_\odot$, explaining the peak in Fig. 3.2). Therefore, the increase in $\Delta t_{\rm proto}$ seen in Fig. 3.2 for decreasing values of $M_{\rm WD}$ can simply be understood from their much lower luminosities following the Roche-lobe detachment (see also Figs. 5 and 10 in Istrate et al. 2014a). Based on our calculated proto-He WD models, we find (see Appendix B)

$$\Delta t_{\rm proto} \simeq 400\ \ {\rm Myr}\ \left(\frac{0.20\ M_\odot}{M_{\rm WD}}\right)^7 . \tag{3.1}$$

The conclusion that $\Delta t_{\rm proto}$ can reach $\sim$ Gyr was found previously for a few single models (e.g. Driebe et al. 1998; Sarna et al. 2000; Althaus et al. 2001c). Here we show, for the first time, its systematic dependence on $M_{\rm WD}$.
Fig. 3.3 shows the contraction phase for three proto-He WDs. The value of $\Delta t_{\rm proto}$ increases significantly when $M_{\rm WD}$ decreases from 0.24 to 0.17 $M_\odot$. Hence, low-mass ($\lesssim 0.20\ M_\odot$) proto-He WDs can remain bloated on a very long timescale. It is important to notice that no pronounced discontinuity in $\Delta t_{\rm proto}$ is seen at $M_{\rm flash} \simeq 0.21\ M_\odot$ (cf. Figs. 3.2, 3.3, and A.2). Although the peak luminosity (and thus the rate of eroding hydrogen) is high during a flash, the star only spends a relatively short time ($\sim 10^3 - 10^6$ yr) at high L when making a loop in the HR–diagram.

3.4 Comparison with observational data of He WDs

In Table A.1 (Appendix A) we list observed low-mass He WDs included among the plotted data in Fig. 3.1. We now discuss recent interesting sources in view of our theoretical modelling.

3.4.1 MSPs with low-mass (proto) He WDs in tight orbits

The companion star to PSR J1816+4510 ($P_{\rm orb} = 8.7$ hr) was recently observed by Kaplan et al. (2012, 2013). They assembled optical spectroscopy and found an effective temperature of $T_{\rm eff} = 16\,000 \pm 500$ K, a surface gravity of $\log g = 4.9 \pm 0.3$, and a companion mass of $M_{\rm WD} \sin^3 i = 0.193 \pm 0.012\ M_\odot$, where i is the orbital inclination angle of the binary. They concluded that while the spectrum is rather similar to that of a low-mass He WD, it has a much lower surface gravity (i.e. larger radius) than a WD on the cooling track. They discussed that PSR J1816+4510 perhaps represents a redback system (cf. Chen et al. 2013, for a formation scenario) where pulsar irradiation of the hydrogen-rich, bloated companion causes evaporation of material, which can explain the observed eclipses of the radio pulses for ~10% of the orbit. However, the very hot surface temperature of this companion (16 000 K) cannot be explained from a redback scenario. Redbacks typically have illuminated dayside temperatures of only $T_{\rm eff} \simeq 6\,000$ K (Breton et al. 2013). Here we suggest that this companion star is simply a low-mass proto-He WD. As we have demonstrated, such a star takes several 100 Myr to reach the cooling track, and our models match the observed values of $T_{\rm eff}$ and $\log g$. (Note, for $P_{\rm orb} = 8.7$ hr one usually expects $M_{\rm WD} \lesssim 0.18\ M_\odot$, cf. Istrate et al. 2014a).

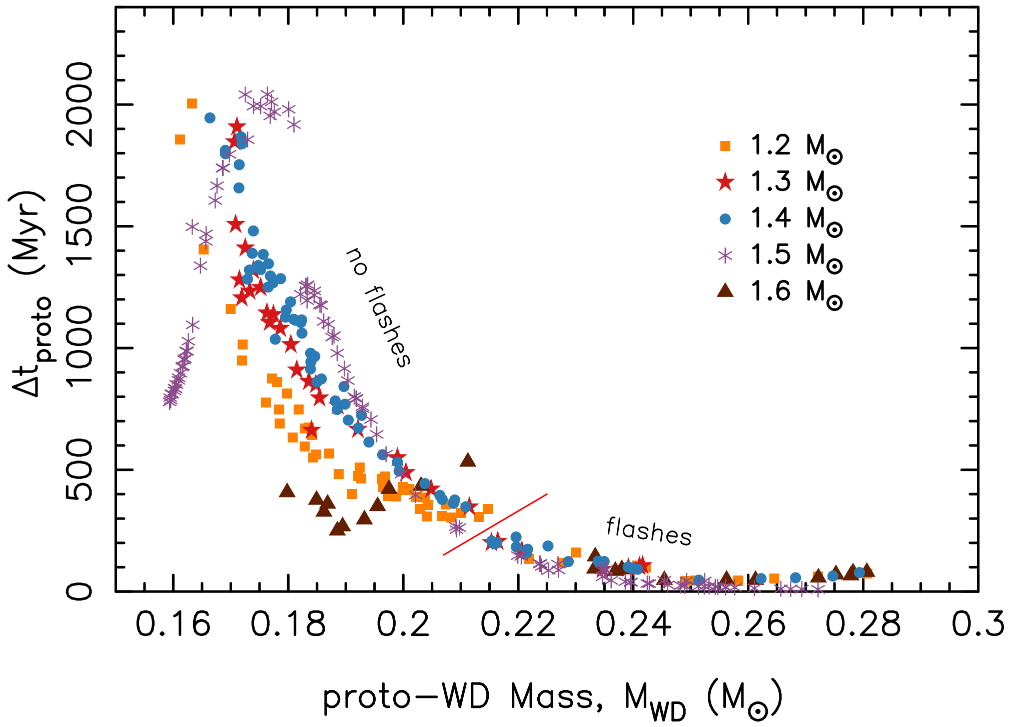

Figure 3.2: Contraction timescale, $\Delta t_{\mathrm{proto}}$ of evolution from Roche-lobe detachment until settling on the WD cooling track, plotted as a function of WD mass, M_{WD}. The initial ZAMS masses of the WD progenitors (the LMXB donor stars) are indicated with various symbols and colours. The red line marks $M_{\mathrm{flash}} \simeq 0.21\ M_{\odot}$ for progenitor stars $\lesssim 1.5\ M_{\odot}$.

Another case is the triple system PSR J0337+1715 recently discovered by Ransom et al. (2014a), which raises fundamental questions about its formation (Tauris & van den Heuvel 2014). One open question is the order of formation of the two WDs orbiting the MSP (with $P_{\mathrm{orb}} = 1.6$ and 327 days). Spectroscopy of the inner companion by Kaplan et al. (2014b) verified that this is a $0.197\ M_{\odot}$ He WD, as known from pulsar timing. They measured a low surface gravity of $\log g = 5.82 \pm 0.05$ and noted that its very high surface temperature, $T_{\mathrm{eff}} = 15,800 \pm 100$ K, could indicate that it had just experienced a flash. This would suggest a surprisingly short lifetime for this object. However, our modelling of $\sim 0.20\ M_{\odot}$ He WDs shows that these stars avoid flashes. Instead we find that for such a star it takes 400 – 600 Myr (Fig. 3.2) to reach the WD cooling track. Therefore, we conclude that it is reasonable to detect such a WD at an early, bloated stage of its evolution.

3.4.2 NLTT 11748 and other low-mass (proto) He WD binaries

A large number of low-mass proto-He WDs (also classified as sdB stars) are found in binaries with another WD. These systems probably formed via stable RLO in cataclysmic variable systems resembling our calculations, but with a $\sim 0.7\ M_{\odot}$ CO WD accretor instead of a NS. NLTT 11748 was discovered by Steinfadt et al. (2010b), with follow-up observations made by Kaplan et al. (2014a). This eclipsing detached binary consists of a $0.71 - 0.74\ M_{\odot}$ CO WD with a very low-mass He WD and $P_{\mathrm{orb}} \simeq 5.6$ hr. Our evolutionary tracks for a $0.16\ M_{\odot}$ He WD are indeed consistent with their observed values of $\log g = 6.35$ and $T_{\mathrm{eff}} = 7\,600$ K (and their estimated mass of $0.136 - 0.162\ M_{\odot}$). Brown et al. (2013)

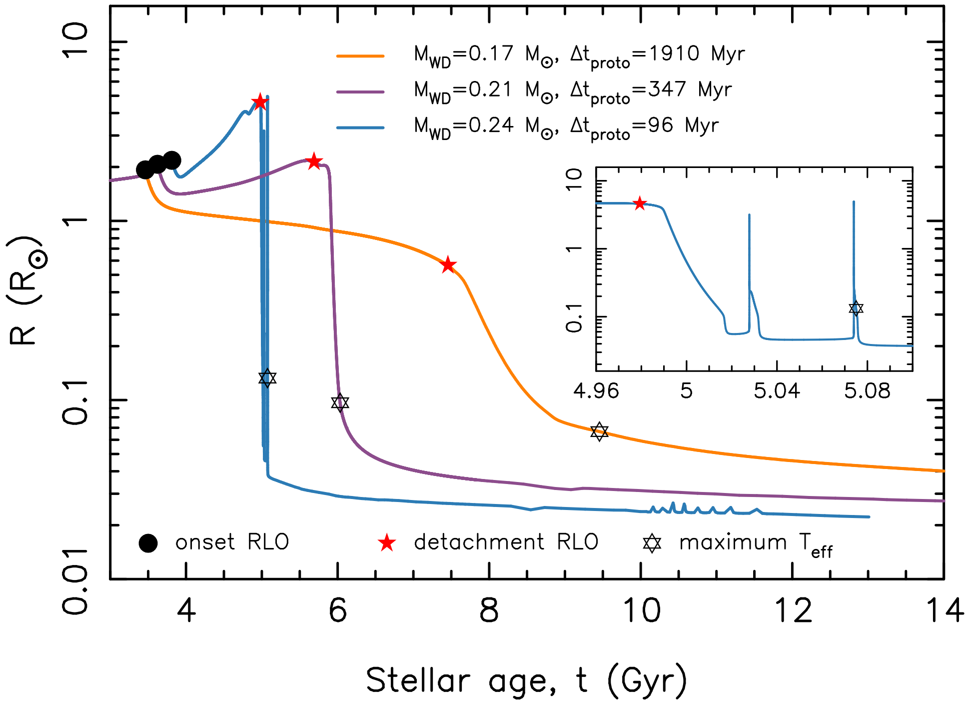

Figure 3.3: Radius as a function of stellar age for the progenitor stars of three He WDs of mass 0.17, 0.21 and 0.24 $M_\odot$. The most massive proto-WD evolves with hydrogen shell flashes – see inset. The epoch between the solid red star (RLO termination) and the open black star (max. T_{eff}) marks the contraction (transition) timescale, $\Delta t_{\mathrm{proto}}$ = 96 – 1910 Myr.

recently detected four binaries with low-mass WDs having $\log g \simeq 5$, in accordance with our modelling of proto-He WDs presented here (cf. Figs. 3.1 and A.1).

3.4.3 Bloated, hot, low-mass He WDs detected by *Kepler*

Four (proto) He WDs have been found with A-star companions in the combined transit and eclipse data from the *Kepler* mission (van Kerkwijk et al. 2010; Carter et al. 2011; Breton et al. 2012). Three of these He WDs (KOI–74, KIC 10657664, KOI–1224) have $M_{\mathrm{WD}} \lesssim 0.26\ M_\odot$ and are also plotted in Fig. 3.1. The mass estimates of these WDs are not very precise. However, within 1–2σ, the characteristics of these objects also seem to match our evolutionary tracks reasonably well.

The question now is why we see all these bloated proto-WDs given that WDs spend significantly more time on the subsequent cooling tracks. This is simply a selection effect. The WDs are only seen to eclipse A-stars in the *Kepler* data as long as they are bloated proto-WDs (and thus also more luminous than ordinary WDs, which have already settled on the cooling track).

3.5 Discussion and conclusions

We have demonstrated that low-mass ($\lesssim 0.20\ M_\odot$), detached proto-He WDs may spend up to ~2 Gyr in the contraction (transition) phase from the Roche-lobe detachment until they reach the WD cooling track. This is important for an age determination of He WDs in general and for recycled MSPs in particular. We expect a fair number of He WDs to be observed in this (bloated) phase, in agreement with recent observations.

The duration of this contraction phase ($\Delta t_{\mathrm{proto}}$) decreases strongly with increasing mass of the proto-He WD, M_{WD}. This can be understood from the well-known correlation between degenerate core mass and luminosity of an evolved low-mass star. Therefore, after Roche-lobe detachment, the rate at which the residual ($0.01 \pm 0.005\ M_{\odot}$) hydrogen in the envelope is consumed is directly proportional to the luminosity and thus M_{WD}. The value of $\Delta t_{\mathrm{proto}}$ is not particularly sensitive to the occurrence or absence of flashes.

Whether or not hydrogen shell flashes occur depends on the WD mass, its chemical composition, and the treatment of diffusion (mixing) of the chemical elements (e.g. Driebe et al. 1998; Sarna et al. 2000; Althaus et al. 2001c; Nelson et al. 2004; Althaus et al. 2013). In general, we find flashes in our models with $0.21 \leq M_{\mathrm{WD}}/M_{\odot} \leq 0.28$ for $M_2 \leq 1.5\ M_{\odot}$. This result agrees excellently well agreement with the interval found by Nelson et al. (2004) for donors with solar metallicity, and also with the earlier work of Driebe et al. (1998). For $M_2 = 1.6\ M_{\odot}$ WDs down to $\sim 0.18\ M_{\odot}$ are experiencing flashes.

Detailed studies by Althaus et al. (2001c, 2013) found hydrogen shell flashes for a much broader range of final WD mass ($0.18 < M_{\mathrm{WD}}/M_{\odot} < 0.41$). However, as pointed out by Nelson et al. (2004), diffusion is an extremely fragile process, and turbulence can mitigate its effects. And more importantly, Nelson et al. (2004) find that both M_2 and the mode of angular momentum losses may also affect the range for which hydrogen shell flashes occur. Indeed, we found a lower value of $M_{\mathrm{flash}} = 0.18\ M_{\odot}$ for our models with $M_2 = 1.6\ M_{\odot}$. It has previously been shown that M_{flash} strongly increases with lower metallicity (e.g. Sarna et al. 2000; Nelson et al. 2004). The work of Althaus et al. (2013) was calculated for a constant $M_2 = 1.0\ M_{\odot}$ ($Z = 0.01$). We have excluded such models with $M_2 < 1.1\ M_{\odot}$ ($Z = 0.02$) since these progenitor stars do not detach from their LMXB and evolve onto WD cooling track within a Hubble time.

Chemical diffusion via gravitational settling and radiative levitation was not included in this work. These effects seem to slightly increase $\Delta t_{\mathrm{proto}}$ compared with models without diffusion (L. Nelson et al., in prep.). A systematic investigation of these and other effects on $\Delta t_{\mathrm{proto}}$ and M_{flash} will be addressed in a future work.

Acknowledgements AGI acknowledges discussions with L. Nelson, P. Marchant, R. Stancliffe and L. Grassitelli. JA acknowledges financial support by the ERC Starting Grant no. (279702, BEACON, led by P. Freire).

CHAPTER 4

Models of low-mass helium white dwarfs including gravitational settling, thermal and chemical diffusion, and rotational mixing

Alina G. Istrate, Pablo Marchant, Thomas M. Tauris, Norbert Langer,
Richard J. Stancliffe and Luca Grassitelli

accepted to Astronomy & Astrophysics

Abstract A large number of extremely low-mass helium white dwarfs (ELM WDs) have been discovered in recent years. The majority of them are found in close binary systems suggesting they are formed either through a common-envelope phase or via stable mass transfer in a low-mass X-ray binary (LMXB) or a cataclysmic variable (CV) system. Here, we investigate the formation of these objects through the LMXB channel with emphasis on the proto-WD evolution in environments with different metallicities. We study for the first time the combined effects of rotational mixing and element diffusion (e.g. gravitational settling, thermal and chemical diffusion) on the evolution of proto-WDs and on the cooling properties of the resulting WDs. We present state-of-the-art binary stellar evolution models computed with MESA for metallicities of $Z = 0.02$, 0.01, 0.001 and 0.0002, producing WDs with masses between $\sim 0.16 - 0.45\ M_{\odot}$. Our results confirm that element diffusion plays a significant role in the evolution of proto-WDs that experience hydrogen shell flashes. The occurrence of these flashes produces a clear dichotomy in the cooling timescales of ELM WDs, which has important consequences e.g. for the age determination of binary millisecond pulsars. In addition, we confirm that the threshold mass at which this dichotomy occurs depends on metallicity. Rotational mixing is found to counteract the effect of gravitational settling in the surface layers of young, bloated ELM proto-WDs and therefore plays a key role in determining their surface chemical abundances, i.e. the observed presence of metals in their atmospheres. We predict that these proto-WDs have helium-rich envelopes through a significant part of their lifetime. This is of great importance as helium is a crucial ingredient in the driving of the $\kappa-$mechanism suggested for the newly observed ELM proto-WD pulsators. However, we find that the number of hydrogen shell flashes and, as a result, the hydrogen envelope mass at the beginning of the cooling track, are not influenced significantly by rotational mixing. In addition to being dependent on proto-WD mass and metallicity, the hydrogen envelope mass of the newly formed proto-WDs depends on whether or not the donor star experiences a temporary contraction when the H-burning shell crosses the hydrogen discontinuity left behind by the convective envelope. The hydrogen envelope at detachment, although small compared to the total mass of the WD, contains enough angular momentum such that the spin frequency of the resulting WD on the cooling track is well above the orbital frequency.

4.1 Introduction

Extremely low-mass white dwarfs (ELM WDs) are low-mass helium-core WDs with masses below $0.2 - 0.3\ M_{\odot}$ and with surface gravities of $5 < \log g < 7$ (Brown et al. 2013). A large number of such objects have been discovered in recent years through dedicated or general surveys such as ELM, SPY, WASP, SDSS and the *Kepler* mission (e.g. Brown et al. 2010; Kilic et al. 2011; Brown et al. 2012; Kilic et al. 2012; Brown et al. 2013; Koester et al. 2009; Maxted et al. 2011; Kepler et al. 2015; Brown et al. 2016). Soon after the discovery of the first ELM WDs, it was recognised that they have to be a product of binary evolution (Marsh et al. 1995b). From an evolutionary point of view, these ELM WDs cannot be formed from single-star progenitors as the nuclear evolution timescale of such low-mass objects would exceed the Hubble time – unless they have an extremely high metallicity (Kilic et al. 2007) or the star lost its envelope from an inspiralling giant planet (Nelemans & Tauris 1998). Indeed, the vast majority of ELM WDs are found in binary systems with a companion star such as a neutron star in millisecond pulsar (MSP) systems (van Kerkwijk et al. 2005), an A-type star in EL CVn-type systems (Maxted et al. 2014a) or another (typically a carbon-oxygen) WD. ELM WDs have been discovered in various environments, from the Galactic disk to open and globular clusters (Rivera-Sandoval et al. 2015; Cadelano et al. 2015), and thus they can be formed from progenitors with different metallicities.

The revived interest in ELM WDs was fostered by the discovery of pulsations in several of these objects (Hermes et al. 2012d, 2013b,c; Kilic et al. 2015) as well as ELM proto-WDs (Maxted et al. 2013, 2014b; Corti et al. 2016; Gianninas et al. 2016). The ELM WD pulsators extend the ZZ Ceti instability strip to lower effective temperatures and higher luminosities. This instability strip contains stars with a convective driving mechanism for pulsations acting at the base of the convective zone associated with hydrogen recombination (e.g. Van Grootel et al. 2013b). In the newly discovered ELM proto-WD pulsators, the excitation mechanism is instead the usual $\kappa-$ mechanism for which the presence of He in the envelope is thought to play a key role (Jeffery & Saio 2013; Córsico et al. 2016). The pulsational behaviour of ELM WDs and ELM proto-WDs provide an unique insight into their interior properties, such as the hydrogen envelope mass and their total mass and rotation rate, which will place stronger constraints on the theoretical models (e.g. Córsico & Althaus 2014a,b; Córsico et al. 2016).

Another interesting and not completely understood feature of ELM WDs is the observed presence of metals in their atmospheres. Gianninas et al. (2014a) provided for the first time systematic measurements of the atmospheric abundances of He, Ca and Mg for this type of stars and examined their distribution as a function of effective temperature and mass. In the observed sample, all the WDs with $\log\ g < 5.9$ show Ca II K lines, suggesting that the presence of metals in these objects is a ubiquitous phenomenon, possibly linked to their evolution. Detailed abundance analyses exist for only a handful of objects (Kaplan et al. 2013; Gianninas et al. 2014b; Hermes et al. 2014b; Latour et al. 2016) but already suggest a diversity of metallicities, as in the case of sdB stars. Gravitational settling depletes the metals in the atmospheres of WDs on a very short timescale compared to their evolutionary timescale (Vauclair et al. 1979; Paquette et al. 1986; Koester et al. 2009), indicating that a process should be at work that counteracts it or replenishes the depleted metals.

In addition to the formation and evolutionary history of these objects, their future outcome is also of theoretical interest. Short-period double WD binaries are candidate progenitors for transient explosive phenomena such as Type Ia, underluminous .Ia and Ca-rich supernovae (Bildsten et al. 2007; Iben & Tutukov 1984; Perets et al. 2010; Foley 2015), as well as exotic systems such as AM CVn stars, R Coronae Borealis (R CrB), and single subdwarf B/O stars (Kilic et al. 2014; Solheim 2010; Clayton 2013; Heber 2016). Moreover, they are expected to be excellent sources of gravitational waves (Hermes et al. 2012b; Kilic et al. 2013) and verification sources for gravitational detectors such as *eLISA* (Amaro-Seoane et al. 2012).

4.2 Formation and evolution of ELM WDs

From a theoretical point of view, an ELM WD can be formed either through common-envelope evolution or stable Roche-lobe overflow (RLO) mass transfer in a low-mass X-ray binary (LMXB) or a cataclysmic variable (CV) system. The formation and evolution of low-mass WDs through a stable mass-transfer phase (or by artificially removing envelope mass from its progenitor star) has been studied intensively over the years (e.g. Driebe et al. 1998; Sarna et al. 2000; Nelson et al. 2004; Althaus et al. 2001a; Panei et al. 2007; Althaus et al. 2013; Istrate et al. 2014a,b). In comparison, the common-envelope channel is less studied and far more uncertain (e.g. Nandez et al. 2015).

Although the majority of ELM WDs are found in double WD systems (Andrews et al. 2014), almost all evolutionary calculations that involve stable mass transfer producing an ELM WD consider a neutron star companion (i.e. an LMXB progenitor system). For the structure of the final ELM WDs, the results of these LMXB calculations can also be applied to CV systems producing ELM WDs in double WD binaries, as the stellar properties of the produced ELM WDs do not depend on the mass of their accreting companion, but instead on the initial orbital period and mass of the donor (progenitor) star (Nelson et al. 2004; De Vito & Benvenuto 2010; Istrate et al. 2014a). Only the orbital periods of the produced ELM WDs will be different.

4.2.1 Hydrogen shell flashes and proto-WDs

After the RLO mass-transfer phase ends, the remaining donor star goes through a so-called (bloated) proto-WD phase in which a significant part of the hydrogen left in the envelope is burned through stable hydrogen shell burning. In addition to this, depending on the mass of the proto-WD, its metallicity and the physics included in the modelling, hydrogen may be burned through short-lived phases of unstable burning through CNO hydrogen shell flashes (e.g. Driebe et al. 1998; Althaus et al. 2001c; Nelson et al. 2004).

Figure 4.1 shows an example of the formation of an ELM WD through the LMXB channel, including the evolution as a proto-WD as well as its further cooling. The stellar track is computed from the zero-age main sequence (ZAMS) until the donor star reaches an age of 14 Gyr, points 0 and 12, respectively, in Fig. 4.1. In this case, the star experiences one hydrogen shell flash. After the Roche-lobe detachment (point 2), the proto-WD goes through a phase of contraction at almost constant luminosity and increasing effective temperature (between points 2 and 3). The total luminosity is dominated by CNO burning while the contribution due to release of gravitational binding energy from contraction is negligible. When the proto-WD reaches point 3, which is at the beginning of the cooling branch, the temperature in the burning shell is too low to sustain CNO burning, therefore the main contribution to the total luminosity is for a while given by contraction, until the star switches to pp-burning. The unstable burning starts around point 4 and CNO burning becomes dominant again. The increasing energy release during the flash development creates a steep temperature gradient close to the location of maximum energy production. This will give rise to a pulse-driven convection zone within the hydrogen burning shell. After the convection zone is fully developed, the evolution becomes faster (between points 5 and 6). Around point 7, the convection zone reaches the stellar surface, and consequently, its surface chemical composition is altered. The maximum hydrogen luminosity reached during the flash is supplied by the pp-burning, although the onset of the instability is triggered by the CNO cycling. Between points 7 and 8, the lower boundary of the pulse-driven convection zone moves upwards, and at point 8 it completely vanishes. Beyond point 8, the contraction of the inner shells resumes, while the surface layers react by expansion, resulting in a redward motion in the HR-diagram that almost brings the proto-WD back to the red-giant branch. At point 9, the star fills its Roche lobe again and a short episode of mass transfer

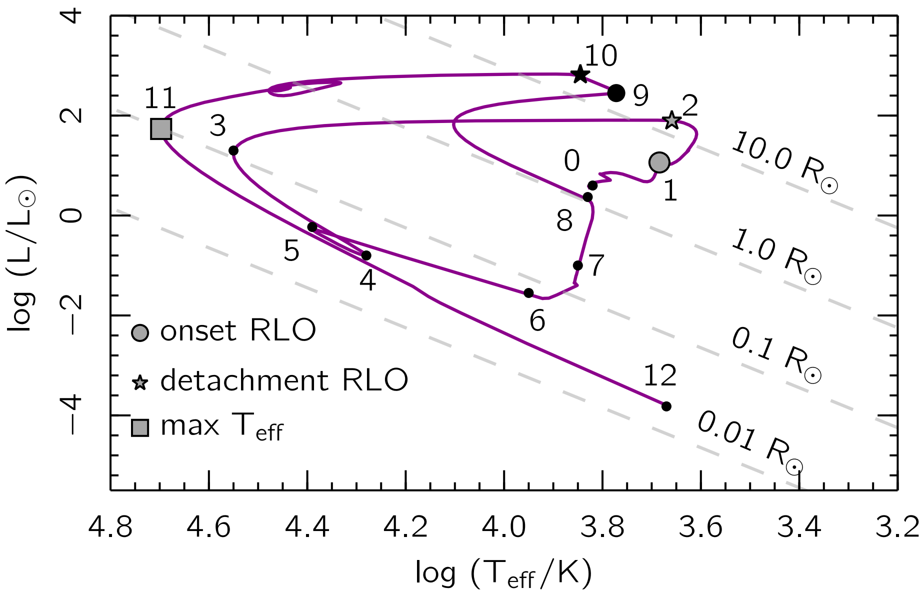

Figure 4.1: Hertzsprung-Russel (HR) diagram showing the formation and cooling of a 0.28 $M_\odot$ helium WD (produced in an LMXB) that undergoes a hydrogen shell flash. The initial progenitor mass is 1.4 $M_\odot$ ($Z = 0.02$), the neutron star mass is 1.2 $M_\odot$, and the initial orbital period is 5.0 days. See Table 4.1 for ages at each stage.

is initiated (between points 9 and 10) with a high mass-transfer rate that approaches $\sim 10^{-7}\ M_\odot\,\mathrm{yr}^{-1}$. After point 10, the star again evolves towards a high surface temperature at almost constant luminosity, and before reaching the final cooling track, it develops a so-called subflash (near $\log T_{\mathrm{eff}} = 4.4$). The time intervals for each of the above described phases are shown in Table 4.1.

The proto-WD phase has an associated timescale, $\Delta t_{\mathrm{proto}}$, which is the time it takes the star to evolve (and contract) from the Roche-lobe detachment until it reaches its maximum effective temperature on the (final) cooling track. In Fig. 4.1 this corresponds to the time interval during the evolution from point 2 to point 11. The duration of this contraction phase is mainly given by the burning rate of the residual hydrogen in the envelope. For evolved low-mass stars there is a well-known correlation between the degenerate core mass and its luminosity (Refsdal & Weigert 1971). Therefore, after Roche-lobe detachment, the rate at which the residual hydrogen in the envelope is consumed is directly proportional to the luminosity and thus increases strongly with M_{WD}. A detailed analysis of the dependence of $\Delta t_{\mathrm{proto}}$ on the mass of the WD is given in Istrate et al. (2014b). This timescale is especially important in MSP systems and should be added to the optically determined cooling age of the WD to yield the true age of the recycled radio pulsar. Unfortunately, the true age of a recycled pulsar cannot be determined from its characteristic spin-down age as this method has proved unreliable by a factor of 10 or more (Camilo et al. 1994; Tauris 2012; Lorimer et al. 1995; Tauris et al. 2012).

Hydrogen shell flashes occur in a range of proto-WD masses that is dependent on the metallicity and whether or not element diffusion is included in the modelling. The lower mass limit for flashes, $M_{\mathrm{flash,min}}$, is determined by the size of the burning shell, such that if $M_{\mathrm{proto-WD}} < \mathrm{M}_{\mathrm{flash,min}}$, then the shell is too thick to trigger unstable hydrogen burning. The upper mass limit, $M_{\mathrm{flash,max}}$, is determined by the cooling time of the burning shell, which needs to be long enough to avoid an extinction of the shell before the instability is fully established (if $M_{\mathrm{proto-WD}} > M_{\mathrm{flash,max}}$, this condition is not fulfilled, cf. Driebe et al. 1998). These conditions are altered when element diffusion is included (Althaus et al. 2001c), and this issue is investigated more carefully in Sect. 4.4.

Table 4.1: Evolution as a function of time for a 0.28 $M_\odot$ proto-WD evolving through a hydrogen shell flash, as plotted in Fig. 4.1. The ZAMS is at point 0, and the onset of RLO (the LMXB phase) is at point 1. The relative age is in comparison to the previous point of evolution and the WD age is with respect to the Roche-lobe detachment (point 2). See text for more details.

Point	Relative age (Myr)	WD age (Myr)
0	–	–
1	3330	–
2	217	0
3	4.92	4.92
4	6.63	11.5
5	57.1	68.7
6	0.0066	68.7
7	2.4×10^{-5}	68.7
8	3.8×10^{-5}	68.7
9	1.5×10^{-5}	68.7
10	3.1×10^{-5}	68.7
11	0.193	68.9
12	10 700	10 800

4.2.2 Age dichotomy in helium WD cooling?

The occurrence of hydrogen shell flashes, when element diffusion is taken into account, has been found to be responsible for a dichotomy in the cooling ages of helium WDs (Althaus et al. 2001a; van Kerkwijk et al. 2005; Althaus et al. 2013; Bassa et al. 2016). The occurrence of flashes in relatively massive helium WDs ($> 0.2\ M_\odot$), with initially thin hydrogen envelopes, leaves behind an even thinner envelope, giving rise to relatively fast cooling. On the other hand, less massive (proto) helium WDs ($< 0.2\ M_\odot$) have thicker hydrogen envelopes after RLO, resulting in stable shell hydrogen burning, and will therefore continue residual hydrogen burning on the cooling track on a long timescale.

Recently, Istrate et al. (2014b) found no evidence for such a dichotomy in the case of thermal evolution of proto-WDs but rather a smooth transition with the mass of the WD. The authors showed that the thermal evolution timescale mainly depends on the proto-helium WD luminosity, which in turn depends on the mass of the proto-WD and not on the occurrence of hydrogen shell flashes. These new findings questioned whether a dichotomy exists in the cooling ages of ELM WDs and if the responsible process might be the occurrence of hydrogen shell flashes.

4.2.3 Aims of this investigation of ELM WDs

The focus of this paper is on the proto-WD phase of ELM WDs, which are investigated through a series of binary stellar evolution calculations of LMXBs. The following aspects are addressed: (i) the hydrogen envelope mass as a result of binary evolution, (ii) the role played by rotational mixing in the evolution of ELM proto-WDs, (iii) the influence of element diffusion and rotation on $\Delta t_{\mathrm{proto}}$ as well as on the cooling timescale, (iv) the existence of a dichotomy in the cooling ages of ELM WDs as a result of the occurrence of hydrogen shell flashes, (v) the presence of metals in the atmospheres of proto-WDs, and (vi) the relation between the mass of a proto-WD and its orbital period at the end of the mass-transfer phase. All these aspects are addressed not only as a function of the proto-WD mass, but also as a function of metallicity. Answering these open questions is essential for understanding the formation of ELM WDs and their age determination, for providing accurate models for astroseismology calculations, and for determining the correct age of MSP binaries. This work extends the previous work by Istrate et al. (2014b) by including element diffusion and rotational mixing in the evolution of the donor star and during the proto-WD and the WD cooling phase. Moreover, the study is extended to include the effect of metallicity as well, for which we investigate four metallicities: $Z = 0.02$, 0.01, 0.001, and 0.0002.

4.3 Numerical methods

The evolutionary tracks presented in this paper are calculated using the publicly available binary stellar evolution code MESA, version 7624 (Paxton et al. 2011, 2013, 2015). The nuclear network used is `cno_extras.net` and accounts for the CNO burning with the following isotopes: ^{1}H, ^{3}He, ^{4}He, ^{12}C, ^{13}C, ^{13}N, ^{14}N, ^{15}N, ^{14}O, ^{15}O, ^{16}O, ^{17}O, ^{18}O, ^{17}F, ^{18}F, ^{19}F,^{18}Ne, ^{19}Ne, ^{20}Ne, ^{22}Mg and ^{24}Mg. Radiative opacities are taken from Ferguson et al. (2005) for $2.7 \leq \log T \leq 4.5$ and OPAL (Iglesias & Rogers 1993, 1996) for $3.75 \leq \log T \leq 8.7$ and conductive opacities are adopted from Cassisi et al. (2007). Convective regions are treated using the mixing-length theory (MLT) in the Henyey et al. (1965) formulation with $\alpha_{\rm MLT} = 2.0$. Transport of angular momentum is treated as a diffusive process which results in rigid rotation in convective zones. The boundaries of convective regions are determined using the Schwarzschild criterion. A step function overshooting extends the mixing region for 0.2 pressure scale heights beyond the convective boundary during core H-burning.

We here refer to element diffusion as the physical mechanism for mixing of chemical elements that is due to pressure gradients (or gravity, i.e. gravitational settling), temperature (thermal diffusion) and composition gradients (chemical diffusion). Gravitational settling tends to concentrate heavier elements towards the centre of the star. Thermal diffusion generally acts in the same direction, although to a lesser degree, by bringing highly charged and more massive species towards the hottest region of the star (its centre). Chemical diffusion, on the other hand, has the opposite effect (e.g. Iben & MacDonald 1985; Thoul et al. 1994). MESA includes the treatment of element diffusion through gravitational settling, chemical and thermal diffusion (Thoul et al. 1994), and radiative accelerations (Hu et al. 2011). Radiative forces are proportional to the reciprocal of the temperature and are thus negligible in hot regions where nuclear burning is of importance. In addition, calculating these forces is computationally demanding. We therefore here neglected the effects of radiative levitation (which is important for determining photospheric composition of hot WDs (Fontaine & Michaud 1979). The detailed description of how element diffusion is implemented in MESA can be found in Paxton et al. (2015). We take into account the effects of element diffusion due to gravitational settling and chemical and thermal diffusion for the following elements ^{1}H, ^{3}He, ^{4}He, ^{12}C, ^{13}C, ^{14}N, ^{16}O, ^{20}N, ^{24}Mg, and ^{40}Ca.
MESA includes the effects of the centrifugal force on stellar structure, chemical mixing, and transport of angular momentum that is due to rotationally induced hydrodynamic and secular instabilities as described in Heger et al. (2000). Here, we take into account the mixing due to dynamical shear instability, secular shear instability, Eddington-sweet circulation, and Goldreich-Schubert-Fricke instability with a mixing efficiency factor of $f_c = 1/30$ (Heger et al. 2000). The mixing of angular momentum that is due to dynamo-generated magnetic fields in radiative zones is also included (Spruit 2002; Heger et al. 2005) as is the angular momentum transport due to electron viscosity (Itoh et al. 1987). A decrease of the mean molecular weight with radius has a damping effect on mixing processes driven by rotation or even prevents these from occurring. The strength of this effect is regulated by the parameter f_{μ}, for which we follow Heger et al. (2000) and set f_{μ}=0.05.

The initial metallicity was set to $Z = 0.02$ (Y=0.28), with initial abundances from Grevesse & Sauval (1998). The lower metallicities were obtained by scaling both X and Y by the same factor such that

$X + Y + Z = 1$. For the WD evolution and for $T_{\rm eff} < 10\,000$ K, the outer boundary conditions were derived using non-grey model atmospheres (Rohrmann et al. 2012).

To calculate the rate of change of orbital angular momentum, we took into account contributions from gravitational wave radiation, mass loss, magnetic braking, and spin orbit couplings:

$$\dot{J}_{\rm orb} = \dot{J}_{\rm gwr} + \dot{J}_{\rm ml} + \dot{J}_{\rm mb} + \dot{J}_{\rm ls}\,, \tag{4.1}$$

as described in Paxton et al. (2015). The contribution of spin-orbit couplings to $\dot{J}_{\rm orb}$ was computed by demanding conservation of total angular momentum (except for losses due to gravitational wave radiation, magnetic braking, and mass loss), that is, changes in spin angular momentum were compensated for by changing the orbital angular momentum. The initial rotation velocity of the donor star was set by requiring that its spin period be synchronized with the initial orbital period. The time evolution of the angular velocity of the donor star is given by

$$\frac{d\Omega_i}{dt} = \frac{\Omega_{\rm orb} - \Omega_i}{\tau_{\rm sync}}, \tag{4.2}$$

where Ω_i is the angular velocity of cell i (Detmers et al. 2008). The synchronization time, $\tau_{\rm sync}$ was calculated using the formalism of tidal effects from Hurley et al. (2002) and depends on whether the envelope is convective or radiative.

4.3.1 Grid of models

To produce our grid of models, we followed the detailed binary evolution of the donor star from the ZAMS until it reached an age of 14 Gyr. The neutron star was treated as a point mass. The final outcome of these LMXB systems is very sensitive to the initial orbital period and to the treatment of orbital angular momentum loss (e.g. Istrate et al. 2014a, and references therein).

We calculated binary tracks for four metallicities: $Z = 0.02$, 0.01, 0.001, and 0.0002. For each metallicity, the models were divided into three categories: (i) basic models (with no diffusion nor rotation), (ii) diffusion models (with element diffusion) and, (iii) diffusion+rotation models (with element diffusion plus rotation). In both the diffusion and diffusion+rotation models, we included the effects of centrifugal forces and angular momentum transport, which means that these two models only differ by the presence of rotational mixing in the rotation models.

For $Z = 0.02$, the initial binary configuration has a 1.4 $M_\odot$ donor star and a 1.2 $M_\odot$ neutron star accretor. For all the other metallicities, our models were calculated with a 1.0 $M_\odot$ donor star and a 1.4 $M_\odot$ neutron star (to facilitate direct comparison with previous work in the literature, see Sect. 4.5.2). All the models were computed using a magnetic braking index of $\gamma = 4$, and we assumed that 30 per cent of the transferred mass is ejected from the neutron star as a fast wind carrying its specific orbital angular momentum. We note that the structure of the ELM WDs is not sensitive to the above choices of mass-transfer parameters which only affect their final orbital periods. A comprehensive study of the influence of the magnetic braking index and the accretion efficiency on LMXB evolution can be found in Istrate et al. (2014a). We point out again that we here refer to the mass of the proto-WD as being the (bloated) donor star mass at the end of the RLO mass-transfer phase (before the occurrence of flashes, which can lead to additional mass-transfer episodes), and the mass of the WD as being the mass at the beginning of the cooling track. We calculated models just above the bifurcation period, which is defined as the shortest initial orbital period that produces a WD (e.g. Istrate et al. 2014a, and references therein).

4.4 Results

4.4.1 General effects of element diffusion and rotational mixing

In the context of low-mass helium WDs, element diffusion was investigated in detail over the past few years by the La Plata group (e.g. Althaus & Benvenuto 2000; Serenelli et al. 2001; Althaus et al. 2001a,c,b; Panei et al. 2007; Althaus et al. 2009, 2013) using the stellar evolution code LPCODE for various ranges of helium WD masses and metallicity. To the best of our knowledge, there is only one other study that used MESA for low-mass helium WDs (Gautschy 2013). Our models include element diffusion from the ZAMS and not only from the proto-WD phase, as in the previous works. Moreover, for the first time, we investigate in detail the role played by rotational mixing in addition to element diffusion in the evolution of ELM WDs.

Element diffusion has a strong effect on the surface composition of a proto-WD and on the chemical profile deep inside the star close to the helium core. At the surface, gravitational settling increases the hydrogen abundance given that hydrogen is the lightest element. Close to the helium core boundary, chemical diffusion tends to smooth it out by mixing the hydrogen downwards into hotter layers because a large hydrogen abundance gradient exists. It has been shown that this hydrogen tail promotes the occurrence of hydrogen shell flashes (e.g. Althaus et al. 2001a). Moreover, when element diffusion is included, a proto-WD experiences more flashes than when diffusion is neglected (e.g. Althaus et al. 2001a). The WD mass interval in which they occur is also changed compared to the case when element diffusion is ignored. The number of flashes and other information for all the models studied in this work are given in Appendix B.

Figure 4.2 shows the evolution of surface gravity versus effective temperature for a proto-WD of $\sim 0.23\ M_{\odot}$ obtained from the following three model configurations: basic, diffusion, and diffusion+rotation. The basic model experiences three hydrogen shell flashes, while the diffusion and the diffusion+rotation models experience one additional flash. The radial expansion following the CNO burning is more pronounced when element diffusion is included, in some cases leading to additional episodes of RLO. In general, the models with diffusion and diffusion+rotation behave in a very similar way.

Figure 4.3 shows the evolution of hydrogen surface abundance (top panel) and log g (bottom panel) for the same (proto)WDs as in Fig. 4.2. As already mentioned, gravitational settling changes the surface abundances. All the elements heavier than hydrogen sink below the surface, leaving a pure hydrogen envelope behind. When rotational mixing is included, gravitational settling and rotational mixing compete with each other to determine the chemical composition of the surface. At the beginning of the proto-WD phase, rotational mixing dominates. However, the surface gravity of the proto-WD increases with time, while the efficiency of rotational mixing decreases, as described in Sect. 4.4.1. Thus, in later phases of the evolution, the gravitational settling overcomes the mixing induced by rotation. By the beginning of the last flash, the surface structure of the model that only includes element diffusion is nearly identical to the structure of the model that includes both element diffusion and rotational mixing. Helium in the envelopes of ELM proto-WDs is a crucial ingredient for exciting pulsation modes through the κ−mechanism, as shown by Jeffery & Saio (2013) and Córsico et al. (2016) for radial and nonradial modes. Gianninas et al. (2016) recently provided the first empirical evidence that pulsations in ELM proto-WDs can only occur when a significant amount of helium is present in their atmospheres. In contrast with evolutionary models that only include element diffusion, our new evolutionary models including rotational mixing produce proto-WDs that have mixed He/H envelopes during most of their evolution before settling on the cooling track.

Another effect of element diffusion, resulting mainly from the competition between chemical and thermal diffusion, is the development of a hydrogen tail that reaches down into the hot helium-rich layers, as

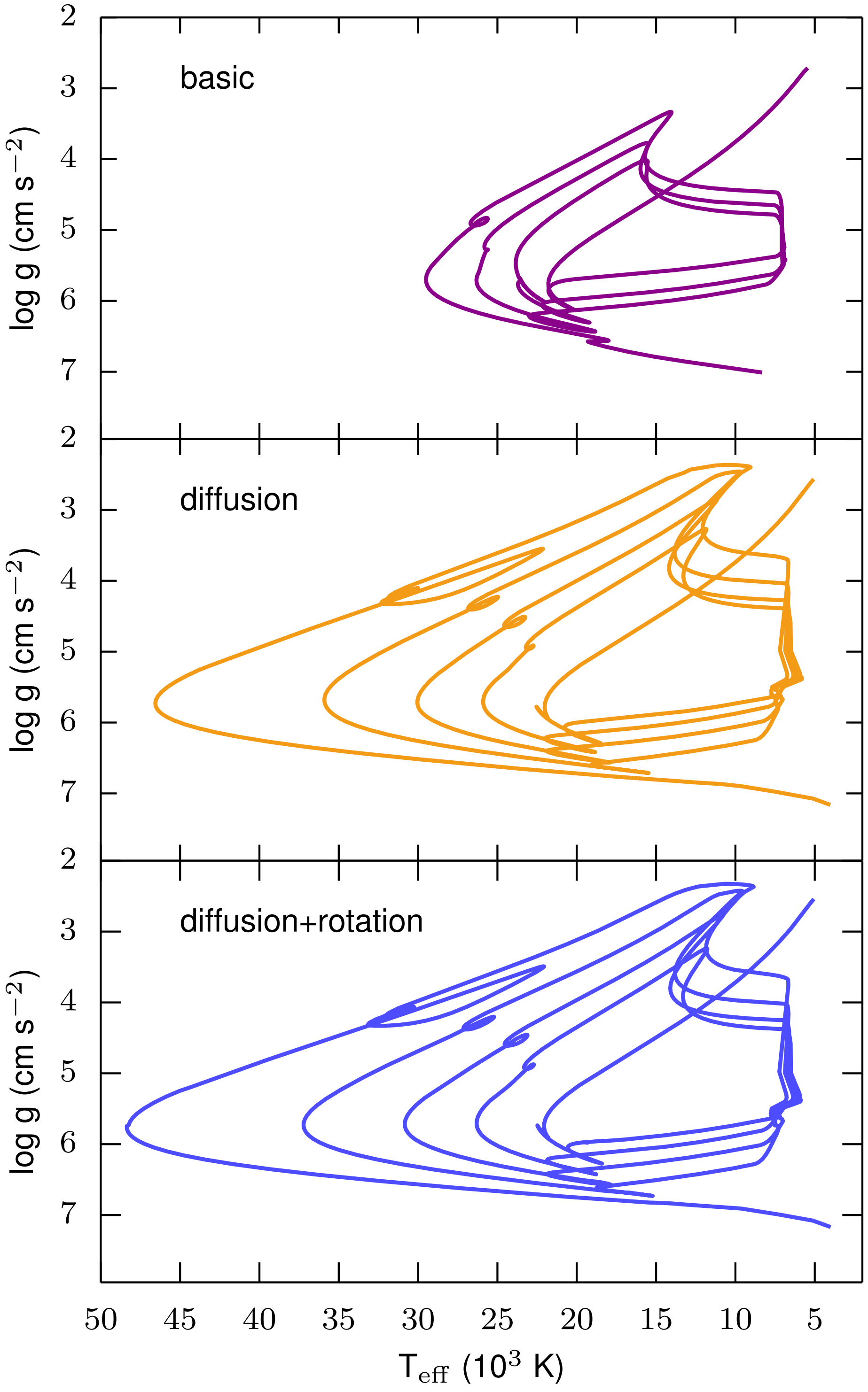

Figure 4.2: Post-RLO evolution of surface gravity versus effective temperature for a $\sim 0.23\ M_\odot$ proto-WD produced from an LMXB donor star with $Z = 0.01$. Three different models are shown: basic configuration (top panel), diffusion configuration (middle panel) and diffusion+rotation configuration (bottom panel). Note that the computations are stopped when the age of the model star reaches 14 Gyr (since ZAMS).

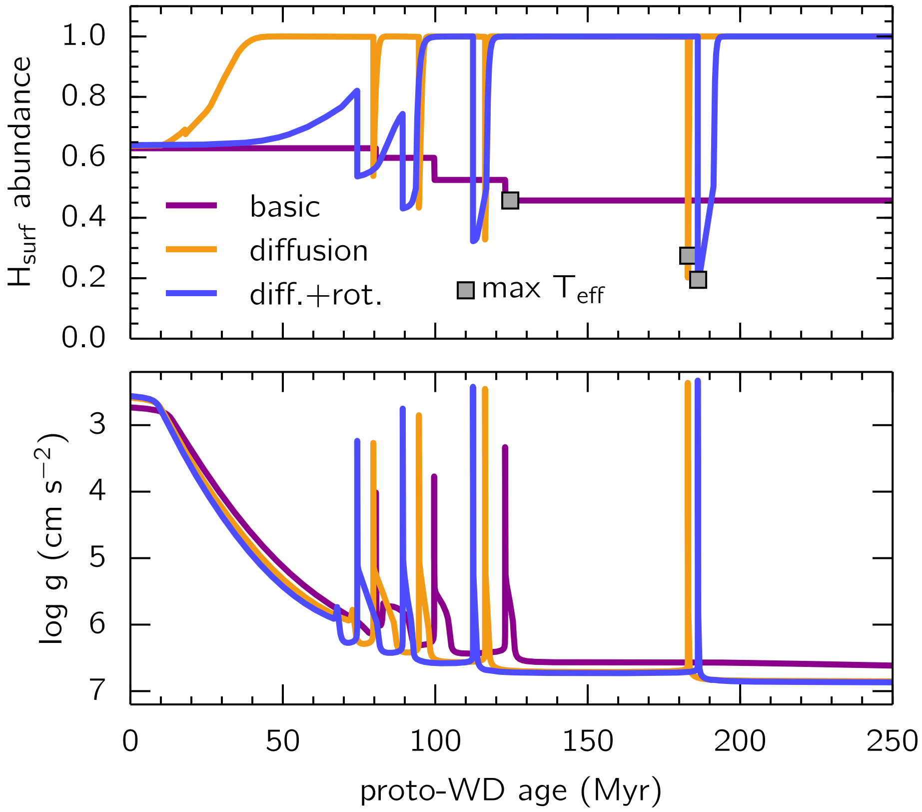

Figure 4.3: Evolution of hydrogen surface abundance (top panel) and log g (bottom panel) for the three proto-WDs shown in Fig. 4.2 illustrating the effect of gravitational settling, rotational mixing and the mixing due to convection zones developed during the hydrogen shell flashes on the surface composition of these objects.

shown in Fig. 4.4. This effect is responsible for the larger number of flashes compared to the case where element diffusion is ignored (basic model). Rotational mixing is seen not to change the chemical structure of the deep layers. This can also be concluded from the very similar behaviour in terms of the number of flashes and the structure of the flashes in the case that includes both diffusion and rotation compared to the case that only includes element diffusion, cf. Figs. 4.2 and 4.5.

In Fig. 4.5 we plot the luminosity produced by hydrogen burning versus the hydrogen envelope mass. For all three models, around 70 per cent of the hydrogen remaining from the end of the LMXB phase (Roche-lobe detachment) is processed before the occurrence of flashes while the bloated proto-WD crosses the HR–diagram. The occurrence of additional flashes, which applies to the cases where element diffusion is included, reduces the hydrogen envelope mass available on the cooling track (i.e. after reaching maximum $T_{\rm eff}$, marked by squares in Fig. 4.5) by a factor of ~ 3 compared with the basic model. The basic model still experiences significant residual hydrogen burning on the cooling track. As a result, the basic model only cools down to a temperature of $T_{\rm eff} \approx 8400\ K$ within 14 Gyr (since the ZAMS), while the two models that include diffusion will cool down to roughly $T_{\rm eff} \approx 4000\ K$ (cf. Fig. 4.2). The cooling properties of the ELM WDs are discussed in more detail in Sect. 4.4.5.

The orbital evolution of the models described above is shown in Fig. 4.6. One difference between the three models is that those with element diffusion (and rotation) require a longer initial orbital period to form approximately the same proto-WD. The orbital period at the Roche-lobe detachment is ~7.05 days for the model that includes diffusion and rotation, ~ 6.73 days for the model with diffusion only, and

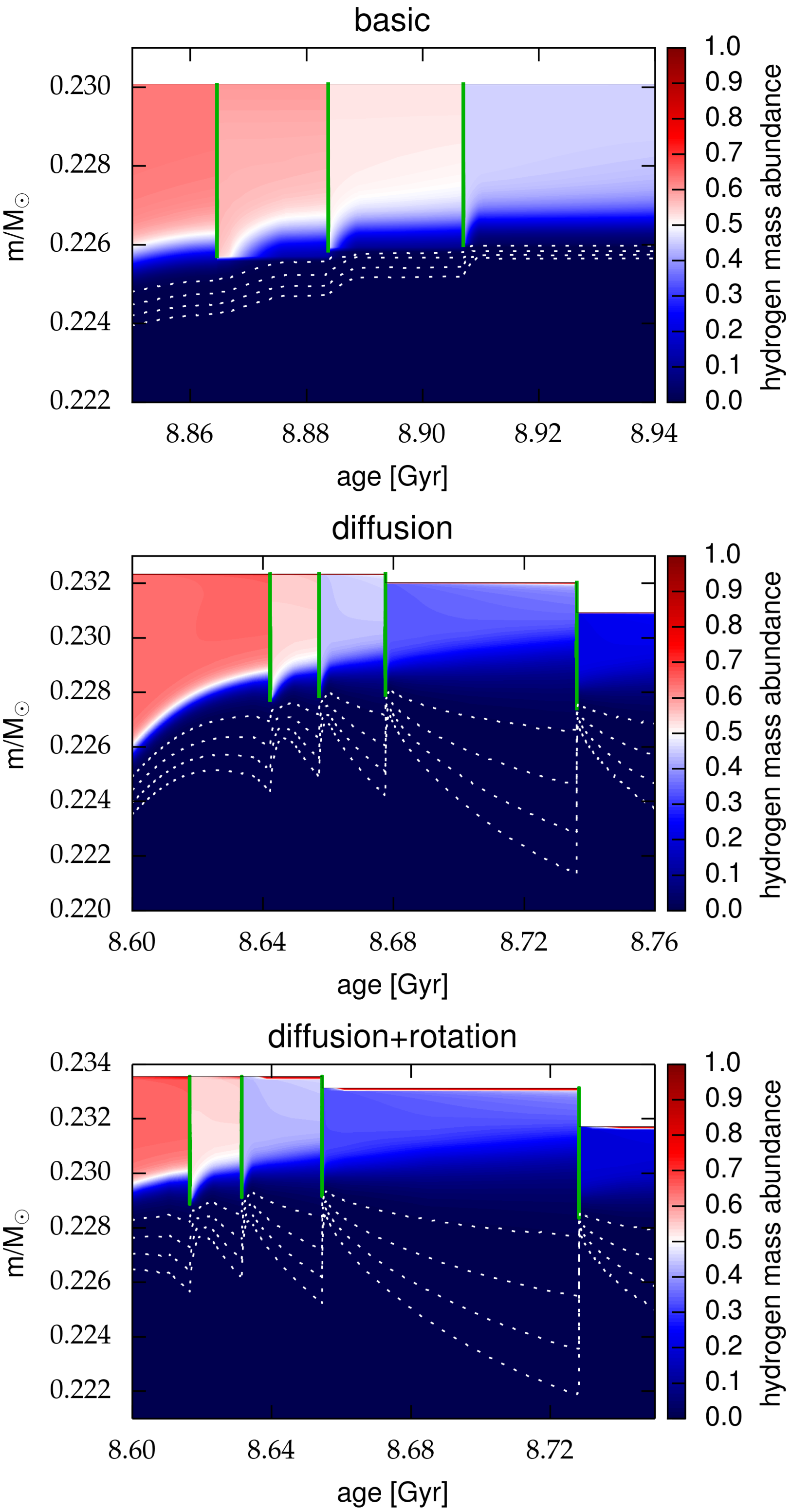

Figure 4.4: Kippenhahn diagrams showing the proto-WD phase for the same systems as in Figure 4.2. The plots show cross sections of the outer $\sim 0.01\ M_\odot$ envelope of the proto-WD in mass coordinates, along the y-axis, as a function of stellar age on the x-axis (relative to the ZAMS age). The green areas denote zones with convection; the dotted white lines define lines of constant hydrogen abundance, 10^{-2} to 10^{-5} (from top to bottom). The intensity of the blue and red colour indicates the hydrogen abundance by mass fraction, as shown on the colour scale to the right. As a result of different input physics, the proto-WDs have slightly different masses and ages. See text for details.

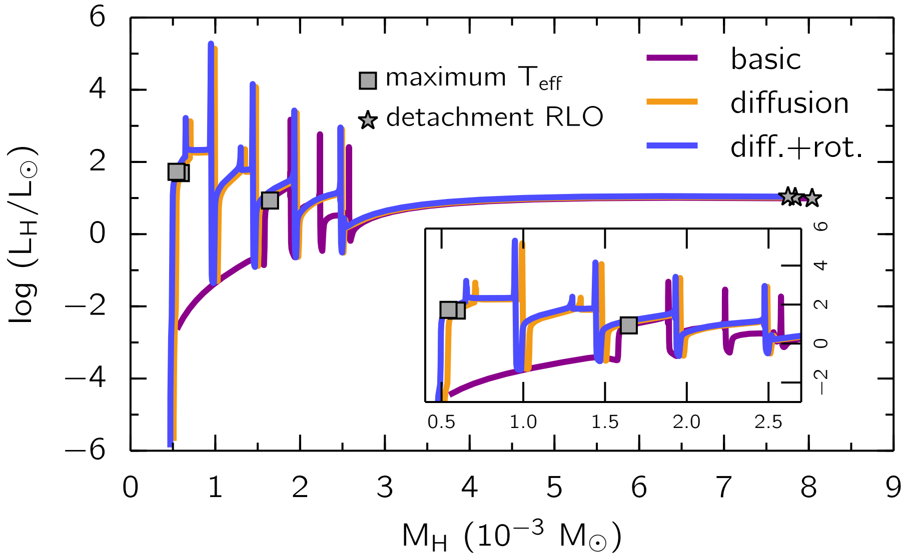

Figure 4.5: Hydrogen burning luminosity versus hydrogen envelope mass, for the same systems as in Fig. 4.2. The grey stars represent the moment of Roche-lobe detachment while the grey squares denote the point of maximum effective surface temperature. The evolution is from the right to the left.

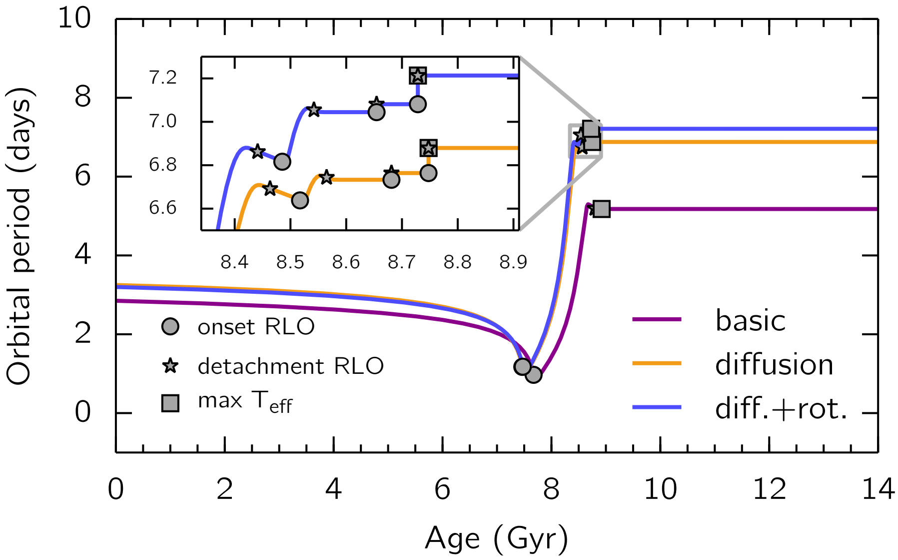

Figure 4.6: Orbital period evolution for the same models as in Fig. 4.2. The grey circles represent the onset of the mass transfer, the grey stars represent Roche-lobe detachment and the grey squares mark the maximum $T_{\rm eff}$.

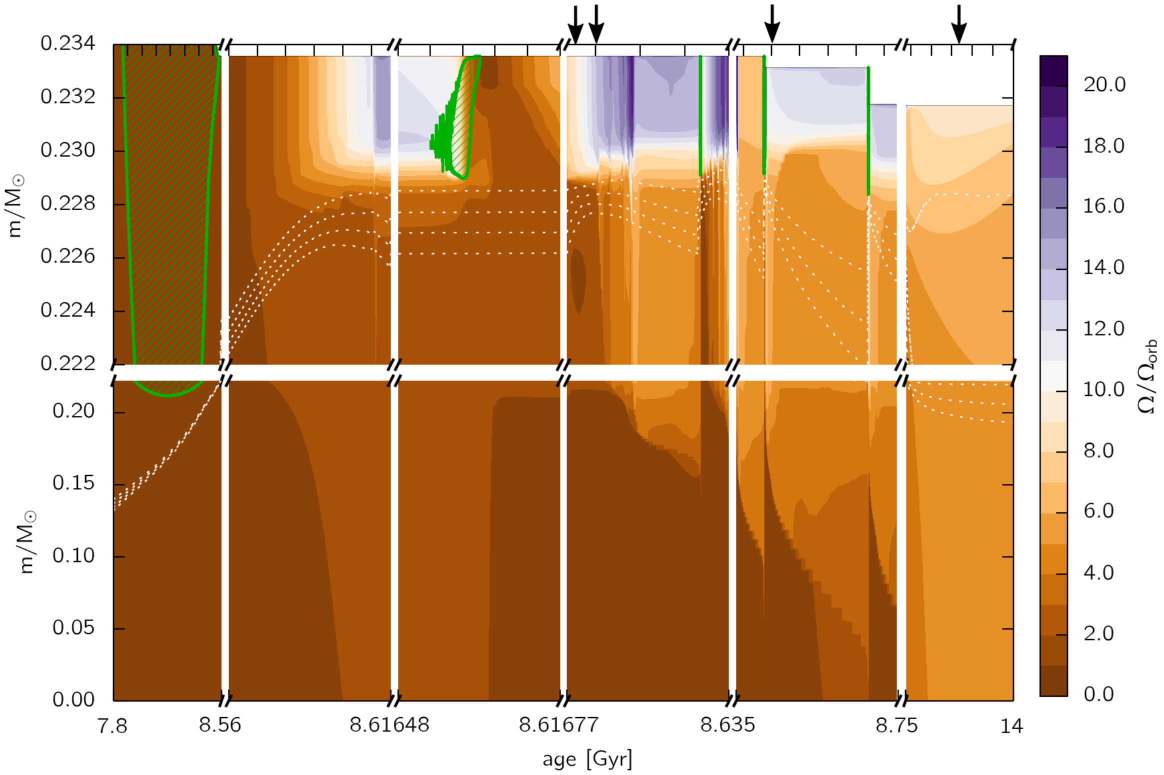

Figure 4.7: Kippenhahn diagram for the same proto-WD as in Fig. 4.4, including both element diffusion and rotational mixing. The intensity of the orange and indigo colour indicates the ratio of the spin angular velocity to the orbital angular velocity, $\Omega/\Omega_{\rm orb}$, as shown on the colour scale to the right. The green areas and the dotted white lines have the same meaning as in Fig. 4.4. The black arrows point to the position of the profiles in Fig. 4.8.

~ 5.19 days for the basic model. As the diffusion-induced flashes are stronger and because almost every flash causes the star to expand and fill its Roche lobe again, the mass-transfer episodes widen the orbit during each flash. In the end, this effect accounts for an increase of a few per cent in the orbital period.

Rotational mixing

As shown in Fig. 4.7, the tidal coupling is strong enough to completely synchronize the donor with the orbit up until the end of the LMXB phase. This changes dramatically after detachment from the Roche lobe; while the helium core barely contracts and spins up only slightly above the orbital frequency, the extended hydrogen envelope spins up significantly during contraction, resulting in strong shear at the core-envelope boundary. As hydrogen flashes develop and the star expands and then contracts, the envelope successively spins down and up, with the rotational period at the surface of the proto-WD at its maximum being up to 20 times shorter than the orbital period. Even though the proto-WD expands back and fills its Roche lobe during flashes, these phases are very short. The convective layers developed during the flashes disappear well before the next phase of Roche–lobe overflow such that tidal synchronization past the LMXB phase is negligible.

Although a strong shear is developed, the composition gradients that help stabilize the instabilities driven by rotation prevent the mixing of elements and angular momentum from the envelope to the core. This is shown in Fig. 4.8, where the different processes contributing to the angular momentum diffusion

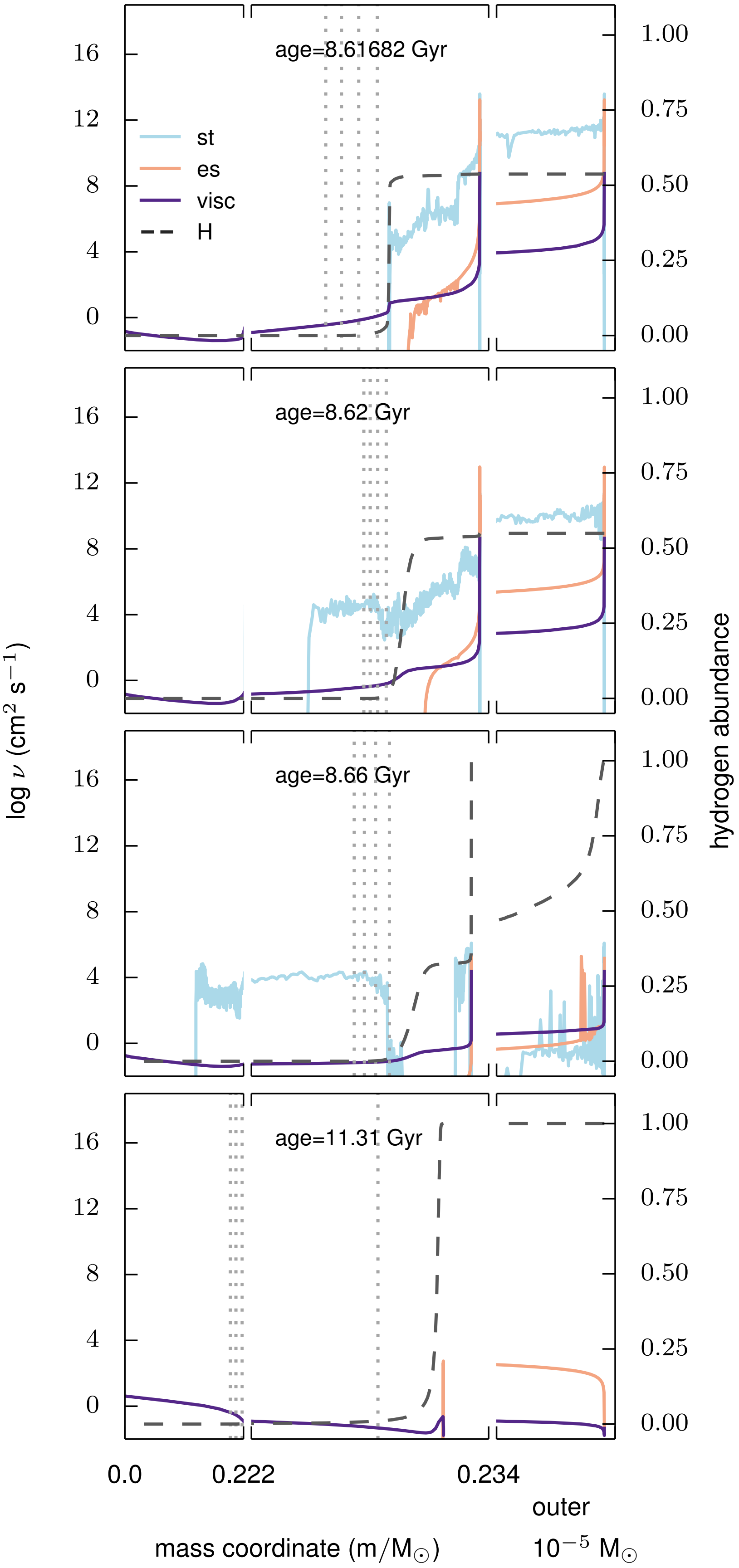

Figure 4.8: Angular momentum diffusion coefficient, ν as function of mass coordinate from the centre (left) to the surface of the star (right) for the same proto-WD as in Fig. 4.7. Processes included are Spruit-Tayler dynamo (st), Eddington-Sweet circulation (es), and electron viscosity (visc). Each panel (from top to bottom) corresponds to a profile as marked by the black arrows in Fig. 4.7 (from left to right). The grey dotted lines define lines of constant hydrogen abundance, from 10^{-5} to 10^{-2}, while the black dashed line represents the hydrogen mass abundance.

coefficient, ν are shown at four different times. As depicted in the first panel, there is a very steep H-gradient immediately after a flash (and also after detachment from the LMXB phase) that completely prevents mixing to the core. As burning proceeds between flashes (second and third panels in Fig. 4.8), the H-gradient is softened and starts to move outwards in mass, which allows some angular momentum to be transported to the core mainly through magnetic torques from the Spruit-Tayler dynamo. Finally, after settling on the cooling track (final panels panel in Figs. 4.7 and 4.8), most of the remaining hydrogen has been burnt, and angular momentum has mixed efficiently between the envelope and the core. Despite the small mass of the envelope relative to the total WD mass, this results in the WD having a spin period more than four times shorter (i.e. faster) than its orbital period.

Because we have assumed that magnetic torques do not contribute to the mixing of elements, rotational mixing in our models barely affects the formation of the hydrogen tail due to element diffusion, and thus has a weak effect on the strength and the occurrence of flashes. At the surface, however, the fast rotation induces element mixing through Eddington-Sweet circulation (see Fig. 4.8), which counteracts the rapid settling of elements heavier than hydrogen.

4.4.2 Effect of metallicity

For a given stellar mass, decreasing the metallicity produces a decrease in the radiative opacity which has an impact on the stellar evolution. The ZAMS and the RGB-phase are shifted towards the blue region of the HR-diagram, with the luminosity and effective temperature being higher during these phases than for models at solar metallicity. In other words, at low metallicity stars tend to be hotter, have smaller radii, and evolve more quickly than their high-metallicity counterparts. An immediate consequence of lower metallicities is therefore a higher mass of the helium WD formed through the LMXB phase at a given initial orbital period because the Roche lobe is filled at a more advanced stage in the evolution as a result of the smaller radius.

As previously demonstrated by Serenelli et al. (2002b) and Nelson et al. (2004), the threshold mass for the occurrence of hydrogen shell flashes increases with lower metallicity. This is confirmed by our calculations, as shown in Table 4.2. For example, for the basic models (without diffusion and rotation), the minimum mass above which the flashes occur is $\sim 0.21\ M_\odot$ for $Z = 0.02$, $\sim 0.22\ M_\odot$ for $Z = 0.01$, $\sim 0.25\ M_\odot$ for $Z = 0.001$, and $\sim 0.28\ M_\odot$ for $Z = 0.0002$.

Models with element diffusion have lower threshold values for flashes to occur, with the following dependence on metallicity: all the models studied for $Z = 0.02$ experience flashes, the lowest mass proto-WD produced being $0.167\ M_\odot$. For $Z = 0.01$ flashes occur above $0.169\ M_\odot$, for $Z = 0.001$ the limit is $\sim 0.22\ M_\odot$, while for $Z = 0.0002$ the lower threshold value is $\sim 0.26\ M_\odot$. When rotational mixing is included, all the threshold values are slightly higher than only diffusion is included, cf. Table 4.2. The upper limit for the occurrence of flashes is not as well constrained because fewer models are calculated models in this mass range, given that the focus of this work is towards the lowest masses of helium WDs, which are the ELM WDs. The obtained limits for hydrogen shell flashes agree well with those found in the literature for low metallicity (Serenelli et al. 2001), but at solar metallicity we obtain somewhat lower values than Althaus et al. (2013).

The change in metallicity not only affects the threshold for flashes, but also the extent of the loops in the HR diagram. In Fig. 4.9 the formation and evolution of a proto-WD with a mass of $\sim 0.28\ M_\odot$ is shown in the HR-diagram for all the investigated metallicities. The lower the metal content, the weaker the CNO burning, and thus the loops during the CNO flashes are markedly less extended than in models with higher metallicity. Moreover, the number of flashes increases with decreasing metallicity: while the models for $Z = 0.02$ and $Z = 0.01$ experience just one hydrogen shell flash, the model at $Z = 0.001$ goes through two flashes, and at $Z = 0.0002$ the star experiences three hydrogen shell flashes. The

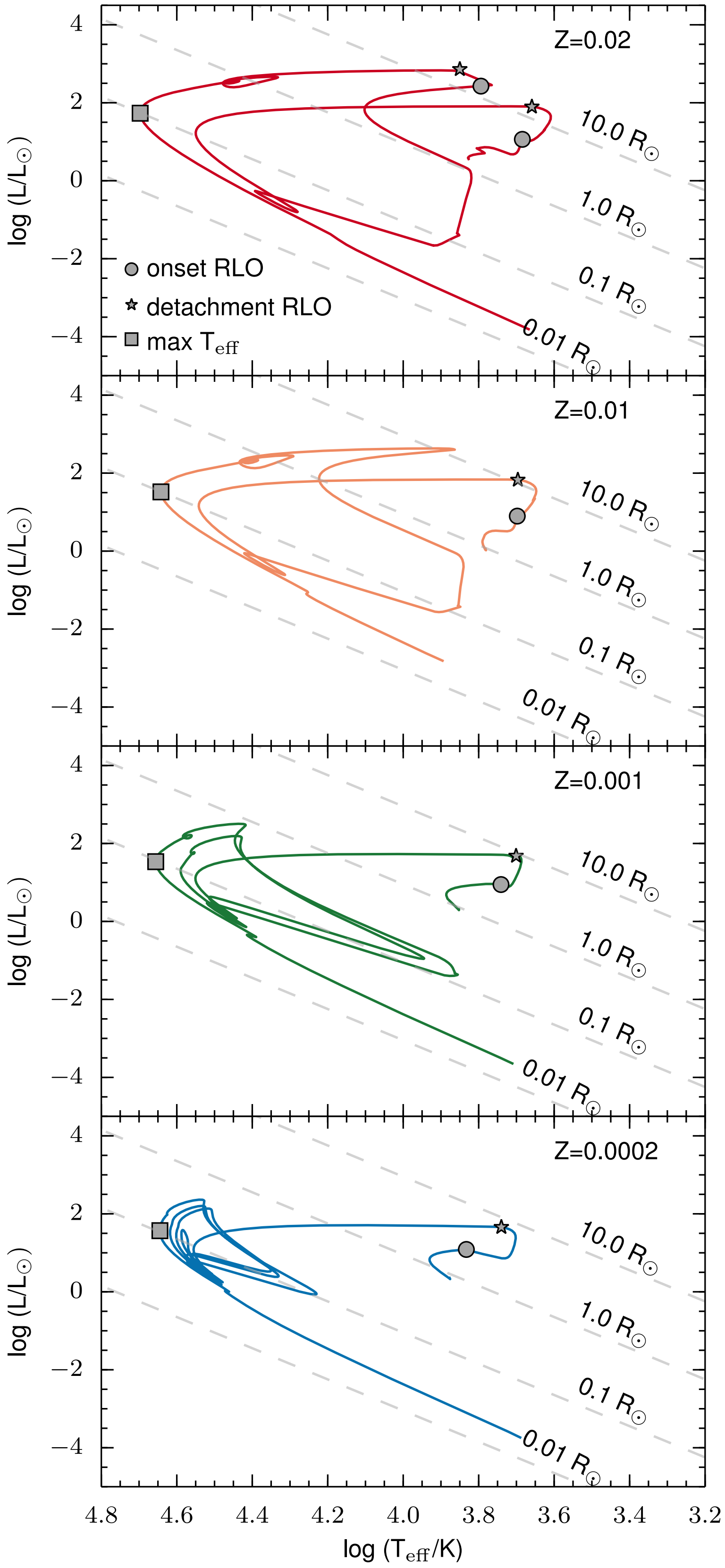

Figure 4.9: HR-diagram showing the formation and evolution of a ∼ 0.28 $M_\odot$ WD from progenitors with different metallicities. The grey symbols represent the beginning of RLO (circles), the end of RLO (stars) and the maximum $T_{\rm eff}$ (squares). The grey dashed lines represent lines of constant radius.

Table 4.2: Proto-WD mass ranges for hydrogen shell flashes. For a given model category and a given metallicity, the threshold mass for flashes also depends on the initial mass of the donor star.

Z	category	$M_{\rm flash,min}$ ($M_\odot$)	$M_{\rm flash,max}$ ($M_\odot$)
0.02	basic	0.212	0.305−0.319
0.02	diffusion	<0.167	>0.392
0.02	diffusion+rotation	<0.167	>0.321
0.01	basic	0.222	0.305−0.375
0.01	diffusion	0.167	>0.291
0.01	diffusion+rotation	<0.181	>0.32
0.001	basic	0.249	0.349−0.422
0.001	diffusion	0.223	>0.322
0.001	diffusion+rotation	0.232	>0.32
0.0002	basic	0.282	0.356−0.441
0.0002	diffusion	0.266	>0.311
0.0002	diffusion+rotation	0.275	>0.292

interval of masses for which flashes occur is also affected by metallicity. For $Z = 0.02$ and $Z = 0.01$, a 0.28 $M_\odot$ helium WD is close to the upper mass limit where hydrogen shell flashes occur, while for $Z = 0.001$ and $Z = 0.0002$, a 0.28 $M_\odot$ helium WD is located close to the lower mass limit of the hydrogen shell flash interval. We stress that the number of flashes decreases with increasing mass of the WD and varies between 0 and 7 flashes for our computed models (see Appendix B).

4.4.3 Inheritance of proto-WDs: the hydrogen envelope mass

Figure 4.10 shows the hydrogen envelope mass at the end of the mass-transfer phase (Roche-lobe detachment), $M_{\rm H,det}$, as a function of the proto-WD mass for all the computed models. For a given metallicity, the models with diffusion and with diffusion+rotation have very similar values of $M_{\rm H,det}$ as the basic models. The general trend is that the lower the mass of the proto-WD, the higher $M_{\rm H,det}$. The features in $M_{\rm H,det}$ are given by the evolutionary history of the progenitor (donor) star and depend on the point in its evolution at which mass transfer is initiated. We note a jump in the hydrogen envelope mass at $\sim 0.21\ M_\odot$, $\sim 0.23\ M_\odot$, $\sim 0.29\ M_\odot$, and $\sim 0.34\ M_\odot$ for $Z = 0.02$, $Z = 0.01$, $Z = 0.001$, and $Z = 0.0002$, respectively. This can be understood as discussed below. The shell hydrogen burning produces a convective envelope. When the convective envelope reaches its deepest extent, a hydrogen abundance gradient is produced between the region of the star mixed by the convective envelope and the layers below (which are rich in helium). When the hydrogen burning shell passes through this chemical discontinuity, the hydrogen burning rate drops, the radius contracts on a Kelvin-Helmholtz timescale and, as a result, the mass transfer will cease. The same phenomenon is responsible for the occurrence of the luminosity bump in red-giant stars (e.g. Thomas 1967; Christensen-Dalsgaard 2015), first discussed in the context of temporary Roche-lobe detachment in LMXBs in Tauris & Savonije (1999).

The interruption of the mass transfer can be a temporary effect if the envelope is massive enough, such that when the burning shell has passed through the discontinuity, the star still has enough material to burn and can therefore resume its mass transfer. If its envelope has been stripped to a greater extent, then the donor star is unable to resume mass transfer and a proto-WD is formed. This discontinuity in $M_{\rm H,det}$, observed at all the metallicities studied, distinguishes the systems that undergo this type of temporary detachment (the systems on the right-hand or upper side of the discontinuity) from the systems in which the hydrogen shell burning passes through the hydrogen abundance discontinuity without being able to resume mass transfer afterwards (the systems on the left-hand or lower side of the discontinuity). This explains the increasing values of $M_{\mathrm{H,det}}$ with $M_{\mathrm{proto-WD}}$ just below the discontinuity.

4.4.4 $\Delta t_{\mathrm{proto}}$: the contraction timescale for proto-WDs

As has been discussed earlier in this work, after the end of the LMXB mass-transfer phase, a certain amount of time, $\Delta t_{\mathrm{proto}}$, is required by the newly formed object, the proto-WD, to contract and reach its cooling track. This timescale, from Roche-lobe detachment to the beginning of the cooling track (defined as when T_{eff} reaches its maximum value), depends on the mass of the proto-WD and can reach up to 2 Gyr for the lowest mass proto-WDs (Istrate et al. 2014b) down to 10 – 100 Myr for the highest mass helium WDs. More importantly, Istrate et al. (2014b) have shown that $\Delta t_{\mathrm{proto}}$ is not influenced by the occurrence of hydrogen shell flashes, and consequently, the suggested dichotomy in WD cooling times produced by hydrogen flashes was called into question.

The determination of $\Delta t_{\mathrm{proto}}$ is important, especially for determining the age of MSPs with helium WD companions independently of the spin-down of the MSP (e.g. van Kerkwijk et al. 2005; Antoniadis et al. 2012; Bassa et al. 2016). During this phase, the proto-WD appears to be bloated, meaning that its radius is significantly larger than the radius of a cold WD of similar mass. As the timescale for this contraction phase ($\Delta t_{\mathrm{proto}}$) is predicted to be relatively long, a number of ELM WDs should be observed in this bloated stage. One example suggested by Istrate et al. (2014b) is PSR J1816+4510, based on observations by Kaplan et al. (2012, 2013).

Figure 4.11 shows $\Delta t_{\mathrm{proto}}$ for all our computed models. One feature is the occurrence of clustering in the data that groups the proto-WDs that undergo the same number of flashes (see Appendix B). As discussed before, the models with diffusion only and diffusion+rotation behave in a very similar way. In general, $\Delta t_{\mathrm{proto}}$ is larger than in the basic models when diffusion is included because of the additional flashes. For $Z = 0.02$ and $Z = 0.01$ there is a smooth transition of $\Delta t_{\mathrm{proto}}$ around the limit of the occurrence of flashes (models that experienced hydrogen shell flashes are plotted with open symbols). We recall that for these high metallicities all the models with diffusion only and diffusion+rotation (except for the model with the lowest mass at $Z = 0.01$) undergo unstable burning through CNO hydrogen shell flashes. However, for $Z = 0.001$ and $Z = 0.0002$ we note a slight increase in $\Delta t_{\mathrm{proto}}$ around the lowest threshold for flashes for all models where diffusion is included.

The maximum value of T_{eff} reached during the proto-WD phase, however, is very sensitive to both the time and the spatial resolution with which the stellar structure is computed. With this in mind, and taking into account that $\Delta t_{\mathrm{proto}}$ is relatively small around the lowest threshold for flashes at these low metallicities the results shown in Fig. 4.11 do not present evidence for a dichotomy in $\Delta t_{\mathrm{proto}}$ that is due to hydrogen flashes. However, for the long-term evolution on the WD cooling track the situation is different, as we discuss below.

4.4.5 Dichotomy on ELM WD cooling tracks

The hydrogen envelope mass is an important parameter that determines the long-term cooling timescale for WDs. Following the work of Istrate et al. (2014b), we consider the beginning of the cooling track as the moment at which the proto-WD reaches its maximum value of T_{eff}. Figure 4.12 shows the remaining hydrogen envelope mass when the proto-WD reaches the maximum T_{eff} ($M_{\mathrm{H,T_{eff,max}}}$) and finally settles on the cooling track, as a function of the mass of the proto-WD. Again, the large scatter is related to the number of flashes (between 0 – 7) that the proto-WD experiences. At all metallicities we note a jump in $M_{\mathrm{H,T_{eff,max}}}$ that occurs at the lowest threshold for flashes. At low metallicities, the effect is more pronounced in models with diffusion and diffusion+rotation, whereas at Z=0.02 the discontinuity

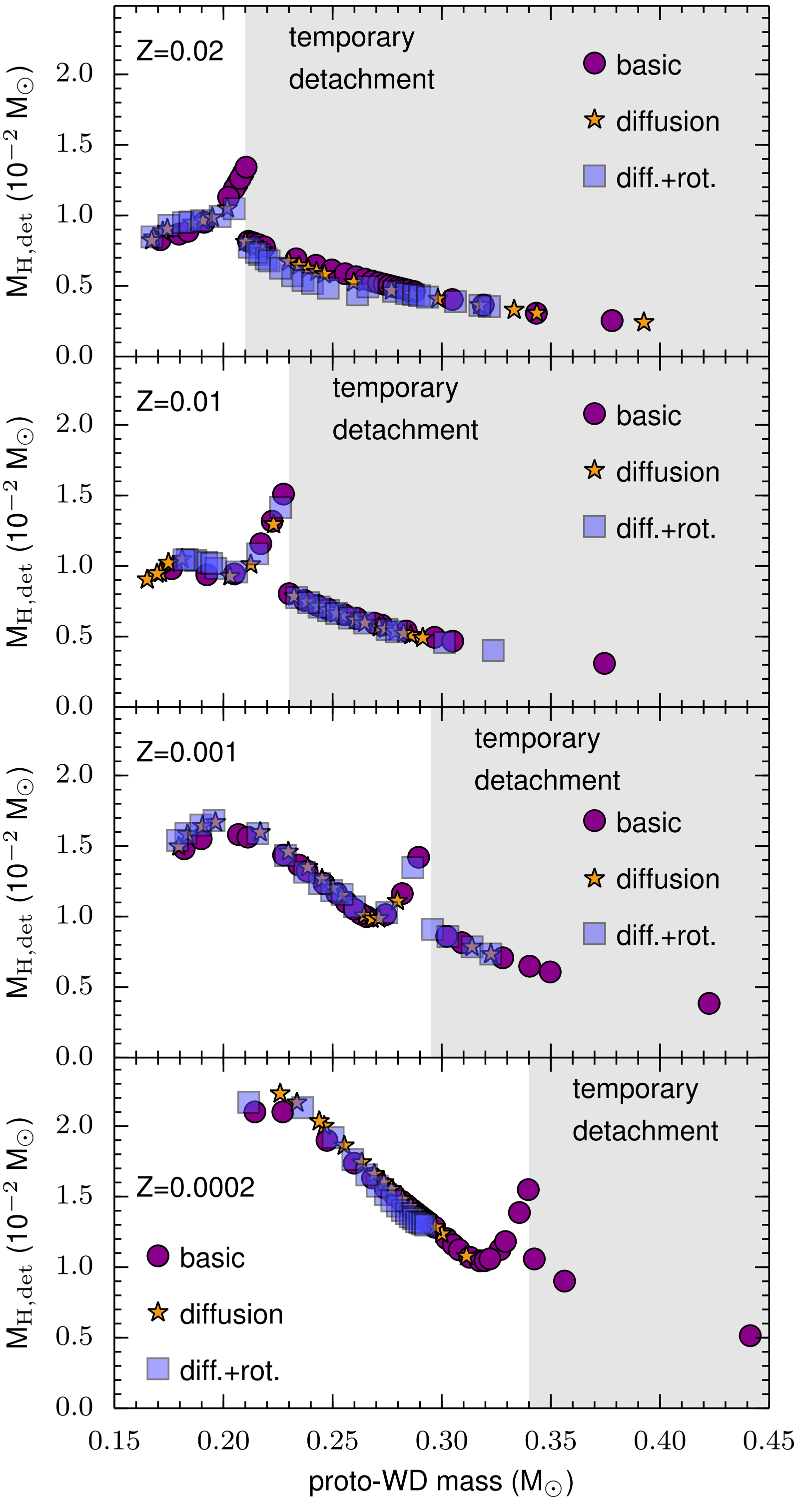

Figure 4.10: Hydrogen envelope mass at the end of the mass-transfer phase (Roche-lobe detachment) for the basic stars (purple circles), for the stars with diffusion only (orange stars) and for the stars with diffusion+rotation (blue squares) for $Z = 0.02$ (top panel), $Z = 0.01$ (second panel), $Z = 0.001$ (third panel) and $Z = 0.0002$ (bottom panel) as a function of proto-WD mass. The grey shaded area denotes the stars that undergo a temporary Roche-lobe detachment (see text for details).

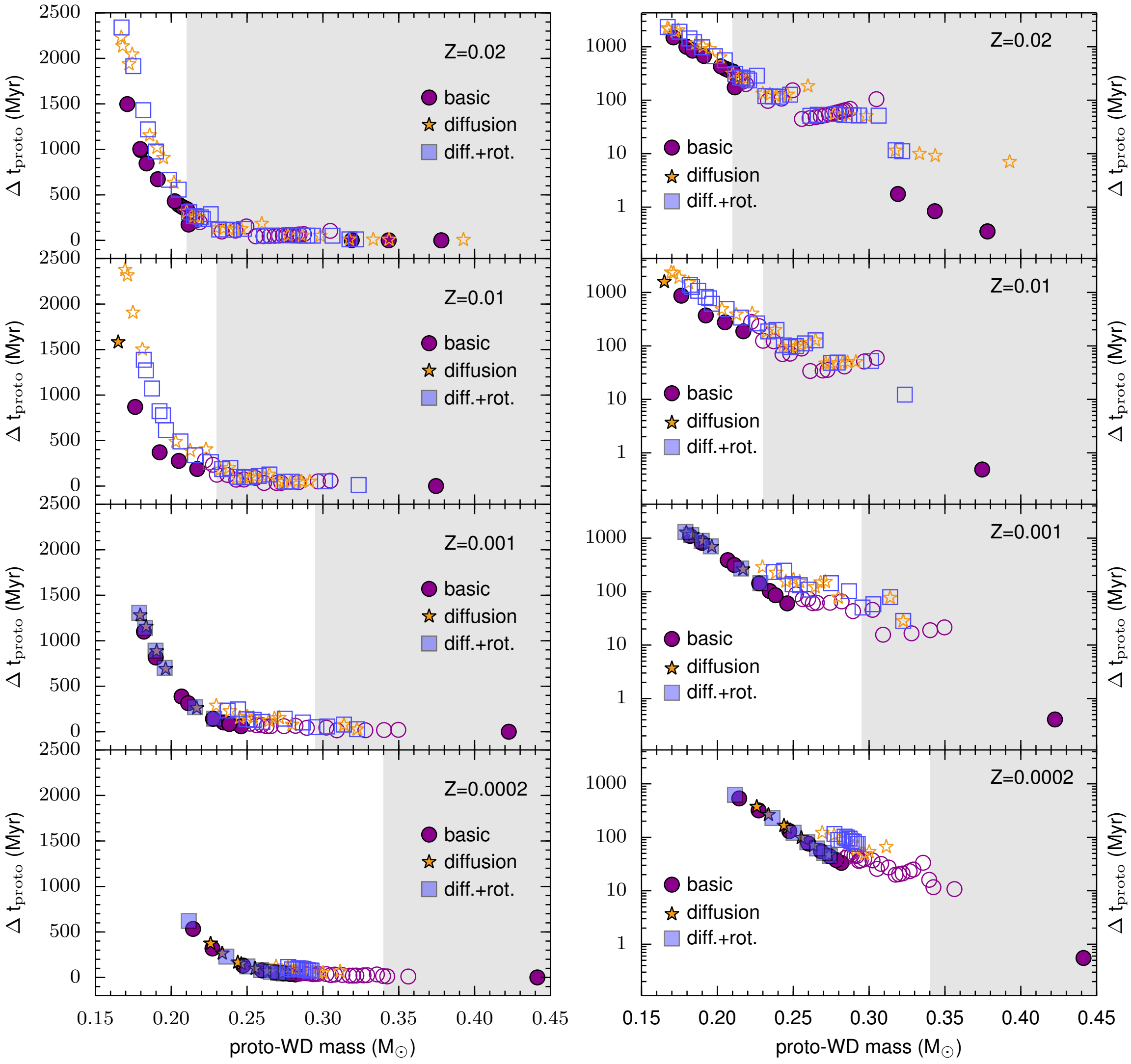

Figure 4.11: Δt_{proto} for the basic models (purple circles), for the models with diffusion only (orange stars), and for the models with diffusion+rotation (blue squares) as a function of proto-WD mass for $Z = 0.02$ (top panels), $Z = 0.01$ (second panels), $Z = 0.001$ (third panels) and $Z = 0.0002$ (bottom panels). The left-hand panels show a linear scale in Δt_{proto} while the right-hand panels show a log scale. Open symbols denote models that experience hydrogen shell flashes, whereas filled symbols denote models that avoid flashes. The grey shaded regions indicate temporary Roche-lobe detachment.

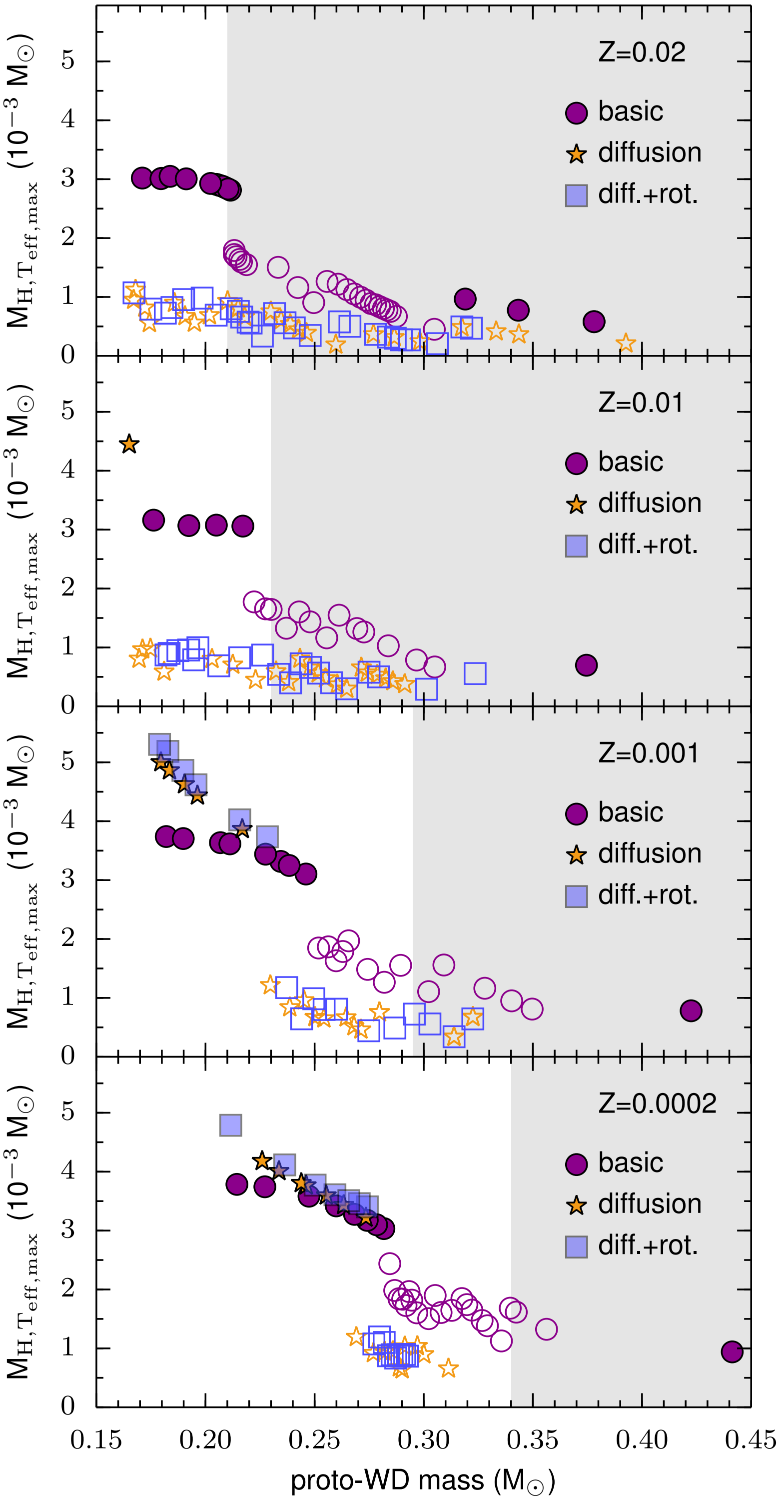

Figure 4.12: Hydrogen envelope mass at the beginning of the cooling track (maximum $T_{\rm eff}$) for the basic models (purple circles), for the models with diffusion only (orange stars) and for the models with diffusion+rotation (blue squares) as a function of proto-WD mass. See Fig. 4.11 for further explanations.

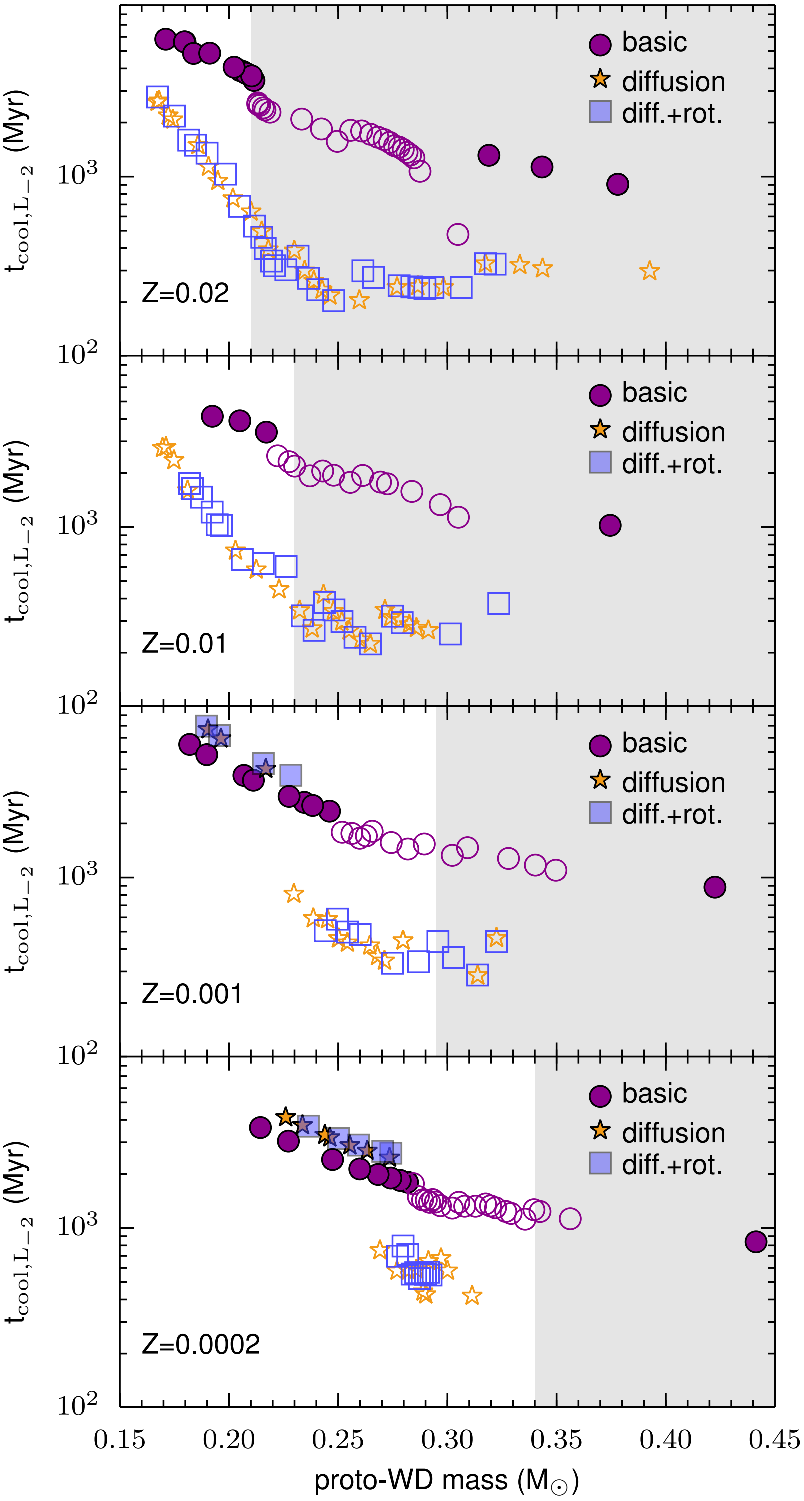

Figure 4.13: Timescale $t_{\mathrm{cool,L_{-2}}}$ (see text) for the basic models (purple circles), for the models with diffusion only (orange stars), and for the models with diffusion+rotation (blue squares) as a function of proto-WD mass. See Fig. 4.11 for further explanations.

is only seen in the basic models (all the systems for which element diffusion is considered experience hydrogen flashes). When element diffusion is included, the hydrogen envelope mass at the beginning of the cooling track is typically twice as small as when element diffusion is neglected (basic models), except for models at low metallicities and masses below the flash threshold. This significantly affects the cooling times of these objects.

For example, consider an ELM WD with a mass of $\sim 0.20\ M_{\odot}$. Figure 4.12 shows that flashes at high metallicities ($Z = 0.02$ and $Z = 0.01$) cause the amount of remaining hydrogen envelope mass at $T_{\rm eff}^{\rm max}$ ($M_{\rm H,T_{eff,max}} \sim 1.0\times 10^{-3}\ M_{\odot}$) to be up to five times smaller than for the cases with lower metallicities ($Z = 0.001$ and $Z = 0.0002$) where flashes do not develop and a thick $\sim 5.0\times 10^{-3}\ M_{\odot}$ residual hydrogen envelope remains at the onset of the cooling track. Hence, it is clear that we do see a dichotomy in the long-term cooling ages of ELM WDs, such that those proto-WDs that experience flashes will have thin hydrogen envelopes and therefore shorter cooling timescales, whereas proto-WDs that avoid flashes will have relatively thick hydrogen envelopes and cool on a much longer timescale. It is important to stress that the threshold mass at which this transition occurs is dependent on metallicity.

We now analyse the dichotomy in long-term cooling in more detail. Figure 4.13 shows the time from the end of the LMXB mass transfer until the WD luminosity reaches $\log(L/L_{\odot}) = -2.0$, $t_{\rm cool,L_{-2}}$ (including $\Delta t_{\rm proto}$). Some of our computed models are not plotted because they reached an age of 14 Gyr before $\log(L/L_{\odot}) = -2.0$. For the basic models, independent of metallicity, there is a small difference in cooling times between the WDs that experience flashes and those for which the hydrogen burning in the shell is stable. However, for the WDs computed with diffusion and diffusion+rotation, the difference in cooling times between systems with and without flashes can be as large as 3 Gyr, see Fig.4.14. We conclude that when element diffusion is included, the occurrence of hydrogen shell flashes does indeed produce a (metallicity-dependent) dichotomy in the cooling times of helium WDs.

Only when element diffusion is neglected in the modelling there is no or only a very small difference between the WDs that experience unstable hydrogen burning compared to those for which the residual hydrogen burning is stable, independent of metallicity. This can explain the findings of Istrate et al. (2014b), who evolved their stellar models without element diffusion and thus questioned the dichotomy idea.

4.5 Discussion

4.5.1 Rotational mixing: source of surface metals?

In the past few years, metals, especially calcium, were detected in the spectra of ELM WDs with a surface gravity lower than ~5.9. Metals sink below the atmosphere on a timescale much shorter than the evolutionary timescale of the proto-WD, which means that another process is required to either counteract the gravitational settling or replenish the depleted metals. There are several possible processes that can be responsible for the observed surface composition of ELM WDs. For a detailed discussion, we refer to Gianninas et al. (2014a) and Hermes et al. (2014b). For higher mass (carbon-oxygen) WDs, the presence of metals in their atmosphere is explained by accretion from circumstellar debris discs formed by tidal disruption of planetary bodies (e.g Debes & Sigurdsson 2002; Jura et al. 2007), which are detectable through excess flux in the IR (e.g Farihi et al. 2009; Kilic et al. 2006). This scenario seems unlikely for ELM WDs given that their compact orbits make the existence of a debris disk dynamically difficult to explain.

Kaplan et al. (2013) suggested that the observed metals are brought to the surface by the pulse-driven convection developed during a hydrogen shell flash. However, shortly after the convection zone vanishes, the metals will sink below the stellar surface as a result of gravitational settling.

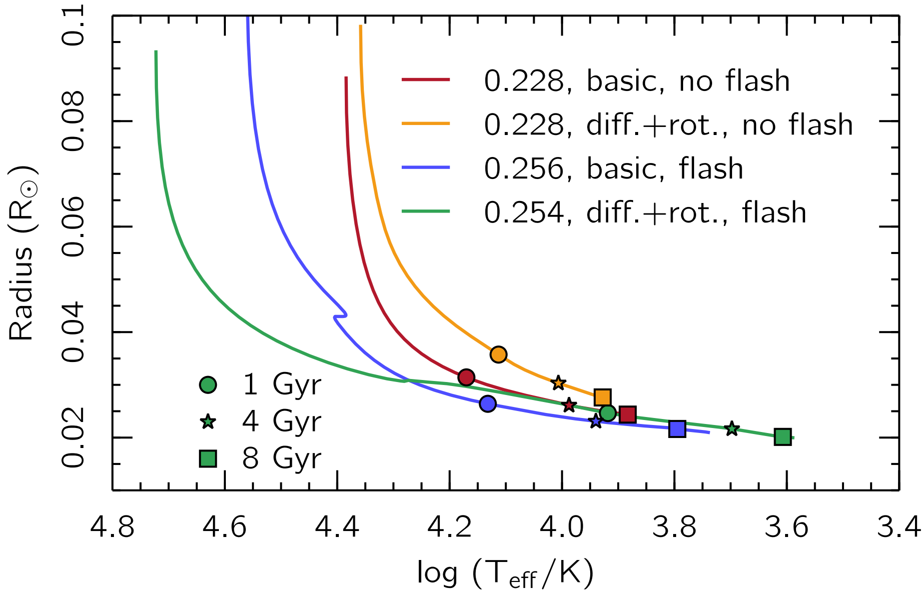

Figure 4.14: Different cooling curves illustrating the differences between basic models (without diffusion and rotation) and models that include element diffusion and rotation. All models have a metallicity of $Z = 0.001$. The value of $M_{\rm WD}/M_\odot$ is shown for each track, and the difference in masses can partly explain the different cooling rates. However, more important in this respect is the occurrence of hydrogen shell flashes (blue and green curves), which accelerates the cooling and creates a dichotomy in WD cooling ages (see text).

A mechanism that can counteract diffusion would be radiative levitation. However, as Hermes et al. (2014a) showed, radiative levitation alone cannot explain the observed abundances, especially in the case of calcium. They suggested that in addition to radiative levitation, another support mechanism such as rotational mixing is likely required to explain the observed pattern in the metal abundances of ELM WDs. Here, we discuss the effect of rotational mixing in determining the surface composition of ELM WDs.

Figure 4.15 shows the evolution of log (Ca/H) at the stellar surface from the beginning of the proto-WD phase (Roche-lobe detachment) to several hundred Myr onto the cooling track. In the model that only includes diffusion calcium sinks much faster beneath the surface than the proto-WD evolutionary timescale after the mass transfer ends. It is brought back to the surface through to the pulse-driven convection zone that is developed by the occurrence of a hydrogen shell flash, only to quickly sink again as a result of the gravitational settling. In the diffusion+rotation model, rotational mixing at the surface acts against the gravitational settling (see Sect. 4.4.1). As the proto-WD advances towards higher surface gravity, rotational mixing becomes less efficient than gravitational settling. During the proto-WD phase, the star may experience several episodes of radial expansion followed by contraction and may also develop zones of convection through the hydrogen flashes. This interplay between convection, expansion (low surface gravity), contraction (high surface gravity), and rotational mixing explains the pattern shown in Fig. 4.15. When the proto-WD enters the cooling track, the surface gravity steadily increases and gravitational settling finally overcomes the mixing that is due to rotation. As a long-term result, the metals will sink below the surface, leaving behind a pure hydrogen envelope.

We plott in Fig. 4.16 all the models with $Z = 0.02$ computed with diffusion only (left panel) and diffusion+rotation (right panel). The points are spaced at intervals of 0.5 Myr and colour-coded according to the value of log (Ca/H). Over-plotted are the data points from Gianninas et al. (2014a). The left panel

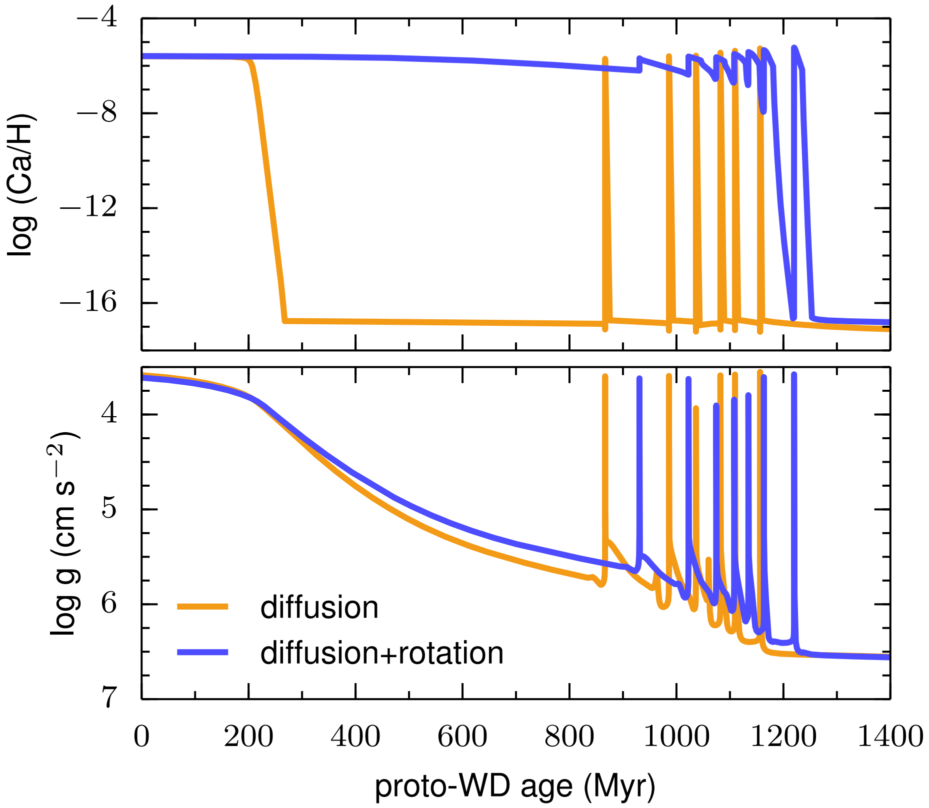

Figure 4.15: Evolution of log (Ca/H) at the stellar surface (top panel) and log g (bottom panel) for a 0.185 $M_{\odot}$ proto-WD computed with diffusion only (orange) and diffusion+rotation (blue) for Z=0.02. The starting point (t = 0) is defined at the moment of Roche-lobe detachment.

clearly shows that the flash scenario discussed above cannot explain the observations. On the other hand, when rotational mixing is included, we can qualitatively explain the presence of calcium in the spectra of proto-WDs as a natural result of their evolution. We recall that the observational data most likely belong to populations with different metallicities, while in Fig. 4.16 we only plot our models with Z = 0.02. The lack of observations of proto-WDs at high T_{eff} arises because the detection limit of Ca lines depends on the effective temperature (see Fig. 9 in Gianninas et al. (2014a)).

4.5.2 Comparison with previous work

As discussed in Gianninas et al. (2015) and Bours et al. (2015), the models of Istrate et al. (2014b) (from here on I14) and Althaus et al. (2013)(A13) show a relatively large discrepancy in their cooling ages. Although the initial binary parameters, and to some extent the metallicities, are different in the two sets of models, the main difference is that the models of A13 include element diffusion, which has an important role in reducing the hydrogen envelope mass through flashes (cf. Sect. 4.4.5), and thus consequently leads to accelerated cooling and therefore younger cooling ages than in I14 models.

Here, we compare our new models including element diffusion (but without rotational mixing to enable comparison) (I16) with the A13 models. We also adopted the same initial binary parameters, namely a 1.0 $M_{\odot}$ donor star and a 1.4 $M_{\odot}$ neutron star accretor, and also applied the same metallicity of Z = 0.01. A13 found that the lower mass limit for which hydrogen shell flashes occur is somewhere in

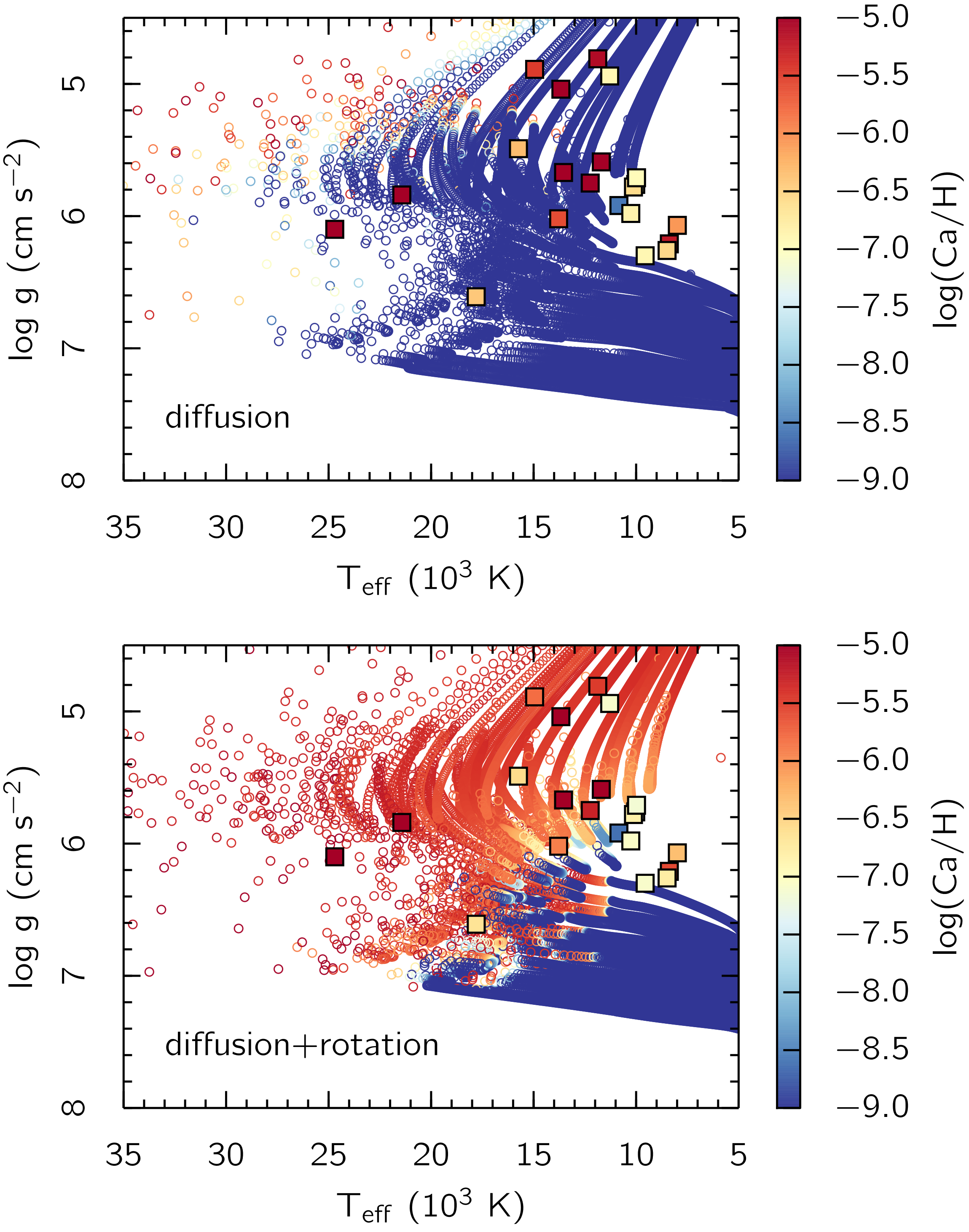

Figure 4.16: Surface gravity versus effective temperature for the models with diffusion only (a), and diffusion+rotation (b), both calculated for a metallicity of $Z = 0.02$. Each evolutionary track is plotted as a dot at 0.5 Myr intervals and colour-coded according to the value of log (Ca/H) at the stellar surface. The over-plotted squares are the observed (proto)WDs with measured Ca abundances taken from Gianninas et al. (2014a).

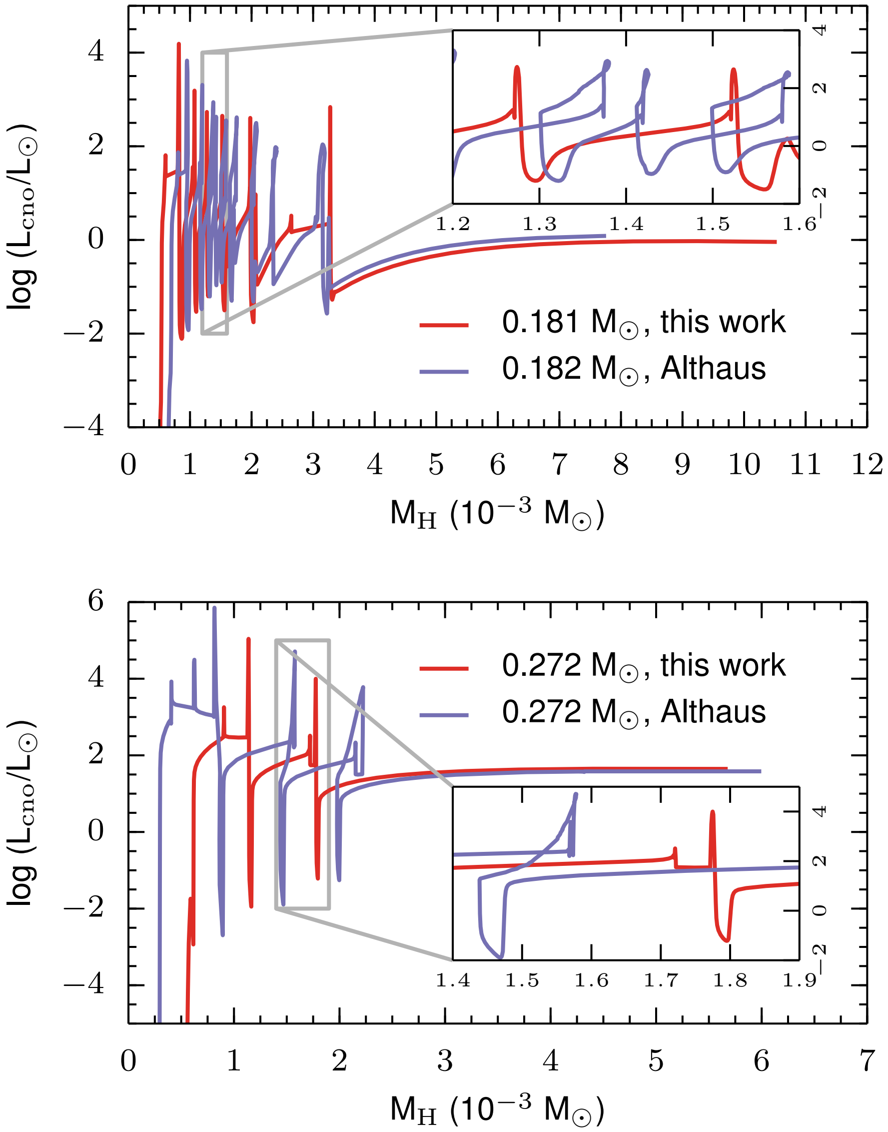

Figure 4.17: Comparison of evolutionary tracks of Althaus et al. (2013) and this work (including diffusion only) for a ~0.18 $M_{\odot}$ WD (a) and ~0.27 $M_{\odot}$ WD (b). The post-RLO evolution of luminosity, given by CNO burning, is plotted as a function of the hydrogen envelope mass. Time goes from right to left. The inset shows an artefact of hydrogen production during the shell flashes in the Althaus et al. (2013) models, see text.

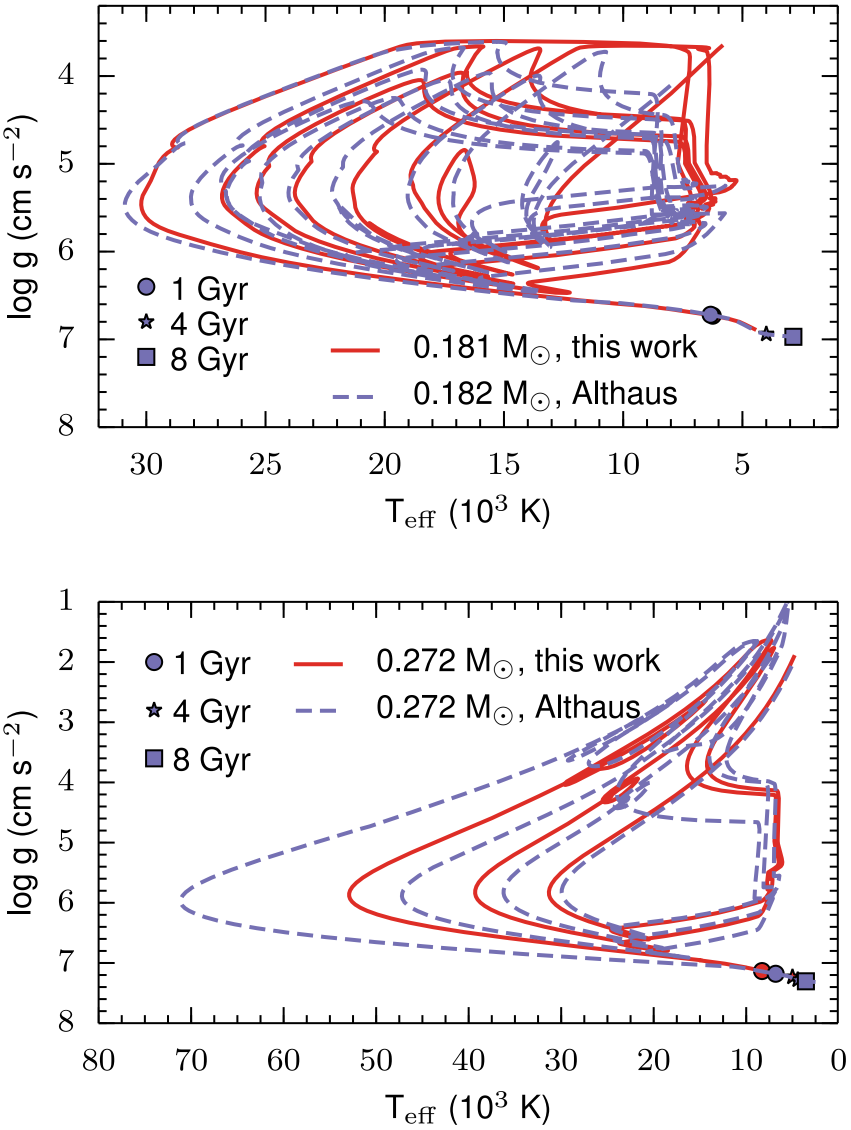

Figure 4.18: Evolutionary tracks in the ($T_{\rm eff}, \log g$)–diagram for the same models as in Fig. 4.17. The circles, stars, and squares indicate cooling ages of 1, 4, and 8 Gyr, respectively. For the 0.18 M$_\odot$ WD, the 1 Gyr symbols for the two models almost coincide. Moreover, we note that the models from this work are only calculated to an age of 14 Gyr, which prevents cooling ages exceeding 3 Gyr for the 0.18 M$_\odot$ model and 6 Gyr for the 0.27 M$_\odot$ model.

the interval $0.176 - 0.182\ M_{\odot}$ (i.e. between the last model with stable shell burning and the first model that experiences flashes), while we find a lower mass limit of $0.165 - 0.169\ M_{\odot}$.

Figure 4.17 compares the I16 models with those of A13 by showing the evolution of luminosity produced by CNO burning as a function of hydrogen envelope mass for a $\sim 0.18\ M_{\odot}$ and a $\sim 0.27\ M_{\odot}$ (proto) helium WD. One important difference is the hydrogen envelope mass left at Roche-lobe detachment. For the $0.18\ M_{\odot}$ WD, the model of I16 initially has a more massive hydrogen envelope, while for the $0.27\ M_{\odot}$ WD it is the opposite. We mention again that in our models diffusion acts from the ZAMS, in contrast with the A13 models, where diffusion is turned on during the proto-WD evolution. Figure 4.17 also shows that the A13 models contain a numerical artefact by which hydrogen is created during CNO burning (see inset).

In Fig. 4.18 we present a $(T_{\rm eff}, \log g)$–diagram and compare the evolutionary tracks from Fig. 4.17. The main difference are additional mass-transfer episodes in the I16 models as a result of a few vigorous flashes. This effect will in the end leave a slightly lower WD mass at the beginning of the cooling track. These differences in proto-WD evolution, combined with the artificial creation of hydrogen in the A13 models, result in slight differences on the cooling track. However, the difference between the A13 models and the I16 models are significantly smaller than when comparing the A13 models with the I14 models (Gianninas et al. 2015; Bours et al. 2015).

4.5.3 Relation of mass to orbital period in WDs

When low-mass stars ($< 2.3\ M_{\odot}$) reach the red-giant branch, the radius of the star mainly depends on the mass of the degenerate helium core and is almost entirely independent of the mass of the envelope (Refsdal & Weigert 1971; Webbink et al. 1983). For the formation of binary MSPs, this relation proves to be very important because it provides a correlation between the mass of the newly formed WD and $P_{\rm orb}$ following the mass transfer episode (Savonije 1987; Joss et al. 1987; Rappaport et al. 1995; Tauris & Savonije 1999; Nelson et al. 2004; De Vito & Benvenuto 2010; Lin et al. 2011; Shao & Li 2012; Jia & Li 2014; Istrate et al. 2014a).

Figure 4.19 shows the $(M_{\rm WD}, P_{\rm orb})$-relation for all the models computed in this work. Our results are in fine agreement with Tauris & Savonije (1999) for systems with $P_{\rm orb} > 1 - 2$ days. For close-orbit systems with $P_{\rm orb} < 1$ day our results agree well with Lin et al. (2011) and Istrate et al. (2014a). We note a slight discontinuity in the relation, which is dependent on metallicity as discussed in Sect. 4.4.3. This weak break in the $(M_{\rm WD}, P_{\rm orb})$-relation was previously reported by other authors (e.g. Nelson et al. 2004; Jia & Li 2014).

4.6 Conclusions

We computed a grid of models for ELM WDs with different metallicities. For each metallicity, we computed three types of models with different physics included: i) basic models (with no element diffusion nor rotation), ii) diffusion (including element diffusion), and iii) diffusion+rotation. For the first time, we took into account the combined effects of rotational mixing and element diffusion in the evolution of WD progenitors and during the proto-WD phase and WD cooling. The main results obtained are summarized as follows:

(i) We confirm that element diffusion plays a significant role in the evolution of proto-WDs that experience hydrogen shell flashes. We also confirm that the unstable burning is triggered by the diffusive hydrogen tail reaching the hot deep layers inside the star (Althaus et al. 2001a). The formation

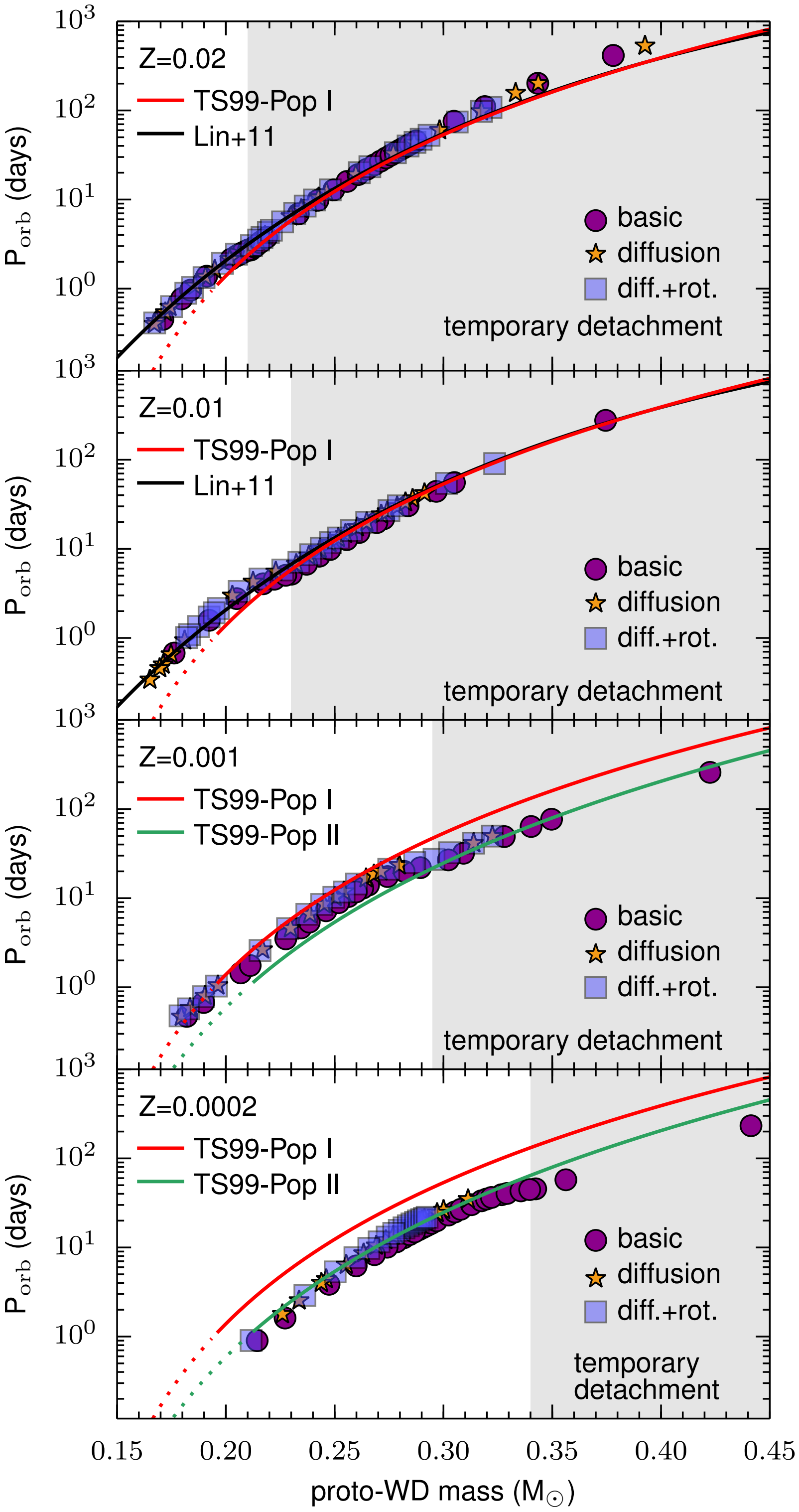

Figure 4.19: $(M_{\mathrm{WD}}, P_{\mathrm{orb}})$-relation for $Z = 0.02$ (top panel), $Z = 0.01$ (second panel), $Z = 0.001$ (third panel), and $Z = 0.0002$ (bottom panel). The grey shaded area denotes the LMXB systems that undergo a temporary detachment (see text). The purple circles represent the basic models, the orange stars the models with diffusion only and the blue squares the models with diffusion+rotation. Over-plotted are the theoretical relations by Tauris & Savonije (1999) and Lin et al. (2011) for the respective metallicity.

of the hydrogen tail is a cyclic process and depends on the available hydrogen in the envelope. Consequently, the number of flashes experienced by a proto-WD of a given mass is increased, leading to reduced hydrogen envelope mass and subsequent accelerated cooling, compared with the models without element diffusion.

(ii) Rotational mixing counteracts the effect of gravitational settling in the surface layers of young bloated ELM proto-WDs, but its efficiency is reduced towards the end of the proto-WD phase, when the star contracts and its surface gravity increases. As a consequence, our new evolutionary models including rotational mixing predict that ELM proto-WDs have mixed H/He envelopes during a significant part of their evolution before settling on the cooling track, in accordance with recent observational evidence from pulsations in ELM proto-WDs (Gianninas et al. 2016). Except for this, the general properties, such as the number of flashes, are not strongly influenced by the presence of rotational mixing.

(iii) Although the hydrogen envelope left after detachment from the LMXB phase is a small fraction of the total WD mass, it has a very high angular momentum content compared to the core. Because the proto-WD contracts while this hydrogen is burnt and angular momentum mixes inwards following each flash, the resulting WD on the cooling track is spun up significantly to a rotation period well below the orbital period.

(iv) The hydrogen envelope mass in newborn proto-WDs is influenced by the evolutionary stage of the donor star at the moment when LMXB mass transfer is initiated. In particular, we found that LMXB donor stars that experience a temporary contraction will produce proto-WDs with a significantly reduced hydrogen envelope mass at the moment of the final Roche-lobe detachment. In general, the shorter the orbital period at the onset of the LMXB phase, the lower the mass of the proto-WD and the higher the final envelope mass. The hydrogen envelope mass is also metallicity dependent, such that (for the same proto-WD mass) the lower the metallicity, the higher the envelope mass.

(v) In general, our resulting mass range for the occurrence of flashes is similar to those found in the literature. For $Z = 0.02$, all our models with diffusion experience flashes, and for $Z = 0.01$ we obtain a lower limit of $\sim 0.16\ M_\odot$, compared to $\sim 0.18\ M_\odot$ found by Althaus et al. (2013).

(vi) We identified two timescales relevant for understanding the evolution of (proto) WDs. The evolutionary timescale of the contraction of proto-WDs, Δt_proto, can reach up to 2.5 Gyr for the lowest proto-WD masses, while for the higher WD masses it is < 100 Myr. When element diffusion is included, this timescale is slightly increased by more numerous flashes than for the case when element diffusion is neglected. As concluded in Istrate et al. (2014b), we did not find a dichotomy in the Δt_proto distribution with respect to the occurrence of flashes, but rather a smooth transition. However, we note a small increase in Δt_proto close to the flash limit for $Z = 0.001$ and $Z = 0.002$. The cooling timescale $t_{\mathrm{cool,L}_{-2}}$ describes the evolution of the WD from LMXB detachment until the WD has evolved well down the cooling track and reaches $\log\ (L/L_\odot) = -2$. This timescale is mostly determined by the hydrogen envelope mass that remains after the proto-WD phase. In the basic models (without element diffusion or rotation), independent of metallicity, there is a very small difference between the models that experience flashes and those that do not. However, we confirm, as first stated by Althaus et al. (2001a), that the situation is different when element diffusion is included, which leads to a dichotomy in the cooling timescale of ELM WDs.

(vii) We investigated whether the observed metal features in ELM proto-WDs might be linked to the internal evolution of these objects. In particular, we analysed the evolution of the surface abundance of calcium and concluded that rotational mixing is a key component for producing the observed pattern in the $(\log g, T_{\rm eff})$–diagram.

The systematic investigation presented here for the effects of thermal and chemical diffusion, gravitational settling, and rotational mixing on a wide range of LMXBs with different initial masses, orbital periods, and metallicity, leads us to conclude that theoretical models must include these aspects when they are compared to observational data of ELM WDs. Hence, with these improved models at hand, the implications are better constraints on the true ages and masses of these WDs and therefore also on the ages and masses of their companion stars, such as millisecond radio pulsars. Moreover, the grid of models we presented might be further used for astroseismology calculations to determine the pulsational behaviour of ELM proto-WDs and ELM WDs.

Acknowledgements

We thank the anonymous referee for helpful advice. A.G.I. thanks Alejandra Romero and Elvijs Matrozis for very useful discussions and BWin Technologies Ltd. for the computing cores on which the simulations in this work were performed.

CHAPTER 5

Summary and conclusions

> There is no real ending. It's just the place where you stop the story.
>
> Frank Herbert

Millisecond pulsars (MSPs) are classical pulsars that have been spun up by accreting mass and angular momentum from a binary companion, through the so-called recycling process. During the mass-transfer phase, the system can be detected as an X-ray binary. Compared to the classical rotation-powered pulsars, MSPs have shorter periods ($P_{\rm spin} < 30$ ms), smaller period derivatives, and weaker magnetic fields. Since the first MSP discovered in 1982, we know now of more than 330 MSPs, including 130 discovered in globular clusters. The majority of these are found in binaries, and even the isolated MSPs are though to have a binary origin where the former companion star was evaporated after the energetic radio MSP turned on after being recycled. The population of companions found orbiting an MSP seems to be a rather diverse one, containing objects such as Jupiter-mass planets, solar-mass main-sequence stars, bloated post-main-sequence non-degenerate companions[1], low-mass helium white dwarfs (He WDs), carbon-oxygen white dwarfs (CO WDs) and neutron stars (NSs). Recent discoveries of exotic systems such as the triple MSP system J0337+1715 (Ransom et al. 2014b) and the double pulsar J0737-3039 (Lyne et al. 2004), suggest that we are still far from having a complete picture of the evolutionary channels leading to MSP systems.

A handful of MSPs are found in very compact orbits, $P_{\rm orb} \simeq 2-9$ hr, around low-mass helium-core WDs with masses below $\sim 0.3\ M_\odot$ and surface gravities $5 < \log g < 7$, the so-called extremely low-mass white dwarfs (ELM WDs). However, this type of objects are not only detected in MSP systems – the majority of them are found in binary systems with a more massive CO WD. With over 80 such objects currently known exhibiting such rather puzzling properties, ELM WDs became a hot research topic in the last couple of years. Some of the most striking properties, such as the chemical composition of their surface layers and their pulsational behaviour shown during different evolutionary phases, call for an improvement of the theoretical evolutionary models.

In this thesis, we investigated two main problems: i) the formation of MSPs observed in compact orbits with orbital periods between $P_{\rm orb} \simeq 2-9$ hr descending from low-mass X-ray binaries (LMXBs), treated in Chapter 2, and ii) the formation of ELM WDs and their subsequent evolution, with an emphasis on the proto-WD phase, described in Chapters 3 and 4.

5.1 Millisecond pulsars in compact orbits

Regarding the formation scenario of radio MSPs in tight binaries ($P_{\rm orb} \simeq 2-9$ hr) with ELM WD companions, the following questions were addressed: (i) whether the observed systems can be reproduced

---

[1] $0.01 < M_{\rm comp}/M_\odot < 0.4$, observed in eclipsing radio MSP binaries called black-widow and redback systems.

by theoretical modelling using standard prescriptions of orbital angular momentum loss, (ii) whether our computations of the Roche-lobe detachments can match the observed orbital periods and finally (iii) whether the correlation between WD mass and orbital period is valid for systems with $P_{\rm orb} < 2$ days.

In order to answer these questions, we analysed the binary interaction in LMXB systems using BEC, a stellar evolutionary code developed by the Bonn group. LMXBs are binary systems in which a low-mass star, with an initial mass below 1.6 $M_\odot$, transfers some of its mass and angular momentum to a NS companion. The mass transfer episode will be initiated as a result of radial expansion of the donor due to its nuclear evolution or shrinkage of the orbit due to loss of orbital angular momentum via gravitational wave radiation and magnetic braking. As a consequence, the final outcome of such systems is highly dependent on the initial orbital period. In this framework, the magnetic braking mechanism is one of the most uncertain processes. The most commonly used formulation of magnetic braking in LMXB systems is based on an empirical model which was developed in early 1980s from the observed spin-down rate of low-mass stars.

In this thesis, a large grid of models for LMXBs were computed, consisting of different initial donor masses and NS masses, as well as different values for the so-called γ-index of magnetic braking. For each of these sets of parameters, we explored a range of initial orbital periods in a systematic survey, yielding a total of almost 400 models. Our work showed that the orbital properties of the observed radio MSP systems with $P_{\rm orb} \simeq 2 - 9$ hr and ELM WD companions can be reproduced for each set of these initial parameters. However, a severe fine-tuning is required for the initial orbital period in order to reproduce the observed systems. This fine-tuning issue has been reported before in the literature in the modelling of ultra-compact X-ray binaries. Based on a comparison with observational data of binary pulsars, we argue that such a fine-tuning is unlikely from a statistical point of view and that something needs to be modified or is missing in the standard input physics of LMXB modelling. We refer to this issue as the *orbital period fine-tuning problem*. Moreover, we demonstrate that the theoretically calculated ($M_{\rm WD} - P_{\rm orb}$) relation is also valid for systems with $P_{\rm orb} < 2$ days, although with a larger scatter for He WD masses between $0.15 - 0.20$ $M_\odot$ due to a dependence on the initial mass of the WD progenitors.

The reported problem of orbital fine-tuning in the modelling of radio MSPs calls for a follow-up investigation. An improvement of our model would be the use of a more realistic approach of the magnetic braking mechanism. For solar-like single stars, magnetohydrodynamic simulations recently became available in which the modelling of the magnetic braking due to magnetized stellar winds, properly includes the dependence on the strength of the magnetic field, mass–loss rate, stellar radius, surface gravity and spin rate, for both slow and fast rotators (e.g. Matt et al. 2012). On the other hand, effects such as the irradiation of the donor star by the pulsar wind and the existence of a circumbinary disk should also be included. Finally, a population synthesis study of MSPs in compact orbits is required in order to properly compare the theoretical predictions with the observed orbital period distribution.

5.2 Formation and evolution of extremely low-mass white dwarfs

In the context of ELM WDs, we focused on the thermal evolution and the contraction phase towards the WD cooling track, i.e. the proto-WD phase. The proto-WD phase is the evolutionary phase from the end of the mass transfer in a binary system until the remaining donor, i.e. the proto-WD, finally settles on its WD cooling track. A timescale is associated with this evolutionary phase, the so-called $\Delta t_{\rm proto}$. A determination of $\Delta t_{\rm proto}$ is crucial when one uses the cooling time of the WD companion to get an accurate independent estimate of the age of a MSP system. The reason is that $\Delta t_{\rm proto}$ should be added to the derived cooling age to achieve the total age of the MSP since its formation via recycling. This result can be compared to the kinematic spin-down age of the MSP, whereby we can learn about the spin evolution of the MSP. The proto-WD phase is extremely important for the further cooling evolution of the WD, through processes affecting the hydrogen envelope left on top of the helium core after the binary interaction – for example, the residual nuclear burning in a hydrogen shell. As a handful of the recently observed ELM WDs appear to be found in this evolutionary stage, a detailed investigation of the proto-WD phase is required in order to understand their observed features, such as the presence of metals in their atmospheres.

During the proto-WD phase, the remaining hydrogen left after the binary detached undergoes burning in a shell surrounding the helium core. If this burning is unstable, i.e. if a runaway-type process with a CNO hydrogen flash develops, it forces the proto-WD to cross backwards in the HR–diagram while the radius is drastically increased. As a result of such hydrogen shell flashes, only a *thin* hydrogen envelope will be left on top of the helium core, in contrast to a *thick* hydrogen envelope in the case of stable hydrogen shell burning. The WD cooling timescale is determined mostly by the size its envelope. Consequently, a dichotomy is thought to be produced in the cooling of ELM WDs due to the prior evolution during the proto-WD phase, i.e. systems that experience hydrogen shell flashes will have a much faster cooling evolution compared to those that undergo stable residual burning.

In Chapter 3, we investigated in detail the proto-WD phase using the large grid of models computed in Chapter 2. We have shown that for detached low-mass proto-He WDs, $\Delta t_{\rm proto} \leq 2$ Gyr, i.e. they may spend up to 2 Gyr in the contraction phase from the Roche-lobe detachment until they reach the WD cooling track. As a result, we expect a fair number of He WDs to be present in this bloated phase, in agreement with recent observations. The value of $\Delta t_{\rm proto}$ decreases strongly with increasing mass of the proto-He WD. This can be understood from the well-known correlation between the degenerate core mass and luminosity of an evolved low-mass star. After Roche-lobe detachment, the rate at which the residual hydrogen in the envelope is consumed is directly proportional to the luminosity and thus it depends on the mass of the WD. We found $\Delta t_{\rm proto} \propto M_{\rm WD}^{-7}$. Moreover, we showed that the value of $\Delta t_{\rm proto}$ is not particularly sensitive to the occurrence or absence of flashes and thus we questioned the suggested dichotomy in the cooling times of He WDs.

The La Plata group in Argentina showed in a series of papers that element diffusion, i.e. gravitational settling and thermal and chemical diffusion, plays a significant role in the evolution of low-mass He WDs, a process which was neglected in our initial investigation. However, as pointed out by Nelson et al. (2004), element diffusion is an extremely fragile process and turbulence can mitigate its effects.

In Chapter 4, we extended our initial study on the formation and evolution of ELM WDs by taking into account element diffusion and, for the first time in the context of WDs, rotational mixing. In particular, the following topics were addressed: (i) the mass of the hydrogen envelope as a result of binary evolution, (ii) the role played by rotational mixing in the evolution of ELM proto-WDs, (iii) the influence of element diffusion and rotation on $\Delta t_{\rm proto}$ as well as on the cooling timescale, (iv) the existence of a dichotomy in the cooling ages of ELM WDs as a result of the occurrence of hydrogen shell flashes, (v) the presence of metals in the atmospheres of proto-WDs and (vi) the relation between the mass of the proto-WD and its orbital period at the end of the mass-transfer phase.

Using the publicly available binary stellar evolution code MESA, we computed more than 300 evolutionary tracks producing WDs with masses between $\sim 0.16 - 0.45\ M_\odot$. As ELM WDs have been discovered in various environments, from the Galactic disk to open and globular clusters, we took into account different initial metallicities, namely Z=0.02, 0.01, 0.001 and 0.0002. For each metallicity, we divided our models into three categories, depending on the included physics: (i) basic models (with no diffusion and no rotation), (ii) diffusion models (with element diffusion only) and (iii) rotation models (with both element diffusion and rotation), and systematically compared their properties. The initial rotational velocity of the donor star was set by requiring that its spin period is synchronized with the initial orbital period. Further studies should take into account that this assumption might not hold, and investigate different initial spin periods for the main sequence star.

The hydrogen envelope mass in a newborn proto-WD is a result of binary interactions and depends on the evolutionary stage of the donor star at the moment when mass transfer is initially activated. In particular, we find that the LMXB donor stars which evolve through a so-called temporary detachment (caused by a temporary contraction of the donor star which occurs when the H-burning shell crosses the hydrogen abundance discontinuity left behind by the convective envelope, leading to a temporary cease the mass transfer) will produce proto-WDs in which the hydrogen envelope mass is significantly smaller. Although showing some spread, in general, the lower the mass of the produced proto-WD, the higher the hydrogen envelope mass. Moreover, metallicity also plays an important role, such that, for the same proto-WD mass, the lower the metallicity, the higher the envelope mass.

Our results confirm that element diffusion plays an important role on the evolution of proto-WDs which experience hydrogen shell flashes. When element diffusion is accounted for, the unstable burning is triggered by the diffusive hydrogen tail resulting from the thermal and chemical diffusion, which reaches inside the hot deep layers close to the helium core. The formation of this hydrogen tail is a cyclic process and depends on the available hydrogen in the envelope. Consequently, the number of flashes experienced by a proto-WD of a given mass is increased compared to the models without diffusion. Due to these hydrogen shell flashes, the hydrogen envelope mass will be greatly reduced and the subsequent cooling phase is accelerated. In other words, if element diffusion is included, the occurrence of hydrogen shell flashes produces a clear dichotomy in the cooling timescales of ELM WDs. Moreover, the threshold at which this dichotomy occurs is dependent on metallicity. However, the evolutionary timescale of proto-WDs, $\Delta t_{\mathrm{proto}}$, is even slightly increased due to more numerous flashes compared to the case when element diffusion is neglected – confirming our conclusion from Chapter 3 on the large value of $\Delta t_{\mathrm{proto}}$ for ELM WDs.

Rotational mixing is found to counteract the effect of gravitational settling in the surface layers of young, bloated ELM proto-WDs and therefore plays a key role for determining their surface chemical abundance. However, it does not affect the internal structure of the proto-WDs, i.e. the formation of diffusive hydrogen tails, implying that the diffusion models and the rotation models exhibit very similar evolutionary timescales. Moreover, our results suggest that the spin frequencies of the WDs resulting on the cooling track are well above their orbital frequencies. At this point, there are no accurate enough measurements of the spin period of ELM WDs, so our work calls for further dedicated observations on the rotation periods of ELM WDs to put our predictions to the test.

The new evolutionary models including element diffusion and rotational mixing presented in this thesis have a great potential for further studies on pulsations. While writing this section, three ELM proto-WDs with mixed H/He atmospheres have been discovered (Gianninas et al. 2016), showing optical variability in the range $320 - 590$ s. This range of pulsation periods is consistent with theoretical predictions of p-mode pulsations in equilibrium[2] WDs models with mixed atmospheres and a mass of $\sim 0.18\ M_{\odot}$. However, a proper analysis of realistic evolutionary models is needed. As we have shown in this thesis, rotational mixing inhibits the settling of helium in the surface layers of proto-WDs, in contrast to the pure hydrogen envelopes produced when just element diffusion is taken into account. The pulsational analysis of the models presented in this thesis is currently investigated. If rotation models can explain the existence of the ELM proto-WD pulsators, this would provide one more piece of observational evidence that, indeed, rotational mixing plays a key role in the proto-WD phase of these objects.

---

[2] For envelope models specified by fixed values of effective temperature, surface gravity, mass and a variable value of the envelope composition.

In this work, we explored the formation of ELM WDs descending from LMXB systems, with an initial mass of the main-sequence donor star of 1.1 and 1.4 $M_\odot$. It has been shown in Istrate (2015) that the hydrogen envelope mass at the end of the mass-transfer phase depends on the initial mass of the donor star. In a future study, one should extend the grid of models including element diffusion and rotational mixing for a larger range of initial donor star masses.
The surface composition of ELM proto-WDs is determined by the interplay of several processes, i.e. gravitational settling, rotational mixing and radiative levitation. Radiative levitation has been neglected in this study, due to the huge computational time required. Therefore, a future study in which element diffusion, rotational mixing as well as radiative levitation are all included is required for a quantitative analysis of the surface composition of ELM WDs.
The majority of ELM WDs are found orbiting a more massive CO WD. The models presented in this thesis, along with the evolutionary models currently available in the literature, are computed in the LMXB framework in which the accretor is a NS treated as a point mass. This assumption is probably fairly correct as various studies, including the current one, show that the mass of the NS accretor does not play a role in determining the properties of the resulting ELM WD, but only affects the final orbital period. However, evolutionary models for the formation of ELM WDs, taking into account that the accretor is another WD should be performed in the future. Such studies would push forward our understanding of the formation and evolution of the ELM WD population and would be a valuable input for binary population synthesis investigations for a direct comparison with observations.

APPENDIX **A**

Additional information regarding the proto-WD phase

A.1 Observational data and time evolution in the ($T_{\rm eff}$, $\log g$)–diagram

In Fig. A.1 we have plotted points for fixed time intervals of evolution along a number of selected tracks from Fig. 3.1. The density of points along these curves combined with the (proto) WD luminosities at these epochs can be used to evaluate the probability of detecting them. For a direct comparison with data population synthesis needs to be included to probe the distribution of WD masses. The observational data plotted in Fig. 3.1 were taken partly from the sources given in Table A.1 (primarily He WDs with MSP companions, main-sequence A-star companions, or He WDs that have been detected to show pulsations). Additional data for the plotted symbols can be found in Silvotti et al. (2012); Hermes et al. (2013b); Brown et al. (2013).

A.2 The (proto) WD contraction phase

Fig. A.2 shows the time $\Delta t_{\rm proto}$ it takes from Roche-lobe detachment until the proto-He WD reaches its highest value of $T_{\rm eff}$ and settles on the cooling track. Shown in this plot are all our calculated models for progenitor stars of 1.2 and 1.4 $M_{\odot}$ (i.e. a subset of the models plotted in Fig. 3.2). The black line (Eqn. 3.1) is an analytical result obtained from a somewhat steep core mass–luminosity function ($L \propto M_{\rm WD}^{7}$) combined with the assumption (for simplicity) that in all cases 0.01 $M_{\odot}$ of hydrogen is burned before reaching the highest $T_{\rm eff}$. The figure shows that this line also serves as a good approximate fit to our calculated models. For a given He WD mass, the fit to $\Delta t_{\rm proto}$ calculated from our models is accurate to within 50%.

A.3 Nuclear burning during flashes

To compare the burning of residual envelope hydrogen for a case with and without large thermal instabilities (hydrogen shell flashes), we have plotted tracks in the HR–diagram shown in Fig. A.3. The age of the stars and the total amount of hydrogen remaining in their envelopes are given in Table A.2 for the points marked in the figure. These models were chosen very close to (but on each side of) $M_{\rm flash} \simeq 0.21$ $M_{\odot}$, in both cases for a 1.3 $M_{\odot}$ progenitor star. As discussed in the main text, although the peak luminosity is high during a flash (and thereby the rate at which hydrogen is burned), the star only spends a relatively short time ($\sim 10^{6}$ yr) in this epoch. (For more massive He WDs it is even less time – for example, it only lasts $\sim 10^{3}$yr for a 0.27 $M_{\odot}$ He WD.) Therefore, the amount of additional hydrogen burned as a result of flashes is relatively small. In the example shown in Fig. A.3 it amounts

Table A.1: Observational data of a number of low-mass He WDs (and proto-He WDs), preferentially in tight binary systems.

He WD	$\log g$ (cm s^{-2})	$T_{\rm eff}$ (K)	$M_{\rm WD}$ ($M_\odot$)	$P_{\rm orb}$ (hr)	Optical data
PSR J0337+1715	5.82 ± 0.05	$15\,800 \pm 100$	0.197 ± 0.0002	39.12	Kaplan et al. (2014b)
PSR J0348+0432	6.035 ± 0.06	$10\,120 \pm 90$	0.172 ± 0.003	2.46	Antoniadis et al. (2013)
PSR J0751+1807	7.41 ± 0.48	$3\,900 \pm 400$	0.138 ± 0.0006[a]	6.31	Bassa et al. (2006b)
PSR J1012+5307	6.75 ± 0.07	$8\,550 \pm 25$	0.16 ± 0.02	14.51	van Kerkwijk et al. (1996); Callanan et al. (1998)
PSR J1738+0333	6.45 ± 0.07	$9\,130 \pm 150$	0.182 ± 0.016	8.52	Antoniadis et al. (2012)
PSR J1816+4510	4.9 ± 0.3	$16\,000 \pm 500$	$\sim 0.21 \pm 0.02$[b]	8.66	Kaplan et al. (2012, 2013)
PSR J1909−3744	6.77 ± 0.04	$9\,050 \pm 50$	0.2038 ± 0.0022	36.72	Antoniadis (2013)
PSR J0024−7204U[c]	~ 5.6	$\sim 11\,000$	~ 0.17	10.29	Edmonds et al. (2001)
PSR J1911−5958A[c]	6.44 ± 0.20	$10\,090 \pm 150$	0.175 ± 0.010	20.64	Bassa et al. (2006a)
NLTT 11748	6.35 ± 0.03	$7\,600 \pm 120$	0.149 ± 0.013	5.64	Kaplan et al. (2014a)
KOI−74	6.51 ± 0.14	$13\,000 \pm 1000$	0.22 ± 0.03	125.53	van Kerkwijk et al. (2010)
KOI−1224	5.75 ± 0.06	$14\,700 \pm 1000$	0.22 ± 0.02	64.75	Breton et al. (2012)
KIC 10657664	5.50 ± 0.02	$14\,600 \pm 300$	0.26 ± 0.04[d]	78.55	Carter et al. (2011)
SDSS J184037.78	6.49 ± 0.06	$9\,390 \pm 140$	~ 0.17	4.59	Hermes et al. (2013b)[e,f]
SDSS J111215.82	6.36 ± 0.06	$9\,590 \pm 140$	~ 0.17	4.14	Hermes et al. (2013b)[e,f]
SDSS J151826.68	6.90 ± 0.05	$9\,900 \pm 140$	~ 0.23	14.62	Hermes et al. (2013b)[e,f]
J1614	6.66 ± 0.14	$8\,800 \pm 170$	~ 0.19	–	Hermes et al. (2013b)[f]
J2228	6.03 ± 0.08	$7\,870 \pm 120$	~ 0.16	–	Hermes et al. (2013b)[f]

[a] D. Nice, private comm. (2014).

[b] Based on Kaplan et al. (2013). See also Istrate et al. (2014a) for further comments on the component masses of this source.

[c] The WD is most likely to have formed in this globular cluster binary given that the eccentricity is $e < 10^{-5}$, as expected from recycling.

[d] Carter et al. (2011) found two possible solutions for $M_{\rm WD}$ ($0.26\ M_\odot$ and $0.37\ M_\odot$). This WD has $P_{\rm orb} = 3.3$ days and thus we adopt the lower value of $M_{\rm WD}$ since this is agrees much better with the known ($M_{\rm WD}, P_{\rm orb}$)-correlation (see Tauris & Savonije 1999, for discussions).

[e] See additional references therein.

[f] Pulsating He WDs, see Córsico & Althaus (2014a) for recent theoretical modelling.

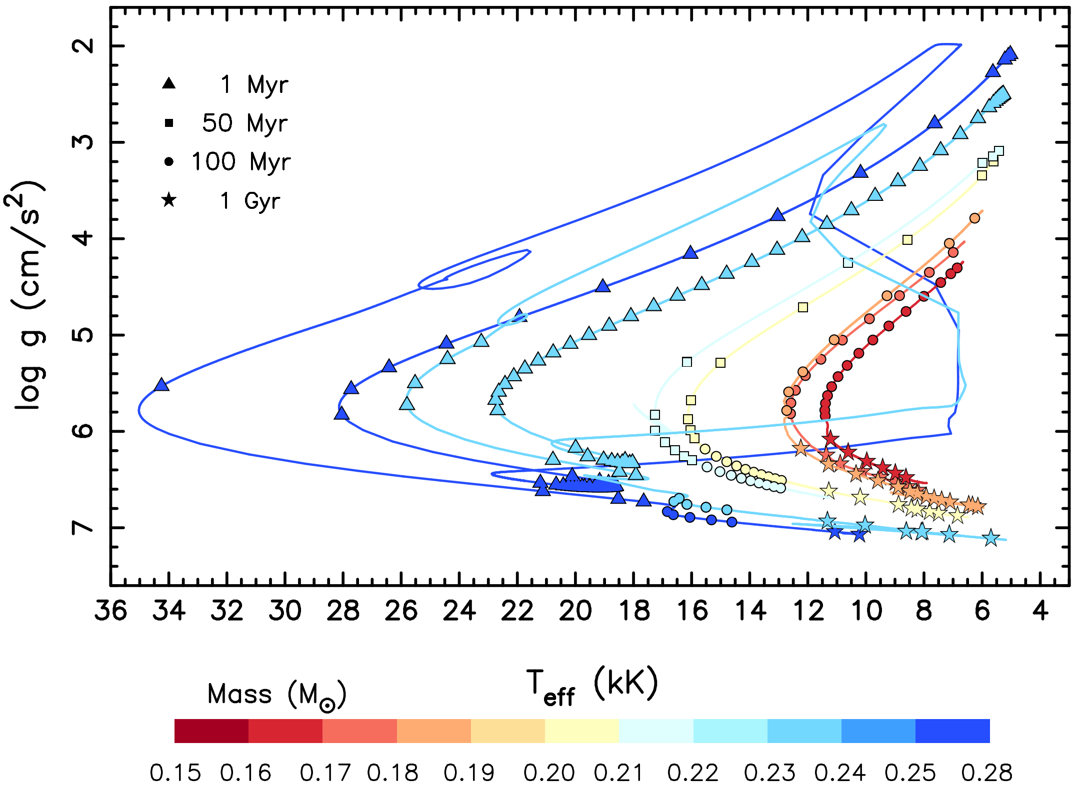

Figure A.1: Selected tracks (Fig. 3.1) with a point marked for a time interval of 1 Myr (triangle), 50 Myr (square), 100 Myr (circle), and 1 Gyr (star).

to about 12% of the total amount of hydrogen at the point of Roche-lobe detachment. Hence, the flashes may appear to reduce $\Delta t_{\mathrm{proto}}$ by ~ 100 Myr. However, one must bear in mind that the proto-WDs that experience flashes are also the WDs with the least amount of hydrogen in their envelopes after RLO.

For a star that experiences flashes, the residual hydrogen present in the envelope following the LMXB-phase is processed roughly as follows: 70% during the epoch from Roche-lobe detachment until reaching highest T_{eff}, 10% during the flashes, and 20% after finally settling on the WD cooling track.

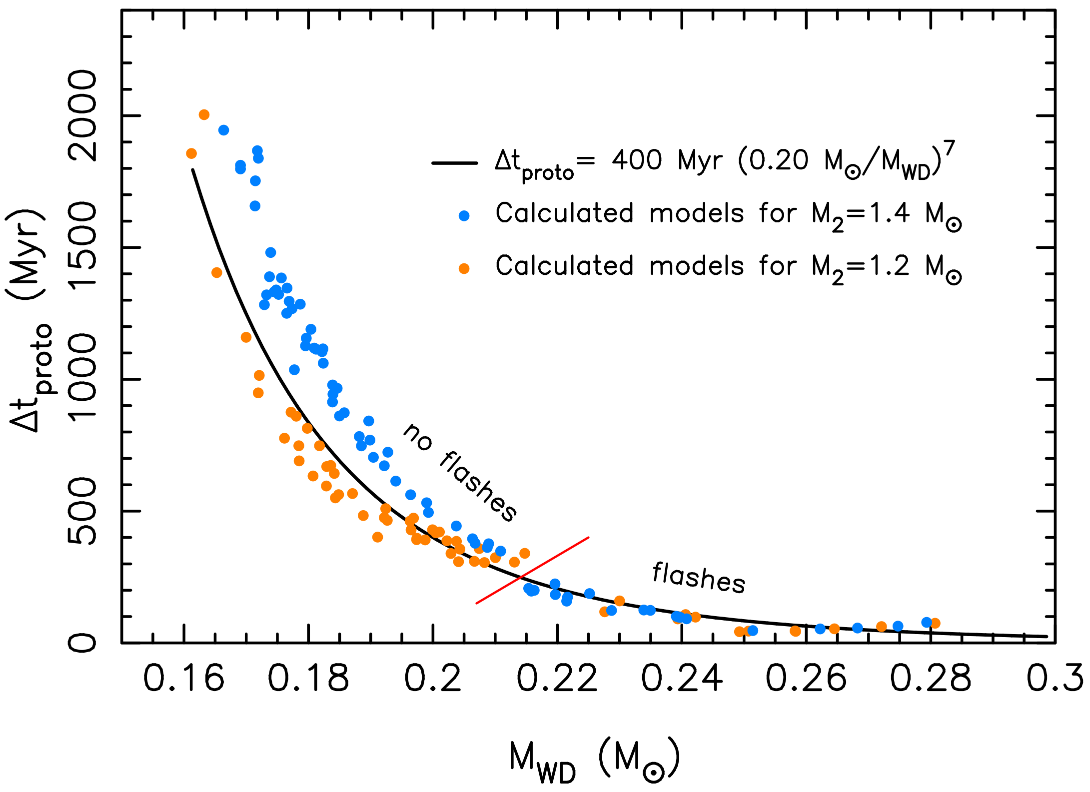

Figure A.2: Calculated models of proto-He WDs from Fig. 3.2 for M_2 = 1.2 $M_\odot$ (orange) and M_2 = 1.4 $M_\odot$ (blue). The black line is a fit to the data. It can also be derived analytically using a modified core mass–luminosity relation for low-mass evolved stars, combined with an assumed fixed amount of residual hydrogen (0.01 $M_\odot$) to be burned. The red line separates models with and without flashes.

Table A.2: Ages and remaining hydrogen of the two proto-He WDs shown in Fig. A.3. The points N1...N4 are for the non-flashing 0.212 $M_\odot$ WD model and the points F1...F9 are for the 0.221 $M_\odot$ flashing WD model.

Point	Relative age[a]	Total age[b]	Hydrogen[c] (10^{-3} $M_\odot$)
N1	0	0	13.68
N2	341 Myr	341 Myr	2.94
N3	1 900 Myr	2 240 Myr	0.79
N4	8 231 Myr	10 470 Myr	0.67
F1	0	0	7.78
F2	107 Myr	107 Myr	2.71
F3	31 Myr	138 Myr	2.45
F4	1536 yr	138 Myr	2.45
F5	5.1 Myr	143 Myr	2.22
F6	20 Myr	163 Myr	2.06
F7	1536 yr	163 Myr	2.05
F8	3.6 Myr	166 Myr	1.75
F9	2 089 Myr	2 255 Myr	0.85

[a] Age relative to the previous point along the track.
[b] Cumulated age relative to the first point on the track (since the time of Roche-lobe detachment).
[c] Total amount of hydrogen remaining in the envelope of the (proto)-He WD.

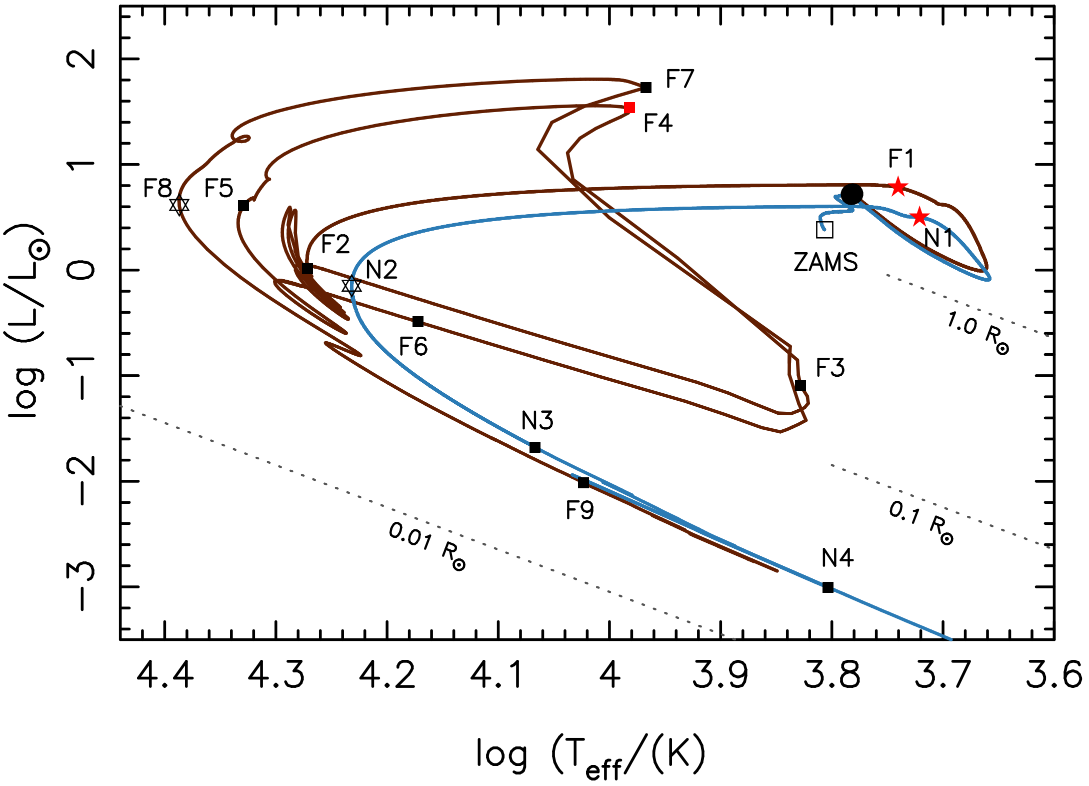

Figure A.3: Evolutionary tracks in the HR–diagram for a 0.221 $M_\odot$ proto-He WD *with* flashes (brown) and for a 0.212 $M_\odot$ proto-He WD *without* flashes (blue). See Table A.2 for data.

APPENDIX B

Properties of the computed models

Table B.1: Properties of selected models. The quantities given are (1st–7th column): the (proto) WD mass, the number of hydrogen shell flashes, the orbital period and the hydrogen envelope mass at Roche-lobe detachment, the hydrogen envelope mass at maximum $T_{\rm eff}$, $\Delta t_{\rm proto}$, and the time interval (cooling timescale) from Roche-lobe detachment until the WD reaches a luminosity of $\log(L/L_\odot) = -2$.

$Z = 0.02$, basic models (no element diffusion nor rotation)

Mass ($M_\odot$)	# flashes	$P_{\rm orb,det}$ (d)	$M_{\rm H,det}$ (10^{-2} $M_\odot$)	$M_{\rm H,T_{eff,max}}$ (10^{-3} $M_\odot$)	$\Delta t_{\rm proto}$ (Myr)	$t_{\rm cool,L_{-2}}$ (Myr)
0.171	0	0.451	0.827	3.02	1500	5820
0.180	0	0.767	0.867	3.01	1000	5630
0.180	0	0.779	0.869	3.01	993	5620
0.184	0	0.961	0.887	3.05	846	4850
0.191	0	1.38	0.952	3.01	672	4860
0.202	0	2.14	1.13	2.93	430	4060
0.205	0	2.34	1.19	2.91	392	3900
0.206	0	2.43	1.23	2.90	377	3850
0.208	0	2.53	1.26	2.88	364	3760
0.209	0	2.63	1.30	2.86	352	3690
0.210	0	2.73	1.34	2.83	342	3630
0.211	0	2.71	0.817	2.81	174	3430
0.213	3	2.94	0.808	1.72	274	2530
0.213	3	2.94	0.808	1.79	268	2570
0.214	3	3.05	0.804	1.68	261	2490
0.216	3	3.28	0.794	1.64	237	2410
0.216	3	3.40	0.790	1.59	221	2350
0.219	3	3.76	0.777	1.55	200	2280
0.233	2	6.89	0.692	1.50	97.1	2090
0.242	2	9.81	0.646	1.16	107	1840
0.250	2	12.8	0.614	0.905	153	1570
0.256	1	16.0	0.587	1.26	44.6	1810
0.261	1	19.0	0.566	1.22	46.1	1800
0.265	1	21.9	0.549	1.13	48.0	1720
0.268	1	24.5	0.534	1.05	50.1	1660
0.271	1	26.9	0.523	0.996	52.2	1610
0.274	1	29.3	0.513	0.945	54.3	1550
0.276	1	31.5	0.504	0.889	56.3	1490
0.278	1	33.7	0.496	0.868	58.2	1460
0.280	1	35.8	0.489	0.835	60.1	1410
0.282	1	37.8	0.482	0.805	61.9	1360
0.283	1	39.8	0.476	0.779	63.7	1320
0.285	1	41.7	0.470	0.755	65.4	1270
0.287	1	45.5	0.460	0.670	68.9	1070
0.305	1	75.6	0.404	0.451	105	477
0.319	0	111	0.365	0.965	1.76	1310
0.343	0	202	0.307	0.775	0.838	1130
0.378	0	414	0.255	0.581	0.351	907

Table B.2: Properties of selected models. See Table B.1 for a description of the parameters.

Z = 0.02, diffusion

Mass ($M_\odot$)	# flashes	$P_{\mathrm{orb,det}}$ (d)	$M_{\mathrm{H,det}}$ (10^{-2} $M_\odot$)	$M_{\mathrm{H,T_{eff,max}}}$ (10^{-3} $M_\odot$)	$\Delta t_{\mathrm{proto}}$ (Myr)	$t_{\mathrm{cool,L_{-2}}}$ (Myr)
0.167	24	0.401	0.823	0.951	2230	2610
0.168	26	0.431	0.843	1.12	2130	2650
0.172	12	0.541	0.885	0.818	1940	2190
0.174	10	0.623	0.904	0.557	2050	2080
0.186	6	1.08	0.948	0.899	1160	1500
0.191	6	1.35	0.963	0.674	1020	1130
0.195	6	1.63	0.984	0.563	907	945
0.202	5	2.14	1.05	0.689	636	755
0.210	4	2.72	0.811	0.930	316	638
0.215	4	3.40	0.775	0.806	264	495
0.218	5	3.89	0.753	0.662	256	392
0.230	3	6.45	0.672	0.753	134	387
0.235	3	7.79	0.644	0.606	129	299
0.239	4	9.16	0.620	0.540	121	263
0.243	3	10.6	0.600	0.448	123	234
0.246	4	12.0	0.582	0.390	128	218
0.260	3	19.0	0.526	0.191	184	205
0.277	3	32.6	0.467	0.365	54.9	242
0.286	3	43.2	0.441	0.316	52.1	246
0.298	2	60.0	0.409	0.246	50.7	242
0.317	1	97.5	0.363	0.487	11.5	328
0.333	2	157	0.331	0.416	9.96	322
0.344	2	201	0.307	0.366	9.17	308
0.393	2	532	0.242	0.211	7.03	298

Table B.3: Properties of selected models. See Table B.1 for a description of the parameters.

Z = 0.02, diffusion+rotation

Mass ($M_\odot$)	# flashes	$P_{\mathrm{orb,det}}$ (d)	$M_{\mathrm{H,det}}$ (10^{-2} $M_\odot$)	$M_{\mathrm{H,T_{eff,max}}}$ (10^{-3} $M_\odot$)	$\Delta t_{\mathrm{proto}}$ (Myr)	$t_{\mathrm{cool,L_{-2}}}$ (Myr)
0.167	23	0.412	0.848	1.07	2340	2770
0.175	10	0.628	0.929	0.794	1910	2170
0.182	8	0.886	0.948	0.725	1430	1600
0.185	7	1.03	0.954	0.821	1220	1500
0.190	6	1.33	0.963	0.956	976	1350
0.198	6	1.92	0.992	0.981	666	1030
0.205	5	2.44	1.05	0.691	558	684
0.212	4	3.03	0.775	0.801	309	531
0.215	4	3.51	0.739	0.755	266	460
0.217	5	3.76	0.723	0.659	265	398
0.220	5	4.27	0.692	0.572	253	339
0.221	4	4.53	0.678	0.557	234	319
0.226	4	5.61	0.627	0.336	288	303
0.232	3	7.01	0.572	0.719	119	361
0.236	3	8.44	0.539	0.563	117	272
0.241	3	9.88	0.517	0.476	116	234
0.248	3	12.8	0.485	0.346	127	204
0.261	3	20.0	0.438	0.578	51.1	299
0.266	3	23.4	0.494	0.502	53.4	275
0.278	3	33.6	0.463	0.365	54.8	247
0.284	2	39.9	0.446	0.319	52.8	243
0.287	2	43.8	0.438	0.299	52.7	242
0.290	2	47.4	0.431	0.274	52.3	238
0.293	2	52.6	0.421	0.273	51.8	241
0.306	2	74.2	0.389	0.208	51.4	241
0.317	1	97.6	0.363	0.491	11.6	327
0.322	1	108	0.353	0.469	11.1	326

Table B.4: Properties of selected models. See Table B.1 for a description of the parameters.

Z = 0.01, basic models (no element diffusion nor rotation)

Mass ($M_\odot$)	# flashes	$P_{\rm orb,det}$ (d)	$M_{\rm H,det}$ (10^{-2} $M_\odot$)	$M_{\rm H,T_{eff,max}}$ (10^{-3} $M_\odot$)	$\Delta t_{\rm proto}$ (Myr)	$t_{\rm cool,L_{-2}}$ (Myr)
0.176	0	0.676	0.981	3.16	869	0.00
0.192	0	1.58	0.937	3.07	371	2200
0.205	0	2.76	0.944	3.08	277	1120
0.217	0	4.05	1.16	3.06	188	3310
0.222	4	4.56	1.32	1.77	281	2460
0.228	3	5.05	1.51	1.66	234	2290
0.230	3	5.19	0.804	1.65	125	2120
0.237	2	6.71	0.756	1.33	122	1920
0.243	2	8.26	0.721	1.60	70.3	2020
0.248	2	9.82	0.694	1.43	71.6	1930
0.256	1	12.7	0.654	1.16	89.2	1740
0.261	1	15.2	0.627	1.55	33.9	1890
0.269	1	19.7	0.593	1.32	34.7	1740
0.273	1	21.7	0.581	1.26	35.6	1720
0.284	1	30.5	0.539	1.03	41.2	1540
0.297	1	44.2	0.494	0.787	51.0	1320
0.305	1	55.5	0.467	0.669	59.6	1110
0.375	0	277	0.310	0.698	0.487	1010

Table B.5: Properties of selected models. See Table B.1 for a description of the parameters.

Z = 0.01, diffusion

Mass ($M_\odot$)	# flashes	$P_{\rm orb,det}$ (d)	$M_{\rm H,det}$ (10^{-2} $M_\odot$)	$M_{\rm H,T_{eff,max}}$ (10^{-3} $M_\odot$)	$\Delta t_{\rm proto}$ (Myr)	$t_{\rm cool,L_{-2}}$ (Myr)
0.165	0	0.340	0.904	4.45	1580	0.00
0.170	7	0.458	0.946	0.807	2380	2750
0.171	5	0.501	0.950	0.967	2320	2780
0.175	5	0.651	1.02	0.980	1910	2350
0.181	7	0.937	1.05	0.589	1500	1590
0.203	6	2.97	0.927	0.804	487	731
0.212	5	4.26	1.01	0.707	390	572
0.223	5	5.53	1.30	0.448	405	447
0.232	4	6.74	0.784	0.593	183	339
0.238	4	8.33	0.745	0.411	201	268
0.240	2	8.99	0.729	1.23	130	1810
0.243	3	9.98	0.712	0.808	94.8	415
0.248	3	11.6	0.685	0.654	95.9	335
0.252	3	13.2	0.664	0.561	97.2	293
0.255	4	14.7	0.646	0.475	102	261
0.260	3	17.4	0.617	0.371	114	232
0.265	3	19.9	0.596	0.299	127	219
0.271	3	24.2	0.566	0.658	47.1	342
0.274	2	26.2	0.555	0.572	47.6	311
0.279	3	29.9	0.536	0.534	48.5	301
0.283	2	33.2	0.522	0.474	49.2	283
0.286	2	36.4	0.510	0.425	49.6	268
0.291	2	42.0	0.491	0.377	50.3	260

Table B.6: Properties of selected models. See Table B.1 for a description of the parameters.

Z = 0.01, diffusion+rotation

Mass ($M_\odot$)	# flashes	$P_{\rm orb,det}$ (d)	$M_{\rm H,det}$ (10^{-2} $M_\odot$)	$M_{\rm H,T_{eff,max}}$ (10^{-3} $M_\odot$)	$\Delta t_{\rm proto}$ (Myr)	$t_{\rm cool,L_{-2}}$ (Myr)
0.182	7	1.01	1.04	0.873	1390	1740
0.183	6	1.09	1.04	0.898	1270	1620
0.187	7	1.34	1.04	0.946	1070	1460
0.192	7	1.72	1.02	0.957	823	1210
0.195	7	1.92	1.02	0.790	777	1020
0.197	6	2.14	0.983	0.995	615	1020
0.206	5	3.32	0.958	0.689	491	652
0.216	5	4.59	1.09	0.824	339	618
0.226	4	5.79	1.41	0.870	264	596
0.234	4	7.05	0.775	0.543	187	317
0.239	4	8.58	0.740	0.399	199	262
0.244	3	10.2	0.709	0.723	102	378
0.248	3	11.7	0.684	0.660	95.1	342
0.252	4	13.2	0.663	0.565	98.9	293
0.258	3	16.0	0.631	0.401	111	240
0.262	3	18.5	0.608	0.326	121	222
0.265	3	19.9	0.596	0.299	127	219
0.275	2	26.8	0.551	0.579	48.1	314
0.279	2	30.4	0.533	0.501	48.9	289
0.301	2	54.3	0.460	0.290	52.3	251
0.324	1	90.6	0.401	0.556	12.3	368

Table B.7: Properties of selected models. See Table B.1 for a description of the parameters.

Z = 0.001, basic models (no element diffusion nor rotation)

Mass ($M_\odot$)	# flashes	$P_{\rm orb,det}$ (d)	$M_{\rm H,det}$ (10^{-2} $M_\odot$)	$M_{\rm H,T_{eff,max}}$ (10^{-3} $M_\odot$)	$\Delta t_{\rm proto}$ (Myr)	$t_{\rm cool,L_{-2}}$ (Myr)
0.182	0	0.471	1.48	3.74	1100	2640
0.190	0	0.674	1.55	3.71	816	2860
0.207	0	1.45	1.58	3.64	387	3550
0.211	0	1.75	1.56	3.62	314	3410
0.228	0	3.49	1.44	3.44	142	2760
0.234	0	4.62	1.37	3.32	102	2610
0.238	0	5.38	1.32	3.25	85.5	2470
0.246	0	7.22	1.23	3.10	60.2	2310
0.252	3	8.90	1.17	1.85	88.9	1760
0.256	4	10.4	1.10	1.87	72.2	1720
0.260	4	11.8	1.05	1.63	73.2	1630
0.263	3	13.0	1.02	1.79	60.6	1690
0.266	3	14.0	0.999	1.97	61.7	1780
0.274	3	17.5	1.01	1.48	61.8	1540
0.282	3	20.0	1.16	1.27	65.5	1430
0.289	2	22.0	1.42	1.55	43.1	1510
0.302	2	26.9	0.861	1.11	45.5	1310
0.309	1	31.9	0.815	1.56	15.6	1450
0.328	1	49.1	0.708	1.16	16.6	1270
0.340	1	63.7	0.648	0.950	18.9	1150
0.350	1	76.9	0.607	0.810	21.4	1090
0.423	0	258	0.385	0.781	0.406	875

Table B.8: Properties of selected models. See Table B.1 for a description of the parameters.

Z = 0.001, diffusion

Mass ($M_\odot$)	# flashes	$P_{\mathrm{orb,det}}$ (d)	$M_{\mathrm{H,det}}$ (10^{-2} $M_\odot$)	$M_{\mathrm{H,T_{eff,max}}}$ (10^{-3} $M_\odot$)	$\Delta t_{\mathrm{proto}}$ (Myr)	$t_{\mathrm{cool,L_{-2}}}$ (Myr)
0.180	0	0.466	1.50	5.00	1280	0.00
0.183	5	0.582	1.58	4.86	1160	0.00
0.190	0	0.800	1.64	4.63	886	5900
0.196	0	1.05	1.67	4.44	692	5830
0.217	1	2.65	1.60	3.87	261	3920
0.230	4	4.59	1.46	1.21	289	805
0.239	6	6.61	1.35	0.840	227	589
0.245	5	8.54	1.27	0.958	155	580
0.250	2	10.3	1.20	0.674	168	451
0.254	2	11.9	1.15	0.651	153	429
0.264	2	16.7	1.01	0.668	122	412
0.268	1	18.5	0.985	0.518	149	360
0.271	1	19.9	0.986	0.462	153	341
0.280	3	23.4	1.11	0.756	77.6	438
0.314	1	41.4	0.785	0.339	76.9	282
0.322	3	49.7	0.734	0.676	28.1	452

Table B.9: Properties of selected models. See Table B.1 for a description of the parameters.

Z = 0.001, diffusion+rotation

Mass ($M_\odot$)	# flashes	$P_{\mathrm{orb,det}}$ (d)	$M_{\mathrm{H,det}}$ (10^{-2} $M_\odot$)	$M_{\mathrm{H,T_{eff,max}}}$ (10^{-3} $M_\odot$)	$\Delta t_{\mathrm{proto}}$ (Myr)	$t_{\mathrm{cool,L_{-2}}}$ (Myr)
0.179	0	0.477	1.54	5.30	1310	0.00
0.183	0	0.572	1.59	5.18	1140	0.00
0.190	0	0.783	1.65	4.86	891	2300
0.196	0	1.03	1.68	4.62	702	2230
0.216	0	2.59	1.59	4.02	270	4180
0.228	0	4.55	1.43	3.74	144	2800
0.237	4	6.58	1.32	1.18	233	0.00
0.244	1	8.49	1.23	0.646	246	496
0.250	5	10.2	1.18	0.986	138	582
0.254	5	11.7	1.16	0.803	132	487
0.260	5	14.4	1.07	0.808	109	479
0.275	1	21.1	1.03	0.443	144	326
0.287	1	25.0	1.35	0.489	102	332
0.296	2	27.3	0.910	0.725	50.4	435
0.303	1	32.3	0.858	0.558	58.0	351
0.314	1	41.5	0.785	0.341	78.9	284
0.322	1	49.7	0.734	0.644	28.3	428

Table B.10: Properties of selected models. See Table B.1 for a description of the parameters.

Z = 0.0002, basic models (no element diffusion nor rotation)

Mass ($M_\odot$)	# flashes	$P_{\rm orb,det}$ (d)	$M_{\rm H,det}$ (10^{-2} $M_\odot$)	$M_{\rm H,T_{eff,max}}$ (10^{-3} $M_\odot$)	$\Delta t_{\rm proto}$ (Myr)	$t_{\rm cool,L_{-2}}$ (Myr)
0.214	0	0.900	2.10	3.78	533	3550
0.227	0	1.61	2.10	3.74	318	2980
0.247	0	3.86	1.90	3.58	131	2350
0.260	0	6.21	1.74	3.42	76.6	2110
0.268	0	8.30	1.63	3.28	54.9	1940
0.274	0	10.1	1.56	3.17	43.9	1870
0.278	0	11.6	1.51	3.10	37.4	1810
0.282	0	12.8	1.47	3.03	33.2	1780
0.284	1	13.9	1.43	2.44	41.0	1750
0.287	3	14.9	1.40	1.98	47.6	1480
0.289	4	15.8	1.38	1.84	47.0	1410
0.290	4	16.6	1.36	1.83	45.6	1410
0.292	4	17.3	1.34	1.73	44.7	1370
0.293	3	18.0	1.32	1.96	36.1	1420
0.295	3	18.7	1.31	1.82	37.0	1370
0.297	3	19.9	1.28	1.60	39.2	1310
0.302	4	23.1	1.20	1.50	36.9	1270
0.305	3	25.0	1.16	1.90	25.6	1380
0.308	4	26.8	1.12	1.61	31.8	1310
0.313	3	30.2	1.07	1.65	27.2	1300
0.317	2	33.4	1.04	1.85	20.0	1340
0.320	2	34.9	1.05	1.74	20.4	1300
0.322	2	36.4	1.06	1.65	21.0	1280
0.327	2	39.1	1.12	1.47	23.2	1210
0.329	2	40.4	1.18	1.38	25.0	1180
0.336	2	43.1	1.39	1.13	33.4	1100
0.340	1	44.6	1.55	1.68	16.0	1250
0.342	1	45.5	1.06	1.62	11.6	1220
0.356	1	57.5	0.901	1.32	10.7	1110
0.441	0	232	0.514	0.940	0.552	829

Table B.11: Properties of selected models. See Table B.1 for a description of the parameters.

Z = 0.0002, diffusion

Mass ($M_\odot$)	# flashes	$P_{\rm orb,det}$ (d)	$M_{\rm H,det}$ (10^{-2} $M_\odot$)	$M_{\rm H,T_{eff,max}}$ (10^{-3} $M_\odot$)	$\Delta t_{\rm proto}$ (Myr)	$t_{\rm cool,L_{-2}}$ (Myr)
0.226	0	1.78	2.23	4.18	374	4060
0.234	0	2.54	2.17	4.01	265	3670
0.244	0	4.00	2.03	3.81	166	3240
0.246	0	4.40	2.00	3.77	149	3130
0.255	0	6.38	1.86	3.60	98.3	2830
0.263	0	8.56	1.74	3.43	69.8	2640
0.269	5	10.5	1.66	1.19	122	735
0.273	0	12.1	1.60	3.22	46.4	2420
0.277	4	13.5	1.55	0.919	110	569
0.282	4	15.9	1.48	0.944	89.1	573
0.286	5	17.8	1.43	0.952	76.1	574
0.289	5	19.4	1.39	0.678	100	441
0.290	5	20.1	1.38	0.644	103	420
0.291	4	20.8	1.36	1.03	59.3	639
0.297	4	24.3	1.28	1.04	48.8	664
0.300	4	26.3	1.24	0.899	53.4	570
0.311	5	34.8	1.08	0.657	66.5	412

Table B.12: Properties of selected models. See Table B.1 for a description of the parameters.

Z = 0.0002, diffusion+rotation

Mass ($M_\odot$)	# flashes	$P_{\rm orb,det}$ (d)	$M_{\rm H,det}$ (10^{-2} $M_\odot$)	$M_{\rm H,T_{eff,max}}$ (10^{-3} $M_\odot$)	$\Delta t_{\rm proto}$ (Myr)	$t_{\rm cool,L_{-2}}$ (Myr)
0.212	0	0.902	2.17	4.79	621	0.00
0.236	0	2.90	2.13	4.11	229	3290
0.250	0	5.32	1.92	3.77	121	3100
0.259	0	7.67	1.76	3.61	80.9	2830
0.266	0	9.76	1.65	3.51	61.8	0.00
0.270	0	11.5	1.57	3.46	51.0	2590
0.274	0	13.1	1.52	3.40	44.5	2560
0.277	3	14.4	1.47	1.08	115	688
0.280	5	15.6	1.43	1.19	89.2	779
0.282	5	16.6	1.40	1.10	89.1	692
0.284	4	17.5	1.38	0.875	103	542
0.286	5	18.4	1.36	0.892	95.9	556
0.287	5	19.1	1.34	0.836	94.3	519
0.288	5	19.9	1.32	0.893	84.0	558
0.290	5	20.6	1.32	0.872	82.0	538
0.291	5	21.2	1.31	0.897	75.2	552
0.293	5	21.8	1.30	0.868	74.9	541

Curriculum Vitae

Personal Details

Name	Alina Georgiana Istrate
Date of Birth	6 January 1986
Email	istrate@uwm.edu

Education

2012–2016	PhD in Astrophysics, Rheinische Friedrich-Wilhelms-Universität, Bonn, Germany.
2009–2012	Master of Science in Computer Simulation in Science, Bergische Universität Wuppertal, Germany
2004–2009	Bachelor of Science in Physics, University of Bucharest, Romania

Professional Experience

2016–	Postdoc position at Center for Gravitation, Cosmology and Astrophysics, Department of Physics, University of Wisconsin-Milwaukee, US
2012–2016	Doctoral work at the University of Bonn, Germany.
2010	Guest student Programme at Jülich Supercomputing Center, Germany
2009	Summer Research Program at Nano Initiative Munich, Germany
2008	International Summer Program at Helmoltz Centrum Berlin, Germany
2007	Internship at Max Planck Institute for Radioastronomy, Bonn, Germany

Scholarships

2004–2005	Study Scholarship at University of Bucharest, Romania
2005–2006	Praiseworthy Scholarship at University of Bucharest, Romania
2006–2007	Erasmus Scholarship at University of Bonn, Germany

Teaching Experience

2012/2013	Teaching assistant, "Stellar structure and evolution", University of Bonn, Germany
2013/2014	Tutor for lab course, "Spectroscopy of stars", University of Bonn, Germany

List of publications

Refereed publications

1. **Istrate, A. G.**, Tauris, T. M., Langer, N., 2014, A&A, Volume 571, id.A45, *The formation of low-mass helium white dwarfs orbiting pulsars: Evolution of low-mass X-ray binaries below the bifurcation period.*
2. **Istrate, A. G.**, Tauris, T. M., Langer, N.; Antoniadis, J., 2014, A&A, Volume 571, id.L3, 6 pp, *The timescale of low-mass proto-helium white dwarf evolution*.
3. **Istrate, A. G.**, Marchant, P., Tauris, T. M., Langer, N., Stancliffe, R. J., Grassitelli, L. 2016, accepted to A&A, *Models of low-mass helium white dwarfs including gravitational settling, thermal and chemical diffusion, and rotational mixing*.
4. Bours, M. C. P., Marsh, T. R., Gänsicke, B. T., Tauris, T. M., **Istrate, A. G.**, Badenes, C., Dhillon, V. S., Gal-Yam, A., Hermes, J. J., Kengkriangkrai, S., Kilic, M., Koester, D., Mullally, F., Prasert, N., Steeghs, D., Thompson, S. E., Thorstensen, J. R., 2015, MNRAS, Volume 450, Issue 4, p.3966-3974, *A double white dwarf with a paradoxical origin?*
5. Grassitelli, L., Fossati, L., Langer, N., Miglio, A., **Istrate, A. G.**, Sanyal, D., 2015, A&A, Volume 584, id.L2, 5 pp, *Relating turbulent pressure and macroturbulence across the HR diagram with a possible link to γ Doradus stars*

Non-refereed publication

1. **Istrate, Alina G.**, 2015, Conference Series, Vol. 493. San Francisco: Astronomical Society of the Pacific, 2015, p.487 , *The Formation of Low-mass Helium White Dwarfs in Close Binaries.*

Acknowledgements

Nothing happens unless first a dream.

Carl Sandburg

It’s been a long road and not an easy journey. First of all, this thesis would not have been possible without Norbert. He gave me the chance to do research in Astrophysics, even if at that point, my background in this field was non-existent. The interview for the PhD position was the best interview I experienced! So thank you Norbert for giving me this chance and for believing in me! Moreover, thank you for all the time you took whenever I had questions and for basically teaching me how to have a critical mind.

I want to thank Thomas for guiding me all these years. His passion for science was always inspiring and his every day optimism uplifting. One thing that I know for sure I inherited from him is being detailed oriented! He took his Doktorvater role extremely serious and sometimes it almost felt like I was a teenager all over again. But, when the time was right, he gave me complete scientific freedom and for that I am sincerely grateful. Like a teenager, I complained a lot on the way but now, looking back, I am very happy and proud to have Thomas as my Doktorvater.

There were a lot of people that helped me get where I am now, during the various stages of this trip. Thank you to all of you. Especially thank you to Popi, the engineer of our imaginary spaceship, to Cristian Roman for all the books and science letters, to Sonka for all the observing nights, to Traian for teaching me how to fight my own demons.

The PhD journey coincided with the most tumultuous period in my personal life. I am forever in debt to all the people who helped during that time, and gave me the positive energy I needed so much.

I want to thank Luca for always being there, for his sugar-free way of talking, for all the long scientific and philosophical talks late in the evenings and for teaching me that cooking is an art itself. Thank you to JC for being one of the most positive people around and for all the time he took to listen to my complains. And for all the coffees, the nutella and all the tequila. Thank you to my office mates, Pablo and Fabian for making the office a happy place! Thank you to Richard for the long scientific and non-scientific discussions! Thank you to Hananeh for all the support during the writing of this thesis, and for all the coffees! Thank you to Toma, Norberto, Ana, Debi, Reiko, Benjamin for making AIfA a much more enjoyable place. Thank you to the kickers group in the institute, especially to Alex, for all the training sessions, literally with sweat and blood. Thank you to all the members of the stellar group as well as the cosmology group. Thank you to the Italian lady from the coffee shop for all the great coffee used to finish this work! Thank you to the dungeon master and my party for the great adventures together! There were a lot of times when I said that I couldn’t wait to leave AIfA, but now, several months after I left, I actually really miss it. I guess AIfA will always have a special place in my life, the second home.

Thank you to my parents for making me fight for my dreams! Thank you to my parents-in-law for

showing me what a real family is.
Thank you to my husband for all the love, support, understanding and patience during all this time. And for teaching me stuff about the real life here on Earth, things that I should know but I don't!
And, in the end, thank you to my brother for not giving up! One step at a time!

Bibliography

Alberts, F., Savonije, G. J., van den Heuvel, E. P. J., & Pols, O. R. 1996, Nature, 380, 676 46

Alpar, M. A., Cheng, A. F., Ruderman, M. A., & Shaham, J. 1982, Nature, 300, 728 15, 22

Althaus, L. G. & Benvenuto, O. G. 2000, MNRAS, 317, 952 60

Althaus, L. G., Córsico, A. H., Isern, J., & García-Berro, E. 2010, A&A Rev., 18, 471 10, 11

Althaus, L. G., Miller Bertolami, M. M., & Córsico, A. H. 2013, A&A, 557, A19 37, 46, 51, 55, 57, 60, 67, 77, 79, 83

Althaus, L. G., Panei, J. A., Romero, A. D., et al. 2009, A&A, 502, 207 60

Althaus, L. G., Serenelli, A. M., & Benvenuto, O. G. 2001a, MNRAS, 323, 471 55, 57, 60, 81, 83

Althaus, L. G., Serenelli, A. M., & Benvenuto, O. G. 2001b, ApJ, 554, 1110 60

Althaus, L. G., Serenelli, A. M., & Benvenuto, O. G. 2001c, MNRAS, 324, 617 37, 46, 48, 51, 55, 56, 60

Amaro-Seoane, P., Aoudia, S., Babak, S., et al. 2012, Classical and Quantum Gravity, 29, 124016 54

Andrews, J. J., Price-Whelan, A. M., & Agüeros, M. A. 2014, ApJ, 797, L32 55

Antoniadis, J., Freire, P. C. C., Wex, N., et al. 2013, Science, 340, 448 20, 22, 23, 34, 38, 39, 42, 92

Antoniadis, J., van Kerkwijk, M. H., Koester, D., et al. 2012, MNRAS, 423, 3316 23, 24, 27, 38, 70, 92

Antoniadis, J. I. 2013, PhD thesis, University of Bonn 92

Applegate, J. H. & Shaham, J. 1994, ApJ, 436, 312 43

Archibald, A. M., Stairs, I. H., Ransom, S. M., et al. 2009, Science, 324, 1411 15, 42

Baade, W. & Zwicky, F. 1934a, Proceedings of the National Academy of Science, 20, 259 13

Baade, W. & Zwicky, F. 1934b, Proceedings of the National Academy of Science, 20, 254 13

Backer, D. C., Kulkarni, S. R., Heiles, C., Davis, M. M., & Goss, W. M. 1982, Nature, 300, 615 26

Barnes, S. A. 2003, ApJ, 586, 464 41

Barnes, S. A. & Kim, Y.-C. 2010, ApJ, 721, 675 41

Bassa, C. G., Antoniadis, J., Camilo, F., et al. 2016, MNRAS, 455, 3806 57, 70

Bassa, C. G., Patruno, A., Hessels, J. W. T., et al. 2014, MNRAS, 441, 1825 42

Bassa, C. G., van Kerkwijk, M. H., Koester, D., & Verbunt, F. 2006a, A&A, 456, 295 38, 92

Bassa, C. G., van Kerkwijk, M. H., & Kulkarni, S. R. 2006b, A&A, 450, 295 24, 92

Benvenuto, O. G., De Vito, M. A., & Horvath, J. E. 2012, ApJ, 753, L33 26, 42

Bhattacharya, D. & van den Heuvel, E. P. J. 1991, Physics Reports, 203, 1 15, 21, 25

Bildsten, L., Chakrabarty, D., Chiu, J., et al. 1997, ApJS, 113, 367 15

Bildsten, L., Shen, K. J., Weinberg, N. N., & Nelemans, G. 2007, ApJ, 662, 95 54

Bours, M. C. P., Marsh, T. R., Gänsicke, B. T., et al. 2015, MNRAS, 450, 3966 77, 81

Braun, H. 1997, PhD thesis, , Ludwig-Maximilians-Univ. München, (1997) 25

Breton, R. P., Rappaport, S. A., van Kerkwijk, M. H., & Carter, J. A. 2012, ApJ, 748, 115 39, 50, 92

Breton, R. P., van Kerkwijk, M. H., Roberts, M. S. E., et al. 2013, ApJ, 769, 108 48

Brown, W. R., Geller, M. J., Kenyon, S. J., & Kurtz, M. J. 2005, ApJ, 622, 33 45

Brown, W. R., Gianninas, A., Kilic, M., Kenyon, S. J., & Allende Prieto, C. 2016, ApJ, 818, 155 19, 20, 54

Brown, W. R., Kilic, M., Allende Prieto, C., Gianninas, A., & Kenyon, S. J. 2013, ApJ, 769, 66 19, 45, 49, 54, 91

Brown, W. R., Kilic, M., Allende Prieto, C., & Kenyon, S. J. 2010, ApJ, 723, 1072 19, 45, 54

Brown, W. R., Kilic, M., Allende Prieto, C., & Kenyon, S. J. 2012, ApJ, 744, 142 19, 54

Brown, W. R., Kilic, M., Hermes, J. J., et al. 2011, ApJ, 737, L23 20

Büning, A. & Ritter, H. 2004, A&A, 423, 281 42

Cadelano, M., Pallanca, C., Ferraro, F. R., et al. 2015, ApJ, 812, 63 54

Callanan, P. J., Garnavich, P. M., & Koester, D. 1998, MNRAS, 298, 207 23, 92

Camilo, F., Thorsett, S. E., & Kulkarni, S. R. 1994, ApJ, 421, 15 46, 56

Cantiello, M. & Langer, N. 2010, A&A, 521, A9 25

Canuto, V. 1970, ApJ, 159, 641 25

Carter, J. A., Rappaport, S., & Fabrycky, D. 2011, ApJ, 728, 139 50, 92

Cassisi, S., Potekhin, A. Y., Pietrinferni, A., Catelan, M., & Salaris, M. 2007, ApJ, 661, 1094 58

Chaty, S. 2013, Advances in Space Research, 52, 2132 15

Chen, H.-L., Chen, X., Tauris, T. M., & Han, Z. 2013, ApJ, 775, 27 22, 26, 40, 42, 48

Christensen-Dalsgaard, J. 2015, MNRAS, 453, 666 69

Clayton, G. C. 2013, in Astronomical Society of the Pacific Conference Series, Vol. 469, 18th European White Dwarf Workshop., 133 54

Coriat, M., Fender, R. P., & Dubus, G. 2012, MNRAS, 424, 1991 27, 42

Corongiu, A., Burgay, M., Possenti, A., et al. 2012, ApJ, 760, 100 38

Córsico, A. H. & Althaus, L. G. 2014a, A&A, 569, A106 20, 54, 92

Córsico, A. H. & Althaus, L. G. 2014b, ApJ, 793, L17 54

Córsico, A. H., Althaus, L. G., Serenelli, A. M., et al. 2016, A&A, 588, A74 54, 60

Córsico, A. H., Romero, A. D., Althaus, L. G., & Hermes, J. J. 2012, A&A, 547, A96 20

Corti, M. A., Kanaan, A., Córsico, A. H., et al. 2016, A&A, 587, L5 54

D'Antona, F. & Mazzitelli, I. 1990, ARA&A, 28, 139 11

D'Antona, F., Ventura, P., Burderi, L., et al. 2006, ApJ, 640, 950 29

De Vito, M. A. & Benvenuto, O. G. 2010, MNRAS, 401, 2552 37, 55, 81

Debes, J. H. & Sigurdsson, S. 2002, ApJ, 572, 556 75

Detmers, R. G., Langer, N., Podsiadlowski, P., & Izzard, R. G. 2008, A&A, 484, 831 59

Dorch, S. B. F. & Nordlund, Å. 2001, A&A, 365, 562 41

Driebe, T., Schoenberner, D., Bloecker, T., & Herwig, F. 1998, A&A, 339, 123 37, 46, 48, 51, 55, 56

Dubus, G., Hameury, J.-M., & Lasota, J.-P. 2001, A&A, 373, 251 27, 42

Dubus, G., Lasota, J.-P., Hameury, J.-M., & Charles, P. 1999, MNRAS, 303, 139 42

Edmonds, P. D., Gilliland, R. L., Heinke, C. O., Grindlay, J. E., & Camilo, F. 2001, ApJ, 557, 57 23, 92

Eggleton, P. P. 1983, ApJ, 268, 368 6, 25

Eggleton, P. P. 2001, in Astronomical Society of the Pacific Conference Series, Vol. 229, Evolution of Binary and Multiple Star Systems, ed. P. Podsiadlowski, S. Rappaport, A. R. King, F. D'Antona, & L. Burderi, 157 41

Ergma, E. & Sarna, M. J. 1996, MNRAS, 280, 1000 30

Farihi, J., Jura, M., & Zuckerman, B. 2009, ApJ, 694, 805 75

Faulkner, J. 1971, ApJ, 170, L99 26

Fedorova, A. V. & Ergma, E. V. 1989, Ap&SS, 151, 125 30

Ferguson, J. W., Alexander, D. R., Allard, F., et al. 2005, ApJ, 623, 585 58

Foley, R. J. 2015, MNRAS, 452, 2463 54

Fontaine, G., Brassard, P., & Bergeron, P. 2001, PASP, 113, 409 11

Fontaine, G. & Michaud, G. 1979, ApJ, 231, 826 58

Freire, P. C., Kramer, M., Lyne, A. G., et al. 2001, ApJ, 557, 105 13

Freire, P. C. C., Wex, N., Esposito-Farèse, G., et al. 2012, MNRAS, 423, 3328 24

Fruchter, A. S., Stinebring, D. R., & Taylor, J. H. 1988, Nature, 333, 237 15, 26

Fryer, C. L. & Kalogera, V. 2001, ApJ, 554, 548 12

Gaensicke, B., Tremblay, P.-E., Barstow, M., et al. 2015, ArXiv e-prints 8

García-Berro, E., Torres, S., Althaus, L. G., et al. 2010, Nature, 465, 194 8

Gautschy, A. 2013, ArXiv astro-ph: 1303.6652 46, 60

Giacconi, R., Gursky, H., Kellogg, E., Schreier, E., & Tananbaum, H. 1971, ApJ, 167, L67 15

Gianninas, A., Curd, B., Fontaine, G., Brown, W. R., & Kilic, M. 2016, ArXiv e-prints 20, 54, 60, 83, 88

Gianninas, A., Dufour, P., Kilic, M., et al. 2014a, ApJ, 794, 35 20, 54, 75, 76, 77, 78

Gianninas, A., Hermes, J. J., Brown, W. R., et al. 2014b, ApJ, 781, 104 54

Gianninas, A., Kilic, M., Brown, W. R., Canton, P., & Kenyon, S. J. 2015, ApJ, 812, 167 19, 77, 81

Grevesse, N. & Sauval, A. J. 1998, Space Sci. Rev., 85, 161 58

Hansen, B. M. S. & Liebert, J. 2003, ARA&A, 41, 465 11

Hansen, B. M. S. & Phinney, E. S. 1998, MNRAS, 294, 569 46

Heber, U. 2016, ArXiv e-prints 19, 54

Heger, A., Langer, N., & Woosley, S. E. 2000, ApJ, 528, 368 58

Heger, A., Woosley, S. E., & Spruit, H. C. 2005, ApJ, 626, 350 58

Henyey, L., Vardya, M. S., & Bodenheimer, P. 1965, ApJ, 142, 841 58

Hermes, J. J., Brown, W. R., Kilic, M., et al. 2014a, ApJ, 792, 39 76

Hermes, J. J., Gänsicke, B. T., Koester, D., et al. 2014b, MNRAS, 444, 1674 54, 75

Hermes, J. J., Kilic, M., Brown, W. R., et al. 2012a, ApJ, 757, L21 20

Hermes, J. J., Kilic, M., Brown, W. R., et al. 2012b, ApJ, 757, L21 54

Hermes, J. J., Montgomery, M. H., Gianninas, A., et al. 2013a, MNRAS, 436, 3573 20

Hermes, J. J., Montgomery, M. H., Gianninas, A., et al. 2013b, MNRAS, 436, 3573 45, 54, 91, 92

Hermes, J. J., Montgomery, M. H., Winget, D. E., et al. 2013c, ApJ, 765, 102 20, 54

Hermes, J. J., Montgomery, M. H., Winget, D. E., et al. 2012c, ApJ, 750, L28 20

Hermes, J. J., Montgomery, M. H., Winget, D. E., et al. 2012d, ApJ, 750, L28 54

Hewish, A., Bell, S. J., Pilkington, J. D. H., Scott, P. F., & Collins, R. A. 1968, Nature, 217, 709 13

Hobbs, G., Archibald, A., Arzoumanian, Z., et al. 2010, Classical and Quantum Gravity, 27, 084013 13

Hu, H., Tout, C. A., Glebbeek, E., & Dupret, M.-A. 2011, MNRAS, 418, 195 58

Hubbard, W. B. & Lampe, M. 1969, ApJS, 18, 297 25

Hulse, R. A. & Taylor, J. H. 1975, ApJ, 195, 51 13

Hurley, J. R., Tout, C. A., & Pols, O. R. 2002, MNRAS, 329, 897 59

Hussain, G. A. J. 2011, in Astronomical Society of the Pacific Conference Series, Vol. 447, Evolution of Compact Binaries, ed. L. Schmidtobreick, M. R. Schreiber, & C. Tappert, 143 41

Iben, Jr., I. & MacDonald, J. 1985, ApJ, 296, 540 58

Iben, Jr., I. & Tutukov, A. V. 1984, ApJS, 54, 335 54

Iben, Jr., I. & Tutukov, A. V. 1986, ApJ, 311, 742 46, 47

Iglesias, C. A. & Rogers, F. J. 1993, ApJ, 412, 752 58

Iglesias, C. A. & Rogers, F. J. 1996, ApJ, 464, 943 25, 58

Illarionov, A. F. & Sunyaev, R. A. 1975, A&A, 39, 185 27

Isern, J. & García–Berro, E. 2004, Lecture Notes and Essays in Astrophysics, 1, 23 10

Isern, J., Hernanz, M., Mochkovitch, R., & Garcia-Berro, E. 1991, A&A, 241, L29 11

Istrate, A. G. 2015, in Astronomical Society of the Pacific Conference Series, Vol. 493, 19th European Workshop on White Dwarfs, ed. P. Dufour, P. Bergeron, & G. Fontaine, 487 89

Istrate, A. G., Tauris, T. M., & Langer, N. 2014a, A&A, 571, A45 46, 48, 55, 59, 81, 92

Istrate, A. G., Tauris, T. M., Langer, N., & Antoniadis, J. 2014b, A&A, 571, L3 22, 55, 56, 57, 58, 70, 75, 77, 83

Itoh, N., Kohyama, Y., & Takeuchi, H. 1987, ApJ, 317, 733 58

Ivanova, N., Justham, S., Chen, X., et al. 2013, A&A Rev., 21, 59 8

Jacoby, B. A., Hotan, A., Bailes, M., Ord, S., & Kulkarni, S. R. 2005, ApJ, 629, 113 27

Jeffery, C. S. & Saio, H. 2013, MNRAS, 435, 885 54, 60

Jia, K. & Li, X.-D. 2014, ApJ, 791, 127 39, 41, 81

Johnston, H. M. & Kulkarni, S. R. 1991, ApJ, 368, 504 34

Joss, P. C., Rappaport, S., & Lewis, W. 1987, ApJ, 319, 180 37, 81

Jura, M., Farihi, J., & Zuckerman, B. 2007, ApJ, 663, 1285 75

Kalirai, J. S. 2012, Nature, 486, 90 8

Kaplan, D. L., Bhalerao, V. B., van Kerkwijk, M. H., et al. 2013, ApJ, 765, 158 20, 23, 24, 48, 54, 70, 75, 92

Kaplan, D. L., Marsh, T. R., Walker, A. N., et al. 2014a, ApJ, 780, 167 24, 49, 92

Kaplan, D. L., Stovall, K., Ransom, S. M., et al. 2012, ApJ, 753, 174 24, 48, 70, 92

Kaplan, D. L., van Kerkwijk, M. H., Koester, D., et al. 2014b, ApJ, 783, L23 49, 92

Kawaler, S. D., Novikov, I., Srinivasan, G., Meynet, G., & Schaerer, D. 1996, Stellar Remnants 10

Kepler, S. O., Kleinman, S. J., Nitta, A., et al. 2007, MNRAS, 375, 1315 9

Kepler, S. O., Pelisoli, I., Koester, D., et al. 2015, MNRAS, 446, 4078 9, 54

Kepler, S. O., Pelisoli, I., Koester, D., et al. 2016, MNRAS, 455, 3413 8

Kilic, M. 2011, Cool White Dwarfs, ed. D. W. Hoard, 25–52 11

Kilic, M., Brown, W. R., Allende Prieto, C., et al. 2011, ApJ, 727, 3 19, 54

Kilic, M., Brown, W. R., Allende Prieto, C., et al. 2012, ApJ, 751, 141 19, 45, 54

Kilic, M., Brown, W. R., & Hermes, J. J. 2013, in Astronomical Society of the Pacific Conference Series, Vol. 467, 9th LISA Symposium, ed. G. Auger, P. Binétruy, & E. Plagnol, 47 54

Kilic, M., Hermes, J. J., Gianninas, A., & Brown, W. R. 2015, MNRAS, 446, 26 54

Kilic, M., Hermes, J. J., Gianninas, A., et al. 2014, MNRAS, 438, 26 54

Kilic, M., Stanek, K. Z., & Pinsonneault, M. H. 2007, ApJ, 671, 761 19, 54

Kilic, M., von Hippel, T., Leggett, S. K., & Winget, D. E. 2006, ApJ, 646, 474 75

Kippenhahn, R. & Weigert, A. 1967, ZAp, 65, 251 46

Kippenhahn, R. & Weigert, A. 1990, Stellar Structure and Evolution, 192 25

Kippenhahn, R., Weigert, A., & Weiss, A. 2012, Stellar Structure and Evolution 3

Kleinman, S. J., Kepler, S. O., Koester, D., et al. 2013, ApJS, 204, 5 9

Knigge, C., Baraffe, I., & Patterson, J. 2011, ApJS, 194, 28 41

Koester, D. 2002, A&A Rev., 11, 33 11

Koester, D., Voss, B., Napiwotzki, R., et al. 2009, A&A, 505, 441 54

Kroupa, P. 2002, Science, 295, 82 2

Landau, L. D. & Lifshitz, E. M. 1971, The classical theory of fields (Pergamon Press, Oxford) 26

Langer, N. 1998, A&A, 329, 551 25

Lanza, A. F. & Rodonò, M. 1999, A&A, 349, 887 43

Lasota, J.-P. 2001, New Astron. Rev., 45, 449 42

Latour, M., Heber, U., Irrgang, A., et al. 2016, A&A, 585, A115 54

Lattimer, J. M. & Prakash, M. 2007, Phys. Rep., 442, 109 27

Lazaridis, K., Verbiest, J. P. W., Tauris, T. M., et al. 2011, MNRAS, 414, 3134 43

Lazaridis, K., Wex, N., Jessner, A., et al. 2009, MNRAS, 400, 805 38

Lazarus, P., Tauris, T. M., Knispel, B., et al. 2014, MNRAS, 437, 1485 25, 46

Lin, D. N. C. & Papaloizou, J. 1979, MNRAS, 186, 799 42

Lin, J., Rappaport, S., Podsiadlowski, P., et al. 2011, ApJ, 732, 70 26, 41, 81, 82

Liu, Q. Z., van Paradijs, J., & van den Heuvel, E. P. J. 2007, A&A, 469, 807 15

Lorimer, D. R. 2008, Living Reviews in Relativity, 11, 8

Lorimer, D. R., Lyne, A. G., Festin, L., & Nicastro, L. 1995, Nature, 376, 393 46, 56

Lundgren, S. C., Zepka, A. F., & Cordes, J. M. 1995, ApJ, 453, 419 23

Lyne, A. G., Burgay, M., Kramer, M., et al. 2004, Science, 303, 1153 85

Ma, B. & Li, X.-D. 2009, ApJ, 691, 1611 19, 22, 30

Manchester, R. N., Hobbs, G. B., Teoh, A., & Hobbs, M. 2005, AJ, 129, 1993 16, 17, 22, 34

Marsh, T. R., Dhillon, V. S., & Duck, S. R. 1995a, MNRAS, 275, 828 19

Marsh, T. R., Dhillon, V. S., & Duck, S. R. 1995b, MNRAS, 275, 828 54

Matt, S. P., MacGregor, K. B., Pinsonneault, M. H., & Greene, T. P. 2012, ApJ, 754, L26 86

Maxted, P. F. L., Anderson, D. R., Burleigh, M. R., et al. 2011, MNRAS, 418, 1156 54

Maxted, P. F. L., Bloemen, S., Heber, U., et al. 2014a, MNRAS, 437, 1681 39, 45, 54

Maxted, P. F. L., Serenelli, A. M., Marsh, T. R., et al. 2014b, MNRAS, 444, 208 20, 54

Maxted, P. F. L., Serenelli, A. M., Miglio, A., et al. 2013, Nature, 498, 463 54

Mestel, L. 1952, MNRAS, 112, 583 9

Mestel, L. 1968, MNRAS, 138, 359 26

Nagase, F. 1989, PASJ, 41, 1 15

Nandez, J. L. A., Ivanova, N., & Lombardi, J. C. 2015, MNRAS, 450, 39 55

Nelemans, G. 2009, Classical and Quantum Gravity, 26, 094030 22

Nelemans, G. & Tauris, T. M. 1998, A&A, 335, 85 54

Nelson, L. A., Dubeau, E., & MacCannell, K. A. 2004, ApJ, 616, 1124 37, 46, 47, 51, 55, 67, 81, 87

Nelson, L. A. & Rappaport, S. 2003, ApJ, 598, 431 43

Nelson, L. A., Rappaport, S. A., & Joss, P. C. 1986, ApJ, 304, 231 26

Nicastro, L., Lyne, A. G., Lorimer, D. R., et al. 1995, MNRAS, 273, L68 46

Nice, D. J., Stairs, I. H., & Kasian, L. E. 2008, in American Institute of Physics Conference Series, Vol. 983, 40 Years of Pulsars: Millisecond Pulsars, Magnetars and More, ed. C. Bassa, Z. Wang, A. Cumming, & V. M. Kaspi, 453–458 24, 38

Oswalt, T. D., Smith, J. A., Wood, M. A., & Hintzen, P. 1996, Nature, 382, 692 8

Paczynski, B. 1976, in IAU Symposium, Vol. 73, Structure and Evolution of Close Binary Systems, ed. P. Eggleton, S. Mitton, & J. Whelan, 75 8

Paczynski, B. & Sienkiewicz, R. 1981, ApJ, 248, 27 26, 30

Panei, J. A., Althaus, L. G., Chen, X., & Han, Z. 2007, MNRAS, 382, 779 37, 46, 55, 60

Papitto, A., Ferrigno, C., Bozzo, E., et al. 2013, Nature, 501, 517 16, 42

Paquette, C., Pelletier, C., Fontaine, G., & Michaud, G. 1986, ApJS, 61, 197 54

Parker, E. N. 1955, ApJ, 121, 491 41

Paxton, B., Bildsten, L., Dotter, A., et al. 2011, ApJS, 192, 3 58

Paxton, B., Cantiello, M., Arras, P., et al. 2013, ApJS, 208, 4 58

Paxton, B., Marchant, P., Schwab, J., et al. 2015, ApJS, 220, 15 58, 59

Perets, H. B., Gal-Yam, A., Mazzali, P. A., et al. 2010, Nature, 465, 322 54

Phinney, E. S. 1992, Royal Society of London Philosophical Transactions Series A, 341, 39 16

Podsiadlowski, P. 1991, Nature, 350, 136 43

Podsiadlowski, P., Rappaport, S., & Pfahl, E. D. 2002, ApJ, 565, 1107 22, 26, 30, 35, 41, 47

Pollacco, D. L., Skillen, I., Collier Cameron, A., et al. 2006, PASP, 118, 1407 45

Postnov, K. A. & Yungelson, L. R. 2014, Living Reviews in Relativity, 17, 3 8

Pringle, J. E. 1981, ARA&A, 19, 137 42

Pylyser, E. & Savonije, G. J. 1988, A&A, 191, 57 19, 22, 29, 30

Pylyser, E. H. P. & Savonije, G. J. 1989, A&A, 208, 52 22, 30, 35

Radhakrishnan, V. & Srinivasan, G. 1982, Current Science, 51, 1096 15

Ransom, S. M., Hessels, J. W. T., Stairs, I. H., et al. 2005, Science, 307, 892 16

Ransom, S. M., Stairs, I. H., Archibald, A. M., et al. 2014a, Nature, 505, 520 49

Ransom, S. M., Stairs, I. H., Archibald, A. M., et al. 2014b, Nature, 505, 520 85

Rappaport, S., Joss, P. C., & Webbink, R. F. 1982, ApJ, 254, 616 26, 30

Rappaport, S., Podsiadlowski, P., Joss, P. C., Di Stefano, R., & Han, Z. 1995, MNRAS, 273, 731 22, 37, 81

Rappaport, S., Verbunt, F., & Joss, P. C. 1983, ApJ, 275, 713 27

Refsdal, S. & Weigert, A. 1971, A&A, 13, 367 37, 48, 56, 81

Rhoades, C. E. & Ruffini, R. 1974, Physical Review Letters, 32, 324 12

Ritter, H. 1988, A&A, 202, 93 25

Ritter, H. 2008, New Astronomy Reviews, 51, 869 42

Rivera-Sandoval, L. E., van den Berg, M., Heinke, C. O., et al. 2015, MNRAS, 453, 2707 54

Roberts, M. S. E. 2013, in IAU Symposium, Vol. 291, IAU Symposium, ed. J. van Leeuwen, 127–132 22, 26, 40, 42

Rohrmann, R. D., Althaus, L. G., García-Berro, E., Córsico, A. H., & Miller Bertolami, M. M. 2012, A&A, 546, A119 59

Rowe, J. F., Borucki, W. J., Koch, D., et al. 2010, ApJ, 713, 150 45

Rucinski, S. M. 1983, The Observatory, 103, 280 41

Salpeter, E. E. 1955, ApJ, 121, 161 2

Sarna, M. J., Ergma, E., & Gerškevitš-Antipova, J. 2000, MNRAS, 316, 84 37, 47, 48, 51, 55

Savonije, G. J. 1987, Nature, 325, 416 37, 81

Schönberg, M. & Chandrasekhar, S. 1942, ApJ, 96, 161 40

Segretain, L., Chabrier, G., Hernanz, M., et al. 1994, ApJ, 434, 641 10

Serenelli, A. M., Althaus, L. G., Rohrmann, R. D., & Benvenuto, O. G. 2001, MNRAS, 325, 607 60, 67

Serenelli, A. M., Althaus, L. G., Rohrmann, R. D., & Benvenuto, O. G. 2002a, MNRAS, 337, 1091 37

Serenelli, A. M., Althaus, L. G., Rohrmann, R. D., & Benvenuto, O. G. 2002b, MNRAS, 337, 1091 67

Shannon, R. M., Cordes, J. M., Metcalfe, T. S., et al. 2013, ArXiv e-prints 40

Shao, Y. & Li, X.-D. 2012, ApJ, 756, 85 37, 81

Sills, A., Pinsonneault, M. H., & Terndrup, D. M. 2000, ApJ, 534, 335 41

Silvotti, R., Østensen, R. H., Bloemen, S., et al. 2012, MNRAS, 424, 1752 45, 91

Skumanich, A. 1972, ApJ, 171, 565 19, 41

Soberman, G. E., Phinney, E. S., & van den Heuvel, E. P. J. 1997, A&A, 327, 620 25

Solheim, J.-E. 2010, PASP, 122, 1133 54

Spruit, H. C. 2002, A&A, 381, 923 58

Spruit, H. C. & Ritter, H. 1983, A&A, 124, 267 41

Spruit, H. C. & Taam, R. E. 2001, ApJ, 548, 900 42

Stappers, B. W., Bailes, M., Lyne, A. G., et al. 1996, ApJ, 465, L119 26

Steinfadt, J. D. R., Bildsten, L., & Arras, P. 2010a, ApJ, 718, 441 20

Steinfadt, J. D. R., Kaplan, D. L., Shporer, A., Bildsten, L., & Howell, S. B. 2010b, ApJ, 716, 146 49

Stepien, K. 1995, MNRAS, 274, 1019 41

Stovall, K., Lynch, R. S., Ransom, S. M., et al. 2014, arXiv astro-ph: 1406.5214 23, 24

Tauris, T. M. 1996, A&A, 315, 453 25

Tauris, T. M. 2001, in Astronomical Society of the Pacific Conference Series, Vol. 229, Evolution of Binary and Multiple Star Systems, ed. P. Podsiadlowski, S. Rappaport, A. R. King, F. D'Antona, & L. Burderi, 145 41

Tauris, T. M. 2011, in Astronomical Society of the Pacific Conference Series, Vol. 447, Evolution of Compact Binaries, ed. L. Schmidtobreick, M. R. Schreiber, & C. Tappert, 285 15, 16, 17, 22

Tauris, T. M. 2012, Science, 335, 561 46, 56

Tauris, T. M. 2015, ArXiv astro-ph: 1501.03882 13

Tauris, T. M., Kaspi, V. M., Breton, R. P., et al. 2015, Advancing Astrophysics with the Square Kilometre Array (AASKA14), 39 14

Tauris, T. M., Langer, N., & Kramer, M. 2011, MNRAS, 416, 2130 16, 25

Tauris, T. M., Langer, N., & Kramer, M. 2012, MNRAS, 425, 1601 15, 16, 25, 46, 56

Tauris, T. M., Sanyal, D., Yoon, S.-C., & Langer, N. 2013, A&A, 558, A39 25

Tauris, T. M. & Savonije, G. J. 1999, A&A, 350, 928 22, 27, 29, 30, 37, 38, 40, 69, 81, 82, 92

Tauris, T. M. & van den Heuvel, E. P. J. 2006, Formation and evolution of compact stellar X-ray sources (Cambridge University Press), 623–665 6, 8, 15, 18, 21, 25

Tauris, T. M. & van den Heuvel, E. P. J. 2014, ApJ, 781, L13 27, 38, 49

Tavani, M. & Brookshaw, L. 1992, Nature, 356, 320 43

Thomas, H.-C. 1967, ZAp, 67, 420 69

Thompson, C. & Duncan, R. C. 1995, MNRAS, 275, 255 15

Thoul, A. A., Bahcall, J. N., & Loeb, A. 1994, ApJ, 421, 828 58

Timmes, F. X., Woosley, S. E., & Weaver, T. A. 1996, ApJ, 457, 834 12

Tremblay, P.-E., Kalirai, J. S., Soderblom, D. R., Cignoni, M., & Cummings, J. 2014, ApJ, 791, 92 8

Tutukov, A. V., Fedorova, A. V., Ergma, E. V., & Yungelson, L. R. 1987, Soviet Astronomy Letters, 13, 328 30, 40

van den Heuvel, E. P. J. 1994, in Saas-Fee Advanced Course 22: Interacting Binaries, ed. S. N. Shore, M. Livio, E. P. J. van den Heuvel, H. Nussbaumer, & A. Orr, 263–474 25, 42

van der Sluys, M. V., Verbunt, F., & Pols, O. R. 2005a, A&A, 431, 647 19, 22, 30, 35, 41

van der Sluys, M. V., Verbunt, F., & Pols, O. R. 2005b, A&A, 440, 973 41

Van Grootel, V., Fontaine, G., Brassard, P., & Dupret, M.-A. 2013a, ApJ, 762, 57 20

Van Grootel, V., Fontaine, G., Brassard, P., & Dupret, M.-A. 2013b, ApJ, 762, 57 54

van Haaften, L. M., Nelemans, G., Voss, R., Wood, M. A., & Kuijpers, J. 2012, A&A, 537, A104 26

van Kerkwijk, M. H., Bassa, C. G., Jacoby, B. A., & Jonker, P. G. 2005, in Astronomical Society of the Pacific Conference Series, Vol. 328, Binary Radio Pulsars, ed. F. A. Rasio & I. H. Stairs, 357 38, 45, 46, 47, 54, 57, 70

van Kerkwijk, M. H., Bergeron, P., & Kulkarni, S. R. 1996, ApJ, 467, L89 20, 92

van Kerkwijk, M. H., Rappaport, S. A., Breton, R. P., et al. 2010, ApJ, 715, 51 39, 50, 92

van Paradijs, J. 1996, ApJ, 464, L139+ 27, 42

Vauclair, G., Vauclair, S., & Greenstein, J. L. 1979, A&A, 80, 79 54

Verbunt, F. & Zwaan, C. 1981, A&A, 100, 7 26, 41

Vilhu, O. & Walter, F. M. 1987, ApJ, 321, 958 41

Webbink, R. F. 1975, MNRAS, 171, 555 46

Webbink, R. F., Rappaport, S., & Savonije, G. J. 1983, ApJ, 270, 678 37, 81

Weisberg, J. M., Nice, D. J., & Taylor, J. H. 2010, ApJ, 722, 1030 26

Wellstein, S. & Langer, N. 1999, A&A, 350, 148 25

Wijnands, R. & van der Klis, M. 1998, Nature, 394, 344 15

Wolszczan, A. & Frail, D. A. 1992, Nature, 355, 145 13, 26